INAUGURAL - DISSERTATION

ZUR

ERLANGUNG DER DOKTORWÜRDE

DER

NATURWISSENSCHAFTLICH - MATHEMATISCHEN

GESAMTFAKULTÄT

DER

RUPRECHT-KARLS-UNIVERSITÄT

HEIDELBERG

vorgelegt von

Jie Li (M.Sc.)

aus Hubei, China

Tag der mündlichen Prüfung: 7. Dezember 2018

Cell-ligand interaction study by immobilizing ligand on surface

Gutacher:

Prof. Dr. Joachim P. Spatz
Physikalish-Chemisches Institut
Ruprecht-Karls-Universität Heidelberg
Max-Planck-Institut für Medical Research

Prof. (apl.) Dr. Reiner Dahint
Physikalish-Chemisches Institut
Ruprecht-Karls-Universität Heidelberg

Table of Contents

Note: Section 6.2 is going to be published as an article in a scientific journal.

1 Summary

Integrin-mediated cell-extracellular matrix (ECM) adhesion and cadherin-mediated cell-cell adhesion are two main interactions that exist in organism. In order to exclude complex interference in living organism to study how these specific interactions affect cell behaviors, integrin ligands or cadherin ligands can be isolated and immobilized on/in biomaterials. In this thesis, integrin ligand RGD peptide and/or E-cadherin ligand HAV peptide were immobilized on 2D surfaces to study the cell adhesion force and the adhesion mechanisms.

In part I, cell adhesion force induced by integrin-RGD interaction was studied based on the technology of nitrogen-vacancy (NV) diamond. RGD peptide, which was connected to paramagnetic ion Gd^{3+}, was immobilized onto the NV diamond through PEG chain, generating an NV diamond based force sensor. Spin-spin coupling between Gd^{3+} and NVs dependent photoluminescence was recorded as a signal when cell traction force exerted. Different immobilization methods were developed, in order to obtain an optimized chemical structure for the force sensor. Cell traction force generated by integrin-induced adhesion was presented as relaxation time T1 map within a cell region.

In part II, E-cadherin mimetic HAV peptide was immobilized on continual gold surface or nanopatterned gold surfaces in order to precisely control the immobilized amount. HAV-E-cadherin interaction induced cell adhesion was then studied. The results revealed that the surface immobilized HAV peptide specifically interacted with E-cadherin from cells, inducing the translocation of E-cadherin based adhesion from adherens junction at cell-cell interface to HAV-E-cadherin binding at cell-material interface. This leads to enhanced cell adhesion on the material surfaces and

weakened cell-cell contact, which could play important role in wound healing. The HAV-E-cadherin interaction was proved to activate β-catenin signaling pathway, which was the same as E-cadherin based adherens junction at cell-cell interface.

These studies according to cell-ligand interactions on specific ligands are helpful to understand the mechanisms of cell adhesion and cell-materials interactions, which also provide new information about cell behavior on biomaterials. These results can be important in the design of new biomaterials. NV diamond based force sensor with respective ligand can be considered as a prospective toolbox to investigate different types of cell adhesions. For example, the HAV peptide in the second section can be included to detect the force of E-cadherin-induced cell-cell adhesion.

2 Zusammenfassung

In lebenden Organismen sind für die Zelladhäsion die Integrin-vermittelte Zell-Matrix Adhäsion und die Cadherin-vermittelte Zell-Zell Adhäsion am wichtigsten. Die an diesen Interaktionen beteiligen Integrin-Liganden und Cadherin-Liganden können isoliert und sowohl auf als auch in Biomaterialien immobilisiert werden. Hiermit wird eine Untersuchung des Einflusses der Liganden vermittelten Interaktionen auf das Verhalten der Zellen mit einer geringeren Komplexität als im lebenden Organismus möglich. In dieser Arbeit wurden das RGD Peptid als Integrin-Ligand und/oder das HAV Peptid als E-cadherin Ligand auf 2D Oberflächen immobilisiert und damit die Adhäsionskraft und der Adhäsionsmechanismus der Zellen untersucht.

Im ersten Teil wurde die Adhäsionskraft der Zelle, die durch die Intergin-RGD Interaktion entsteht mit Hilfe der Stickstofffehlstellen (NV) Diamanten Technologie untersucht. Um einen NV Diamanten basierten Kraftsensor zu erhalten, wurden RGD-Peptide, die mit einem paramagnetischen Gd^{3+}-Ion verbunden waren, mittels eines PEG Linkers an einen NV Diamanten gekoppelt. Die Photolumineszens der Spin-Spin Kopplung des Gd^{3+} und der NVs wurde als Signal aufgezeichnet, wenn Zellen Zugkraft ausübten. Es wurden verschiedene Immobilisierungsstrategien entwickelt, um die optimale chemische Struktur für den Kraftsensor zu finden. Die Zugkraft der Zelle, die aus der Integrin vermittelten Adhäsion resultiert, wurde als Relaxationszeit T1 Karte innerhalb einer Zellregion dargestellt.

Im zweiten Teil der Arbeit wurde mimetisches HAV Peptid auf homogenen Goldoberflächen oder um die Konzentration zu kontrollieren auf nanostrukturierten Goldoberflächen immobilisiert. Hiermit wurde die HAV-E-cadherin induzierte Zelladhäsion untersucht. Die Ergebnisse zeigten, dass das an Oberflächen

immobilisierte HAV Peptid spezifisch mit zellulärem E-cadherin interagiert. Diese Wechselwirkung induziert eine Verschiebung von E-cadherin basierter Zell-Zell-Adhäsion an Zell-Zell Grenzflächen hin zu HAV-E-cadherin basierten Bindungen an der Zell-Material Grenzfläche. Dies führt zu einer verstärkten Bindung der Zellen an die Oberfläche, schwächt den Zell-Zell-Kontakt und könnte damit eine wichtige Rolle in der Wundheilung spielen. Es wurde gezeigt, dass die HAV-E-cadherin Interaktion den ß-catenin Signalweg aktiviert, so wie es für die E-cadherin basierten Adhäsionsverbindungen an Zell-Zell Grenzflächen bekannt ist.

Diese Studien zu Zell-Liganden Interaktionen mit Hilfe spezifischer Liganden sind hilfreich um die Mechanismen von Zelladhäsion und Zell-Material Interaktionen zu verstehen. Somit liefern diese Untersuchungen zusätzlich neue Informationen über das Verhalten von Zellen auf Biomaterialien und sind wichtig für die Entwicklung neuer Biomaterialien. Die NV Diamanten basierten Sensoren können mit den entsprechenden Liganden ausgerüstet als zukünftige Werkzeugkiste zur Untersuchung verschiedener Zelladhäsionsarten dienen. So könnte zum Beispiel das HAV Peptid, das im zweiten Teil der Arbeit eingesetzt wurde, in Zukunft in einem solchen Sensor genutzt werden, um die Kraft der E-cadherin induzierten Zell-Zell-Adhäsion zu messen.

3 Introduction

3.1 Cell adhesion

Cell adhesion falls roughly into two catalogs, which are the direct and indirect interactions between neighboring cells. Cells may directly attach to one another through specific molecules on cell membrane, known as direct cell-cell contact.[1] Cells may also secrete extracellular matrix (ECM) to indirectly "glue" all together, known as cell-ECM adhesion.[2] One way or another, the formation of an organized multicellular structure requires the cohesion of cells. Cell adhesion to other cells and to ECM leads to cell communications and environment-sensing, which further affect cell internal structure and determine cell fates.[3] Since three-dimensional tissues are assembled by individual cells, cell adhesion is the molecular basis of tissue architecture and morphogenesis.[4] The establishment and dissolution of cellular attachments as well as the modeling of ECM regulate cell growth and migration within the organism, and thus guide the organogenesis and repair as well as the body growth. Although the cell adhesions are generally stable, these adhesive contacts are regarded to be dynamic rather than static. The maintenance of such stable adhesions often needs active cellular processes.[3-4]

Cell-ECM adhesion and cell-cell adhesion mainly locate in different types of tissues, which are dominated by different cell adhesion molecules (CAM) located on the cell membrane and generating different signaling cascades in cells.

3.1.1 Cell-ECM adhesion

Cell-ECM adhesion plays the main role in connective tissues, in which cells are encapsulated by plenty of ECM. The ECM bears most of the mechanical stress induced by tissue, and allows cells to pull on or to be pulled by ECM via Cell-ECM adhesions. The cell adhesive components in ECM are proteins including collagen, fibrinogen, fibronectin, laminin, and vitronectin.[5-6] The main class of CAMs on the cell membrane to mediate cell-ECM interactions is integrin family. ***Table 3.1*** lists some types of integrins in vertebrates. Integrins are heterodimers of two non-covalently associated α and β subunits. Both subunits are transmembrane glycoproteins. The large N-terminal extracellular domains contribute to the binding of the ECM adhesive proteins.[7-9] Meanwhile, the short intracellular C-terminal tails activate a set of signaling proteins to form a complex and link to the cytoskeleton. ***Figure 3.1*** shows the integrin conformation in inactive and active states. Integrin thus bridges the ECM and cellular cytoskeleton and transmits signals bidirectionally across the plasma membrane. It on the one hand transmits the mechanical and biochemical changes into cells by activating signaling pathways, on the other hand, regulates many biological functions responded by cells.[9-10][16, 17]

Table 3.1 Some types of integrins in vertebrates[11-15]

Integrin	Distribution	Ligands
$\alpha_1\beta_1$	Many	Collagens, laminins
$\alpha_2\beta_1$	Many	Collagens, laminins
$\alpha_3\beta_1$	Many	Laminin-5
$\alpha_4\beta_1$	Hematopoietic cells	Fibronectin, VCAM-1
$\alpha_5\beta_1$	Widespread	Fibronectin, proteinases
$\alpha_6\beta_1$	Widespread	Laminins
$\alpha_7\beta_1$	Muscle, glioma	Laminins
$\alpha_L\beta_2$	T-lymphocytes	ICAM-1, ICAM-2
$\alpha_M\beta_2$	Neutrophils and monocytes	Serum proteins, ICAM-1
$\alpha_{IIb}\beta_3$	Platelets	Fibrinogen, fibronectin
$\alpha_V\beta_1$	Ocular melanoma, neurological tumors	Vitronectin, fibrinogen
$\alpha_V\beta_3$	Activated endothelial cells, melanoma, glioblastoma	Vitronectin, fibronectin, fibrinogen, osteoponin, Cyr61, thyoxine, TETRAC
$\alpha_V\beta_5$	Widespread, esp. fibroblasts, epithelial cells	Vitronectin, adenovirus
$\alpha_V\beta_6$	Proliferating epithelia, esp. lung and mammary gland	Fibronectin, TGFβ1+3
$\alpha_V\beta_8$	Neural tissue, peripheral nerve	Fibronectin, TGFβ1+3
$\alpha_6\beta_4$	Epithelial cells	Laminins

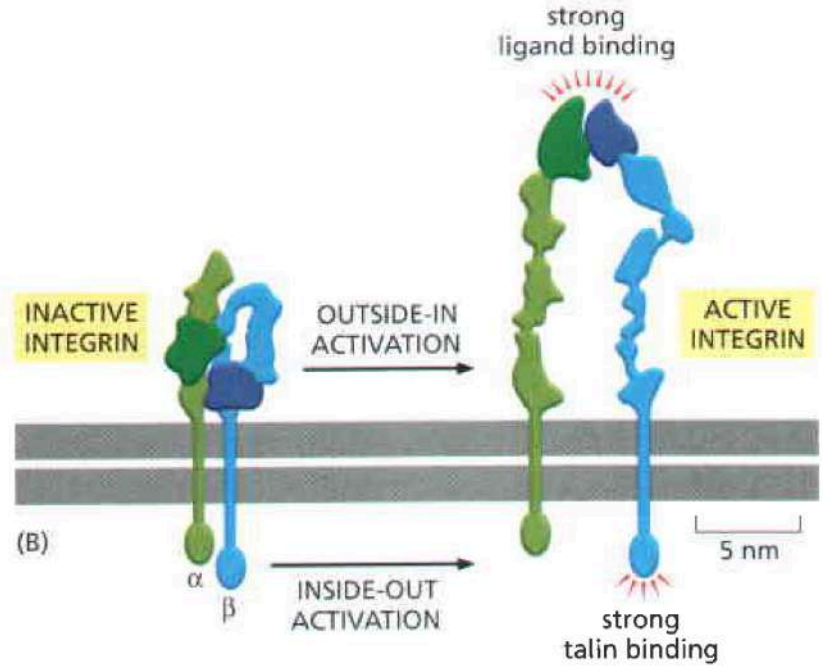

Figure 3.1 Integrin conformation changes when activated. Integrin is folded in inactive state, and the intracellular parts of α and β chains adhere to each other. When integrin is activated by outside ligand binding, or inside talin binding, the structure is extended and the intracellular parts of α and β chains separate apart. Adapted from [1].

Integrin-based cell-ECM adhesion experiences different adhesion stages, as ***figure 3.2*** describes. Activated integrins cluster and recruit integrin-associated signaling proteins at binding points to form specialized adhesion structures at different stages. These structures are different from each other in their morphology, subcellular localization, lifespan, and protein composition.[16] As the early step, actin polymerization and the branched network drive lamellipodial protrusion at the leading edge of cells and lead to the adhesion.[17] The first adhesion structures that become visible by microscopy are nascent adhesions. They are small and highly dynamic, continuously form within the branched actin network.[18] These nascent adhesions only temporally exist. They either disassemble or form the larger focal complexes (FXs) in

the transition zone between the lamellum and the lamellipodium.[19] The subsequent maturation of FXs into focal adhesions (FAs) is force dependent process generated by either cell contractility or external perturbations.[20] Integrin is biochemically and mechanically connected with cytoskeleton at FA points. Cells robustly anchor ECM via this connection to pull the cell body forward but may also restrain the migration process. FAs may finally evolve to fibrillar adhesions (FBs) that are located towards central positions of the cell. FBs are found to bind to fibronectin fibrils[21] to appear as long streaks or dot arrays.[22] FBs are also involved in the remodeling of ECM. Since the adhesion maturation is a dynamic process, all types of adhesion structures can be turned over during cell migration.[16, 23-25]

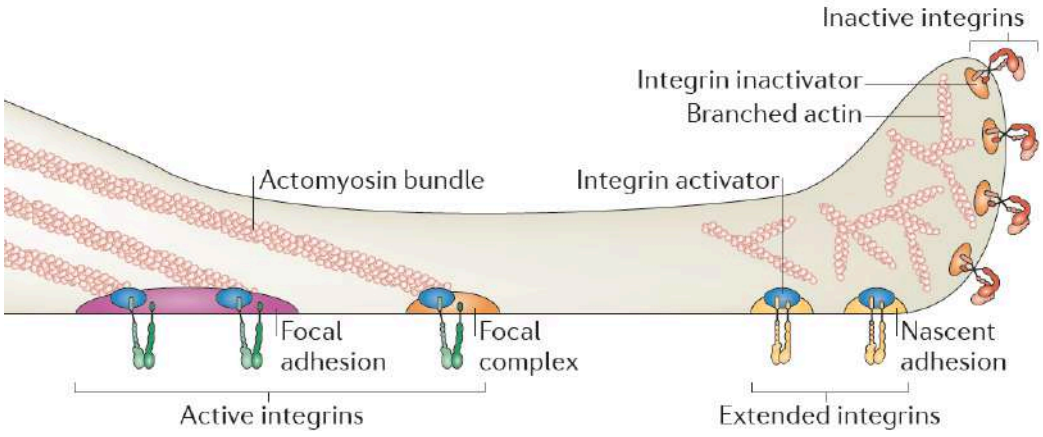

Figure 3.2 Integrin-mediated cell-ECM adhesion.[24] Nascent adhesions firstly appear at lamellipodium protrusion. They are transient and mature into larger focal complexes (FXs). The subsequent maturation of nascent adhesions and FXs into focal adhesions (FAs) is force dependent process, inducing stronger association between integrin and cytoskeleton. Reprinted with kind permission of Springer Nature.

Mechanosensing-based integrin response involves three steps.[26-27] First, integrins are activated by binding to extracellular matrix molecules. Mechanical force can break the contact of α and β integrin subunits and unfold the extracellular domains to expose talin-binding site on the intracellular domain of β chain. Talin, which then binds to integrin, contains actin-binding sites to induce molecular clutch for supporting force transmission, as shown in ***figure 3.3***. In the second step, the applied forces should be transmitted into cells through molecular clutch.[28-29] Therefore the biochemical signals can be activated, known as mechanotransduction. Vinculin also plays a prominent role in molecular clutch besides talin (***figure 3.3***). The tension applied to integrin induces the recruitment of vinculin to focal adhesions.[30] This process is associated with talin and another focal adhesion protein paxillin.[31] Vinculin also directly binds to actin and bear the tension generated by cytoskeleton. It therefore stabilizes and promotes the growth of focal adhesions by regulating the recruitment and the release of other focal adhesion proteins.[32-33] Filamin in focal adhesions also connects integrin and actin for force transduction (***figure 3.3***).[34-36] In a final step, integrin-cytoskeleton linkage transmits force throughout cells. The cell adhesion can be thus reinforced to resist the force sensed by integrin.[37]

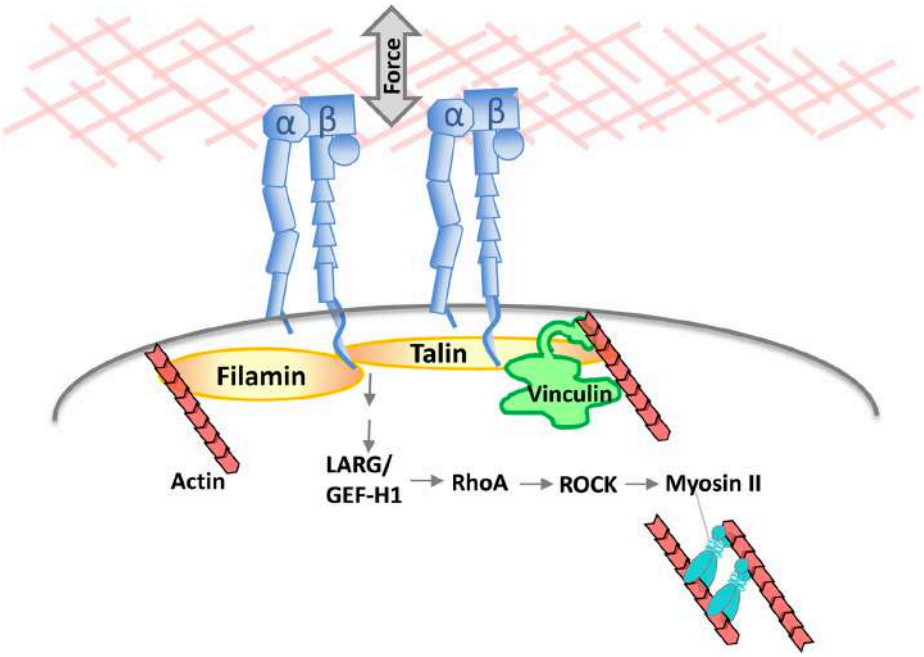

Figure 3.3 Force Transmission at Cell−Matrix Adhesion.[26] Integrin binding to ECM molecules render the expose of talin-binding site. Talin further recruits a molecular clutch for supporting force transmission, including vinculin, paxillin. By a mechanotransduction process, integrin-cytoskeleton linkage transmits force throughout cells finally. Reprinted with kind permission of the American Chemical Society.

Among integrin-induced signaling cascades, the activation of the small GTPase RhoA is one of the keys.[38-39] The activation of RhoA from GDP-bound state to GTP-bound state is regulated by guanine nucleotide exchange factors (GEFs) and GTPase-activating proteins (GAPs). Leukemia-associated Rho GEF (LARG) and guanine nucleotide exchange factor H1 (GEF-H1) directly assist the force-induced RhoA activation (***figure 3.3***).[40] GTP-bound RhoA further activates the Rho kinase (ROCK).[41] ROCK on the one hand can phosphorylate myosin light chain (MLC), on the other hand can inhibit the MLC phosphatase. The phosphorylated MLC promotes the activation of myosin II, which assembles into filaments and interacts with actin

filaments.[42] ATP mediates the conformational changes of assembled myosin II. As a result, force can be generated via the sliding of myosin II and actin filaments against each other to rearrange the actin cytoskeleton.[26] Thereby, cells can rearrange and reinforce the cytoskeleton for the formation of mature adhesions to withstand extracellular mechanical cues (***figure 3.3***).

Integrin-based cell-ECM adhesion transmits the extracellular mechanical cues into cells to regulate the assembly and organization of the cytoskeleton and shape of the cells. This interaction thereby controls the proliferation, apoptosis, and differentiation of the cells, and finally affects their function and commitment.[43]

3.1.2 Cell-cell adhesion

In epithelial tissues, cells are closely bound to each other via cell-cell adhesions.[44] Adherens junctions and desmosome junctions are two types of cell-cell adhesions, which are anchorage sites for actin filaments and intermediate filaments, respectively.[45-46] The key role of the cell adhesion is played by transmembrane adhesion proteins.

Proteins of cadherin superfamily, which are constituted of classical and non-classical cadherins, chiefly mediate cell-cell adherens junction. ***Table 3.2*** lists some members of the cadherin superfamily. They all have an extracellular portion, which contains several copies of cadherin domain. There are five such subdomains, named as EC1-EC5, in the classical cadherins. Cadherins mediate calcium dependent homophilic adhesion through these subdomains. A single subdomain is relatively rigid and connected to each other by a hinge. Each subdomain bind with calcium ions near the hinge to form a rigid but slightly curved rod-like string as the extracellular binding site.[1, 47-49] Meanwhile, the conformation of the N terminus of cadherin

changes slightly to bind oppositely oriented cadherin from neighbor cells. The affinity of the single cadherin-cadherin binding is relatively low, but cadherins on the same cell assemble side-by-side to form clusters. The first extracellular subdomain EC1 interacts with the second extracellular subdomain EC2 of neighboring cadherin via cis interactions.[50] As a result, cadherin-cadherin interaction leads to a zipper-like structure in cadherin clusters to collect all of the weak individual bonds and induce the strong cell-cell adherens junction.[1, 49] On the other hand, the adherens junction can be disassembled by sequentially separating the individual bonds. ***Figure 3.4*** describes this Velcro-like model, just like two pieces of fabric can be joined or peeled apart.

Table 3.2 Some types of cadherins[1]

Cadherin	Main location	Junction association
	Classical cadherins	
E-cadherin	Many epithelia	Adherens junctions
N-cadherin	Neurons, heart, skeletal muscle, lens, and fibroblasts	Adherens junctions and chemical synapses
P-cadherin	Placenta, epidermis, breast epithelium	Adherens junctions
VE-cadherin	Endothelial cells	Adherens junctions
	Nonclassical cadherins	
Desmocollin	Skin	Desmosomes
Desmoglein	Skin	Desmosomes
T-cadherin	Neurons, muscle, heart	None
Cadherin 23	Inner ear, other epithelia	Links between stereocilia in sensory hair cells
Fat (in Drosophila)	Epithelia, central nervous system	Signal-relaying junction (planar cell polarity)
Fat 1 (in mammals)	Various epithelia and central nervous system	Slit diaphragm in kidney glomerulus, other cell junctions

α, β, and γ-Protocadherins	Neurons	Chemical synapses, nonsynaptic membranes
Flamingo	Sensory and some other epithelia	Cell-cell junctions

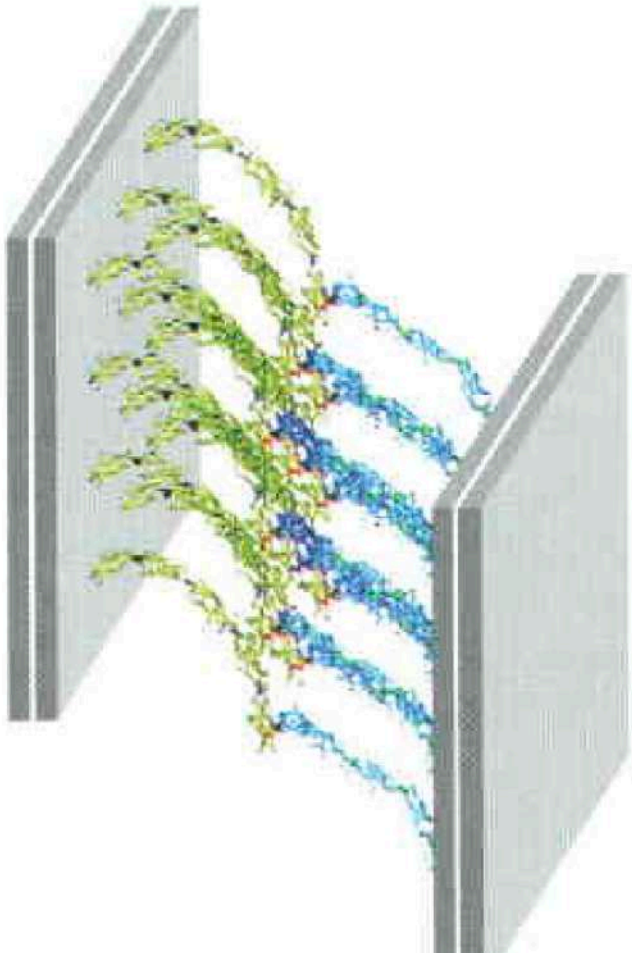

Figure 3.4 Cadherin molecules array at cell-cell contacts.[1] Single cadherin-cadherin interaction is relatively weak. When clustered by side-to-side interaction, many cadherin molecules pack together, forming very strong anchoring junction. Adapted from [1].

While the cadherin extracellular domains mediate such homophilic binding, the intracellular domains provide anchorage for actin cytoskeleton at adherens junctions. The linkage between cadherin and actin is based on a set of accessory intracellular anchor proteins, which can assemble on the cytoplasmic tail of cadherin, as ***figure 3.5*** describes.[26] β-catenin, which is directly assembled on the tail,[51] further recruits and stablizes α-catenin[52] and vinculin[53] at cell-cell junctions. α-catenin, at the same time, interacts with vinculin,[54] while they both connect with actin.[55-56] The force from cell-cell adhesion unfolds α-catenin, which can then bind more vinculin.[57] This process may increase the strength of the cadherin-cytoskeleton connection and thereby induce the force-activated adhesion strengthening. Cadherin interactions initiate RhoA-dependent pathway to activate myosin II.[58-59] Myosin II therefore is involved and affects the cadherin-based mechanotransduction.

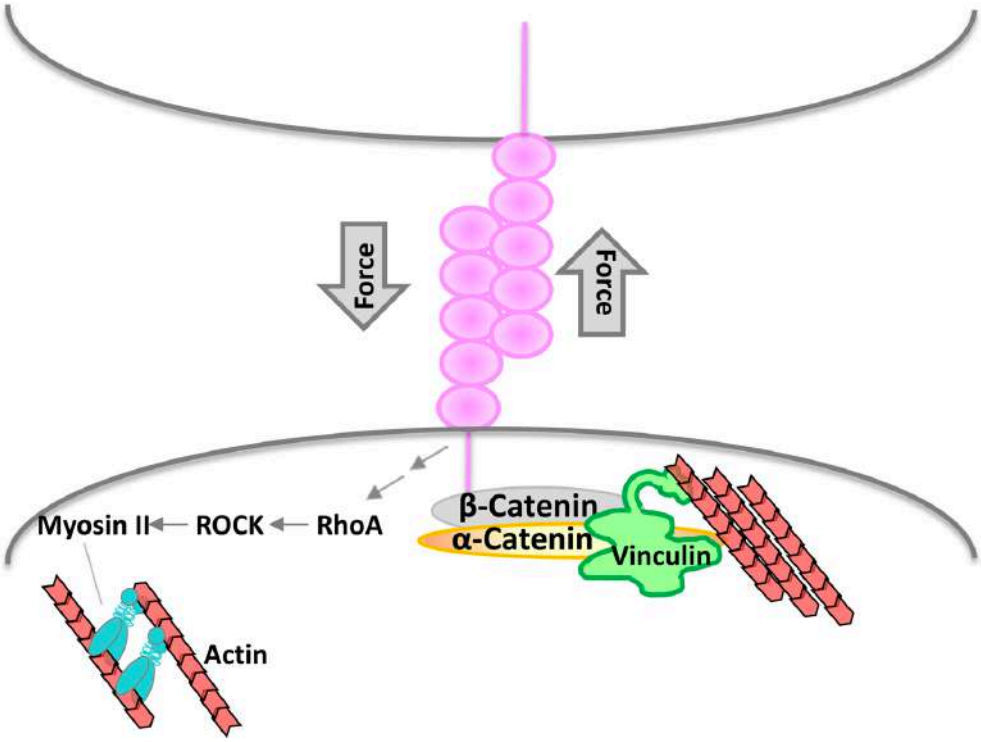

Figure 3.5 Force transmission at cell-cell adhesion.[26] β-catenin is assembled on the cadherin cytoplasmic tail. α-catenin and vinculin are also recruited and stabilized at cell-cell junctions. The force from cell-cell adhesion change the conformation of α-catenin and the connection between α-catenin and vinculin, thereby increasing the strength of the cadherin-cytoskeleton connection. RhoA and Myosin II are also involved in cadherin-based mechanotransduction. Reprinted with kind permission of the American Chemical Society.

Figure 3.6 describes the process of adherens junction formation. When cells get close to each other, the membrane protrusions guided by actin filaments initiate cell-cell contact. The cell-cell contact first causes the formation of small cadherin and catenin clusters, and further activates the intracellular signaling. Thereby, more cadherins and catenins can be recruited to the cell-cell contact region, while actin network expands and the junction expands. In the following step, adherens junction grows in association with actin remodeling and myosin recruitment. Contractile actomyosin network is finally formed and connected to the adherens junction, which allows the stress transmission across the interior of cells.[60] Therefore, cadherin mediated cell-cell adhesion maintains the integrity of the tissue and plays important role in tissue morphogenesis and homeostasis.[47]

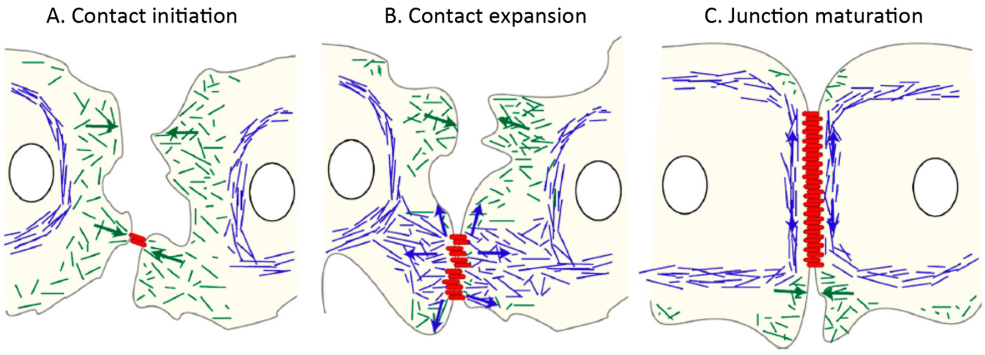

Figure 3.6 Adherens junction formation at cell-cell interface.[61] A: Cell-cell contact is first initiated when cells get close to each other. Small cadherin and catenin clusters are then formed, activating the intracellular signaling. B: More cadherins and catenins are recruited to the cell-cell contact region, while both actin network and junction expand. C: Adherens junction grows in association with actin remodeling and myosin recruitment. Reprinted with kind permission of ROCKEFELLER UNIVERSITY PRESS.

3.1.3 Crosstalk between cell-ECM adhesion and cell-cell adhesion

Cell-ECM adhesion and cell-cell adhesion have similar structure components. They are both linked to cytoskeleton, and share some common adaptor proteins and signaling molecules. Cadherin-mediated adhesion and integrin-mediated adhesion coordinate and are interdependent with each other, which is so called ‘adhesive crosstalk’.[62] In this thesis, 'adhesive crosstalk' generally indicates the functional communication and interaction of cell-ECM adhesion and cell-cell adhesion induced signaling pathways, which is multi-level and varies in time and spatial dimension. ***Figure 3.7*** describes different modes of crosstalk interactions based on short- and long- range of physical associations and cell signaling events.

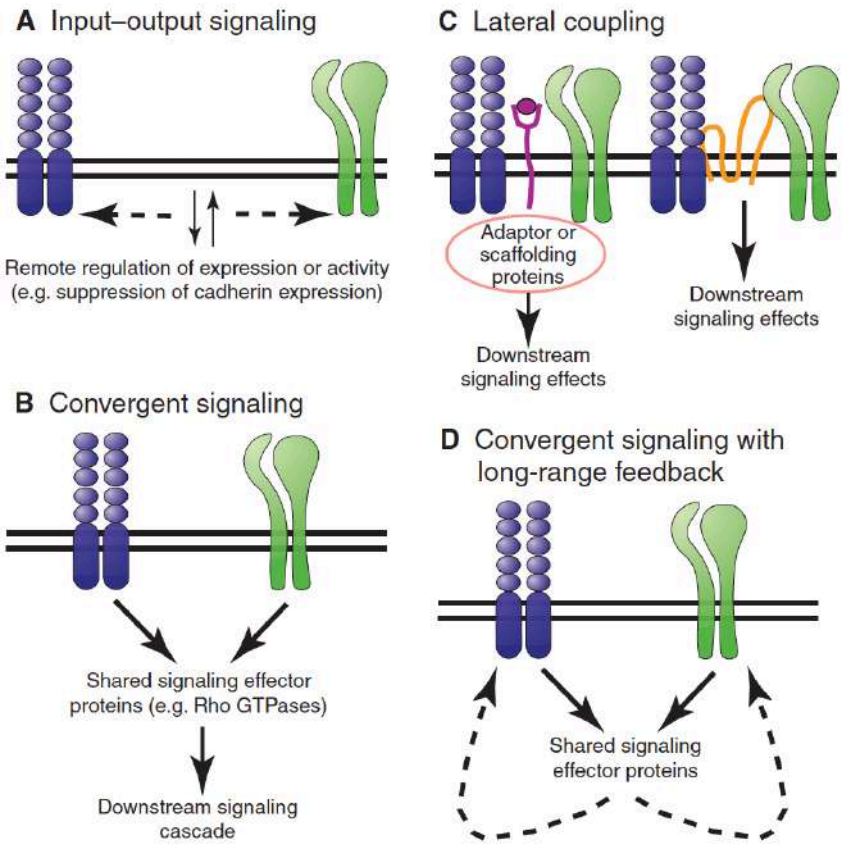

Figure 3.7 Crosstalk interaction modes of cell-ECM adhesion and cell-cell adhesion.[62] A: 'long-range input-output' mode, in which one type of adhesion indirectly affects other adhesions. B: 'convergent signaling' mode. Cell-ECM adhesion and cell-cell adhesion may independently initiate common downstream effectors or signaling pathways. C: 'lateral coupling' mode. Some short-range associations with adaptor proteins or growth factor receptors are involved to laterally couple the adhesion receptors within the plane of the membrane. D: 'convergent signaling with long-range feedback' mode. In this mode, all these three modes may associate with each other and converge into a common pathway. It results in the complex signaling loops, which may give feedbacks to mediate the functions of the initial adhesion elements. Reprinted with kind permission of COMPANY OF BIOLOGISTS LTD..

In the first 'long-range input-output' mode (***figure 3.7 A***), cell ECM adhesion or cell-cell adhesion may induce multiple signaling cascades and finally regulate the gene expression. The changes of the gene expression can alter the levels of adhesion proteins and/or other signaling proteins contributed to adhesions.[63] In other cases, the engagement or disengagement of one type of adhesion may affect membrane trafficking or cytoskeletal association.[64] In this mode, one type of adhesion indirectly affects other adhesions.

In the second 'convergent signaling' mode (***figure 3.7 B***), cell-ECM adhesion and cell-cell adhesion may independently initiate common downstream effectors or signaling pathways. As mentioned above, both adhesions generate force to induce the actin polymerization and the formation of actomyosin network. Other cytoskeletal elements, microtubules and intermediate filaments can be induced by two types of adhesions as well. These cytoskeleton scaffolds connect different types of adhesion complexes. Other shared signaling elements include non-receptor tyrosine kinases, adaptor and scaffolding proteins, and small GTPases.[62]

The third mode is so called 'lateral coupling' (***figure 3.7 C***). Some short-range associations with adaptor proteins or growth factor receptors are involved to laterally couple the adhesion receptors within the plane of the membrane. The coupling does not necessarily require physical connection via cytoskeleton or ligand engagement. For example, the insulin-like growth factor 1 receptor (IGF1R) enables integrin to stabilize cadherin-based cell-cell adhesion.[65-66]

Finally, all these three modes may associate with each other and converge into a common pathway. It results in the complex signaling loops, which may give feedbacks to mediate the functions of the initial adhesion elements (***figure 3.7 D***). For instance, Rho GTPases is the crosstalk point to converge the downstream signaling

from both adhesions, and to induce the upstream signaling to mediate individual adhesion molecules.[65-66]

In epithelia tissues, cell-ECM adhesion and cell-cell adhesion coordinately regulate cell behaviors and also affect each other based on the 'adhesive crosstalk' modes. Cell-ECM adhesion and cell-cell adhesion are spatially segregated in different locations on the cell surface. These two types of adhesions generate mechanical force and regulate actin dynamics in different ways, which contribute to the cell polarity.[67] Two adhesions even exert negative feedback on each other by a variety of ways in different conditions. Cell-ECM adhesion can weaken cell-cell adhesions in some cases, but can be impaired by cell-cell adhesions as well in some other conditions.[68]

The scheme of local negative feedback for the exclusion of two adhesions is shown in ***figure 3.8 A***. When ECM-induced apical membrane protrusions are formed in a monolayer of epithelial cells, the cell-cell adhesion in the same region will be disassembled and reassemble in ECM free region.[69] During cell spreading on ECM, the rigidity of cadherin-mediated adhesion is decreased.[70] The biochemical mechanism is show in ***figure 3.8 B***. Src that is activated by ECM-induced adhesion phosphorylates FAK. Phosphorylated FAK further phosphorylates β-catenin, which causes the disassembly of cadherin complex.[71-72] Meanwhile, the disruption of cadherin complex may result in the release of zyxin, vinculin, and talin, which are components for both two types of adhesions.[73-75] The released proteins may delocalize to reinforce cell-ECM adhesion. On the other hand, surface immobilized cadherin reduces the cell-ECM adhesion of epithelial cells and limits the formation of membrane protrusions.[76] The cell-cell adhesion of two individual myocytes also results in the disassembly of ECM-induced adhesion in the region close to the cell contact area.[77]

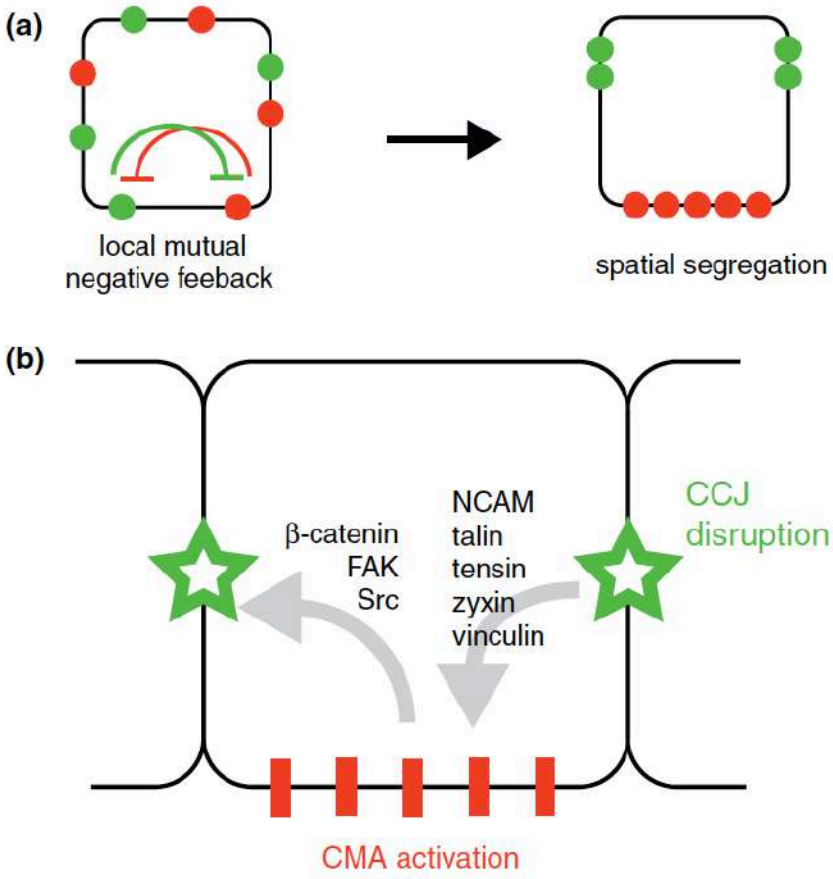

Figure 3.8 Spatial segregation of cell-ECM adhesion and cell-cell adhesion.[68] A: local negative feedback for the exclusion of two adhesions. Cell-ECM adhesion locally impairs cell-cell adhesion. B: Biochemical mechanism of spatial segregation of two adhesions. Cell-matrix adhesion (CMA) activates FAK, Src, β-catenin, thus causes the disassembly of cadherin complex. Cell-cell junction (CCJ) disruption results in the release of zyxin, vinculin, and talin, which may delocalize to reinforce cell-ECM adhesion. Reprinted with kind permission of Elsevier.

3.2 Detecting and measuring cellular forces

Cellular forces, which are forces generated by cells, play important role in cell biological events including cell adhesion, migration, morphogenesis, and

differentiation. Despite there are different types of cellular forces, we only focus on forces exerted by cells on surrounding substrates in this thesis. Cells apply mechanical forces on the substrates via 'mechanotransduction', a process of sensing and responding to cell surroundings.[78-79]

Scientists have been exploring methods used for detecting and measuring these cellular forces over the past decades. However, the application of developed methods on cells remains complicate. Multi-disciplinary cooperation is required for the interpretation of cell-generated forces into acceptable signal. There are different types of methods to detect and measure different cellular forces based on different assumptions, different technical and experimental constructions.[80] In General, these methods can be catalogued into two classes: one class is based on measuring deformation of substrates where cells adhere on/in; another class is molecular tension probes, which translate the molecular deformation into cellular forces.[80] Typical methods used for measuring cell generated forces on substrates are schemed in ***figure 3.9***.

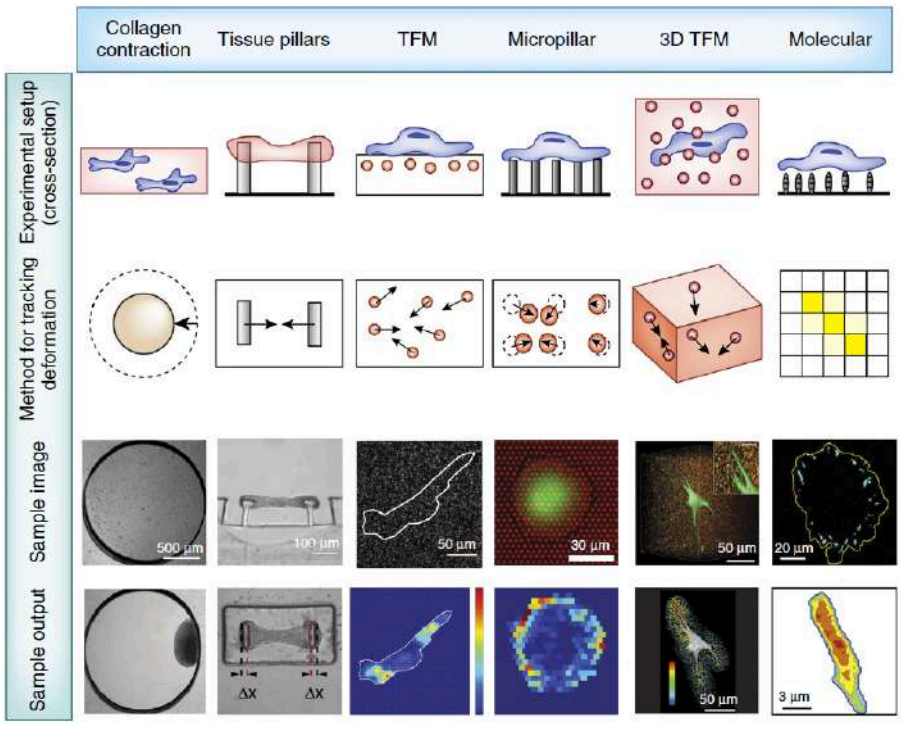

Figure 3.9 Typical methods for measuring cell generated forces.[80] By measuring the compaction of collagen gel which contains cells, cell traction force can be qualitatively characterized. Tissue pillars constituted of cantilevers can quantify cell traction force. Cell traction force microscopy of 2D or 3D measures cell generated forces by translating the displacement of fluorescent microbeads. Micropillar is also prospective method for measuring single cell force in high resolution. Molecular tension probes utilize functional molecules to quantify single cell force more accurately. Reprinted with kind permission of Springer Nature.

3.2.1 Deformation of substrate

As the simplest way, the deformation of cells or substrates can be measured without translating the deformation into actual force. For example, cells were embedded in collagen gel. Upon contraction force of cells, the collagen gel was compacted over a time period. By measuring this compaction, i.e. the change of gel diameter, cell traction force could be qualitatively characterized.[81] Although the application of this method is relatively easy, it has the drawback that the actual force is not obtained and it can not determine single cell forces.

Tissue pillars are also widely used for measuring cell contractile forces in a piece of tissue. Cantilevers of known stiffness are fixed as a substrate, on which cell contraction forces exert. The resulted bending or displacement of the free end of the cantilevers can be imaged by microscopy.[82] Wesley R. Legant et al fabricated microtissue gauges consisted of cantilevers to measure cell forces. Deep investigation was performed on matrix remodeling events, microtissue force generation, and reported rapid changes in microtissue force in response to soluble stimuli.[83] However,

this method still has the limitation that it cannot be used to determine single cell forces.

Cellular traction force microscopy (TFM) is a developed method, which can determine single cell traction force by obtaining measurements of the surrounding displacement field within an in vitro extracellular matrix (ECM). It is a typical way to study dynamic mechanical behavior of cell-ECM and cell-cell interactions. In a standard TFM, fluorescent microbeads (≤ 1 μm) are embedded in transparent 3D ECM substrates which are normally natural or synthetic hydrogels. These microbeads work as fiduciary markers that can be tracked in space and time with microscopy.[84-85] When cell traction force exerts, the displacement of fluorescent microbeads is recorded and transcript into cellular force computationally. The hydrogel substrate should be biocompatible to maintain cellular viability; and the mechanical properties of hydrogel substrate should be well characterized. Conventional TFM can be classified into 2D TFM and 3D TFM. In 2D TFM, fluorescent microbeads are mostly concentrated on the internal surface of hydrogel, while cells are seeded on the surface of the hydrogel. In 3D TFM, fluorescent microbeads are homogeneously distributed in 3D ECM, while cells are seeded inside the hydrogel.[80]

In general, a 2D or 3D TFM experiment is performed as the following process:[80] (1) Cells on the surface or inside the hydrogel exert traction forces on their surrounding hydrogel, causing a stressed state of fluorescent microbeads embedded. (2) The distribution of these stressed state microbeads are firstly optically imaged. (3) Forces are released upon treatments of cells, e. g. cell lysis,[86] detachment,[87] or myosin inhibition,[88] causing an unstressed state of fluorescent microbeads. (4) These unstressed state microbeads are imaged again. (5) The displacement of microbeads between unstressed state and stressed state are calculated by analyzing the resulted

two images computationally, and translated into cellular forces required for such displacement according to the known mechanical properties of hydrogel.

TFM is a powerful tool to study cell behavior related to cellular forces. Qingzong Tseng et al. used 2D TFM to investigate the effect of force on cell-cell junction positioning.[89] Wesley R. Legant et al. applied 3D TFM for measuring traction forces exerted by varieties of cells on their 3D surroundings.[90] Stacey A. Maskarinec et al. combined 2D TFM and 3D TFM to develop a method combining laser scanning confocal microscopy (LSCM) and digital volume correlation (DVC).[88] In this method, fibronectin (FN)-coated polyacrylamide gels containing fluorescent microbeads were fabricated as substrate for 3T3 fibroblasts migrating. Cellular force induced deformation of hydrogel was quantified in all three spatial dimensions: in-plane (x, y) and normal (z) displacements. This study revealed that cells explore their surroundings in all three dimensions. Normal forces play important role as well even in 2D migration. Both 2D TFM and 3D TFM can translate the displacement of fluorescent microbeads into cellular force map. 2D TFM can sense force range of 2-120 nN, from single cell or cell group, with spatial resolution of ~2 μm. 3D TFM is currently limited in single cell force with spatial resolution of ~5 μm.[80] In both methods, synthesis and functionalization of fluorescent microbeads embedded hydrogels are required. Cell treatments, for example cell lysis are also required which may induce extra difficulties.[80]

Besides TFM, micropillar method can also generate cellular force map by measuring the deformation of substrate. Micropillar method is similar to the tissue pillar method described above, since both of them measure the deformation of the substrate silicon rubber cantilevers. However, in micropillar method, cantilevers are normally in 0.5-10 μm range, much smaller than in tissure pillar method. Moreover,

they are fabricated in micropillar arrays, aiming at measuring the forces generated by single cells. This method is relatively easy for computation into force map. It does not require cell lysis as required in TFM, because the unstressed state of pillars is known. It also has the advantage that the stiffness of micropillars can be controlled by varying the length and width of the pillars.[80, 91-92] Saba Ghassemi et al fabricated poly(dimethylsiloxane) (PDMS) elastomer pillars with diameters of 2, 1, and 0.5 μm in hexagonal arrays. By measuring forces on these different micropillars, they revealed that local contraction caused by submicron scale myosin filaments plays important role in cell sensing the stiffness of the substrates.[93] Micropillar as a perspective cellular force measuring method, can measure cellular forces in a range of 50 pN-100 nN, from 1-10 cells, with spatial resolution of ~1 μm.[80] However, it cannot mimic the morphology of cell on ECM and the application in 3D measurement is limited.

3.2.2 Molecular tension probes

In the methods described above, cell traction force-induced deformation of substrate or displacement of fluorescent microbeads is measured. These traditional methods can normally sense nanonewton range forces, and the sensitivity is related to the stiffness of the substrate. Another class of methods for measuring cellular force is tension probes, which can quantify single cells or even single molecular scale forces of piconewton range. In these methods, functional molecules are commonly used to interact with cells and probe cellular forces.[80, 94-95]

Old topics include detecting cellular forces by atomic force microscopy (AFM), magnetic tweezers (MT), and optical tweezers (OT) and more. P. P. Lehenkari et al. functionalized AFM tip with RGD peptide, linked with PEG chain. Then integrin

binding forces were measured by probing cells containing integrins by this functionalized tip, which turned out to be around 32-97 pN.[96] Nadine Walter et al. used magnetic tweezers to investigate the cellular unbinding forces on gold nanopatterned surfaces. A cell with covalently bound magnetic beads adhered on nanopatterned surfaces of different spacing through integrin-ligand interactions. Then magnetic tweezer was utilized to exert a vertical force by lifting the cell. The results showed an increased unbinding force on smaller spacing nanopatterned surface.[97] Similar to magnetic tweezers method, a functionalized glass bead can be bound to a cell and pulled by optical tweezers. A piezoelectric-driven glass pipette displaces this glass bead. Kimihide Hayakawa et al. utilized optical tweezers to directly stretch actin stress fiber, resulting in an activation of mechanosensitive channel in human umbilical vein endothelial cells.[98]

In past years, scientists did much effort in the development of high-resolution 'molecular tension probes', or so called 'molecular force sensors'. These force sensors normally contain either a fluorophore and a quencher or a Förster resonance energy transfer (FRET) fluorophore pair. These fluorophore pairs are separated by an entropic polymeric molecular spring. The strain of the molecular spring, which is induced by cellular forces, can be measured since it is the function of the emission spectra of the fluorophores shift. These molecular tension probes are commonly immobilized on a cell culture surface, mostly targeting integrins and measuring integrin-based binding forces. They normally use PEG or DNA hairpin as molecular spring.[99-101] Stain of the spring can be converted into quantified cellular forces by either experimental calibration or theoretical calculation.[99, 101-103] Yang Liu et al fabricated RGD peptide containing molecular tension probes on gold nanopatterned surface, aiming to study integrin tension and actin dynamics during early focal

adhesion maturation. In this study, the quenching efficiency of Cy3B fluorophore as a function of distance from AuNP surface was calibrated by a range of DNA duplexes, so called nonlinear state estimation technique (NSET) calibration plot. Then the cell tension force, as a function of the change in fluorescence signal was calculated based on wormlike chain (WLC) model and NSET model.[99] Brandon L. Blakely et al developed a molecular tension probe consisted of DNA hairpins conjugated to fluorophore-quencher pairs. When cell traction force applied, the fluorophore-quencher pairs unfold and fluoresce. It gave the information of cell traction forces. The force within focal adhesions was identified by ROCK inhibitor and Rho activator, and thus was revealed to be heterogeneous and localized at their distal edges. In this study, the force required to unfold DNA hairpin was determined by a dual-beam optical trapping apparatus.[100] DNA hairpin as molecular spring can be designed to unfold under a variety of forces. Compared with traditional TFM methods, these molecular tension probes have advantages of higher resolution and sensitivity to cellular forces. They can measure cell-generated forces on glass, plastic, or other polymers, with which traditional TFM methods cannot achieve. However, one should notice that, molecular tension probes provide only the magnitude but not the direction of cellular forces.

Here we discussed only some of the reported methods for detecting and measuring cellular forces on substrates. There are also methods for detecting forces in cells, and methods for detecting single molecular binding forces. They are all powerful tools to understand cell behaviors affected and regulated by forces. However, the development of these methods still requires combination of biology, chemistry, physics, and computation, which remains great challenge.

3.3 Surface immobilization of specific ligands for cell adhesion

In the sections above, we discussed cell adhesion and adhesion force. Cell adhesion in lives involves the participation of enormous of biomolecules, which affect each other in a complicate way. Cell adhesion studies can be simplified by immobilizing specific ligands on model surfaces. In addition, the immobilization of specific ligands on material surfaces is important for the development of biomaterials and the application in biomedical engineering.

Cell-ECM adhesion on different surfaces is commonly studied by immobilizing appropriate RGD ligands on surfaces, which specifically target to integrins expressed by various types of cells. RGD ligands are normally covalently immobilized onto surfaces by different methods, according to the properties of the substrate surfaces. Daniel Hal Davis et al. immobilized RGDC peptide on silicon surface for fibroblast adhesion and proliferation study. Silicon surface was first modified by aminosilane, followed by the linkage of maleimide groups. RGDC peptide was finally immobilized onto the surface through maleimide-thiol reaction.[104] Ming-Hua Ho et al. immobilized RGDS peptide on chitosan scaffold via amide bonding between amino groups in chitosan and carboxyl groups in peptides, which enhanced the attachment of rat osteosarcoma cells on chitosan scaffold.[105] Compared with linear RGD sequences, cyclic RGDs are more effective ligand to interact with cellular integrins.[106] Yang Liu et al. constructed nanoparticle tension probes for investigating force impacted integrin clustering. Cyclic(RGDfK)C was firstly modified with NHS-azide through amine groups to render azide group. Thiol group was reacted with Cy3B-maleimide. Then the azide group was reacted with alkyne-PEG-thiol. The obtained Y-shape molecule containing RGD peptide and Cy3B fluorophore was immobilized onto gold

nanoparticles through Au-thiol reaction.[99] RGD peptides can also be introduced on or into hydrogels of different biocompatible materials. D. Guarnieri et al. conjugated RGD peptide onto NHS-activated PEG chain. The RGD containing hydrogels were formed by combining PEG chains with different concentrations of RGD-PEG chains.[107] F. Z. Cui et al. immobilized RGD peptide in hyaluronic acid hydrogel by activating hydrogel with 1,1-carbonyldiimidazole (CDI).[108] Besides immobilizing RGD peptides onto different surfaces, fibronectin or collegen IV can also be coated onto surfaces for cell adhesion studies.[76, 109]

Cell-cell adhesion is commonly studied by immobilizing cadherin proteins or functional HAV peptide sequence on surfaces. Dagmar Fichtner et al. achieved covalent and density-controllable immobilization of E-cadherin by producing E-cadherin-SNAP-12His-tag linker. The 12 histidine residues (12His) extracted the fusion protein out of the cell supernatant by Ni^{2+}-NTA affinity chromatography. The SNAP-tag covalently bound to the benzyl group by releasing of the guanine part of benzylguanine thiol (BGT), which was mixed with matrixthiol on gold surface by microcontact printing.[110] A prospective technique for immobilizing proteins in biomaterials is fusion of Fc domain of IgG with a target protein, such as cadherin. Functional domain of E-cadherin or N-cadherin is fused as N-terminal with the Fc domain of IgG, forming E-cad-Fc or N-cad-Fc. Then anti-IgG antibodies specifically recognize them. Arthur Ganz et al. achieved force measurement at N-cadherin contacts by immobilizing N-cadherin onto micropillars in two steps. Anti-IgG antibodies were first coated onto micropillars, followed by coating of N-cad-Fc.[111] HAV peptide can also be covalently immobilized on surface for cell adhesion study. Brian D. Cosgrove et al. covalently conjugated HAVDI peptide, together with RGD peptide, in hyaluronic acid hydrogel to study the mechanosensing of mesenchymal

stem cells. In this study, peptides with cysteine residues were linked to the backbone of hyaluronic acid with methacrylate via Michael-type addition reactions.[112]

4 Motivation

In an organized multicellular structure, cells adhere either to extracellular matrix (ECM) or to other cells. This adhesion is the molecular basis of tissue architecture and morphogenesis. It is crucial for the assembly of individual cells into three-dimensional tissues of animals. Cell-ECM adhesions are mainly mediated by integrin family, which connects extracellular proteins and cytoplasmic protein complex. Cell-cell adhesions are chiefly mediated by cadherin superfamily, by which cells are closely bound together. Integrin-mediated interactions and cadherin-mediated interactions have been continuously investigated, as they affect cell internal structure and decide cell fate jointly.

In order to decouple specific integrin or cadherin based interaction from enormous kinds of adhesive interactions and isolate the integrin-mediated or cadherin-mediated adhesions from the complex cell behaviors, one common method is immobilizing respective ligand proteins on biomaterials. This isolation can also endow biomaterials with specific properties to mediate cell behaviors for certain applications. However, proteins can be easily denatured and lose the activity during the fabrication process of biomaterials and are difficult to be precisely functionalized by active chemical groups. Protein mimetic peptides are therefore widely utilized as substitutes in materials science due to their high stability, simple synthesis, precise chemical structure, relatively low costs, and easy to use advantages. In this work, we concentrated to study cell-ligand interactions by immobilizing respective ligand peptides on 2D surfaces.

Cell adhesion force plays important role in cell behaviors including cell adhesion, signaling, function, and morphogenesis. Based on cell-ligand interactions, cells are

able to sense the mechanical cues in microniche and respond by applying cellular forces through mechanotransduction. Measuring cellular forces is important to understand cell behaviors and how cells respond to biochemical and physical stimulations. Several methods have been developed to detect and measure cellular forces, including substrate deformation-based methods and molecular tension probes. The former class is limited by the properties of substrate materials to fully mimic cell ECM. The latter systems are normally established by fluorophores, which suffer from saturation and photobleaching effects.

A new type of molecular tension probe was designed in this thesis by immobilizing RGD peptide and paramagnetic ion containing polymer on nitrogen-vacancy (NV) diamond to study integrin-induced cell adhesion force. NV diamond has been used as prospective quantum sensor due to the spin-dependent photoluminescence effect of NV centers. Atomic resolution imaging can be achieved.

In the second section, cadherin-induced cell-cell interaction was studied by immobilizing E-cadherin mimetic histidine-alanine-valine (HAV) peptide. Cadherin mimetic peptides are widely used in synthetic biomaterials to mimic cell-cell adhesion in cells microniches. This mimicry regulates various cell behaviors, including epithelia remodeling, signal propagation, cell migration and cell differentiation. Although the interaction between immobilized cadherin and cells has been studied in a set of work, it still lacks knowledge to understand the functions of the cadherin mimetic peptides. Since the peptides only mimic the critical amino acids sequence of the cadherin, they do not possess the equal function to proteins. On the other hand, peptides are more stable, easier to fabricate, and exhibit precise chemical composition, compared with proteins. E-cadherin mimetic peptide His-Ala-Val (HAV) was hereby

immobilized on material surfaces and the adhesion and clustering of epithelial cells were studied.

Overall, different types of cell-ligand interactions were studied by utilizing related biomimetic peptides in this thesis. These studies are expected to not only exhibit an overview of the cell adhesions, but also can assist the design of novel biomaterials.

5 Materials and Methods

5.1 Preparation of functional surfaces

5.1.1 Nitrogen-Vacancy (NV) diamond based force sensor

5.1.1.1 Silica (SiO_2) coating on NV diamond

Silica (SiO_2) coatings were always tested on silicon wafers with 1x1 cm^2, 500 μm thick, one side polished (Si-Mat, Germany) before applied on diamonds. Prior to SiO_2 coating, silicon wafers were washed in acetone (VWR International GmbH, Germany) and ethanol (Carl Roth GmbH, Germany) by ultrasound for 15 minutes, respectively. After being rinsed by distilled and deionized H_2O (ddH_2O), the silicon wafers were immersed in fresh Piranha solution, which is a 3:1 mixture of sulfuric acid (H_2SO_4, Carl Roth GmbH, Germany) and hydrogen peroxide (H_2O_2, Merck KGaA, Germany) for about 1 hour. Then they were rinsed thoroughly by ddH_2O and dried by nitrogen gas.

Two methods were developed to generate SiO_2 layers of different thickness on these clean silicon wafers. In the first step of both methods, (3-Aminopropyl)triethoxysilane (APTES, Sigma, Germany) was added into a mixture solvent of ethanol and ddH_2O. In the second step, for method *a*, tetraethyl orthosilicate (TEOS, Sigma, Germany) and ammonia solution 25% (Sigma, Germany) were added into a mixture solvent of ethanol and ddH_2O; while for method *b*, TEOS, 1,2-Bis(triethoxysilyl)ethane (BTSE, Sigma, Germany) and ammonia solution 25% were added. All parameters generating SiO_2 layers of different thickness by both methods are listed in ***table 5.1.1***.

Table 5.1.1 Silica coating parameters for method a and method b

Coating steps	Solvents	Method a (High concentration)	Method a (Low concentration)	Method b
1st step (2 h)	Ethanol 20 ml + H_2O 20 ml	APTES 400 µl	APTES 100 µl	APTES 100 µl
2nd step (1 h/1.5 h/2 h/3 h)	Ethanol 30.8 ml + H_2O 9.2 ml	TEOS 80 µl, Ammonia 720 µl	TEOS 20 µl, Ammonia 180 µl	TEOS 20 µl + BTSE 16.5 µl, Ammonia 180 µl

For coating silica layers on diamonds with NVs or without NVs, diamonds were always first washed by fresh Piranha and washed by ddH_2O. Then SiO_2 layers were obtained by method *a* or method *b* as on silicon wafers.

The SiO_2 layers on diamonds can be washed off by immersing the diamonds in saturated NaOH solution at 80 °C for over 12 hours.

5.1.1.2 Multi-step synthesis of Y-shape macromolecule

5.1.1.2.1 Synthesis of linear functional PEG molecule (without RGD peptide) by method *a*

Metal ion chelator 2,2',2"-(10-(4-((2-((((1R,8S,9s)-bicyclo[6.1.0]non-4-yn-9-ylmethoxy)carbonyl)amino)ethyl)amino)-1-carboxy-4-oxobutyl)-1,4,7,10-tetraazacyclododecane-1,4,7-triyl)triacetic acid (BCN-DOTA-GA, Chematech, France) 50 mg was dissolved in 1 ml ddH_2O, then transferred into 10 ml round-bottom flask, together with a clean stirrer. N-(3-Dimethylaminopropyl)-N′-ethylcarbodiimide hydrochloride (EDC, Sigma, Germany) 2.76 mg was dissolved in 1 ml ddH_2O and added into flask dropwise by syringe under stirring. After 2 hours of

stirring, Boc-NH-PEG-NH_2 with molecular weight 3000 Dalton (Iris Biotech GmbH, Germany) 39.8 mg was dissolved in 1 ml ddH_2O and added into flask dropwise by syringe under stirring. The reaction was kept at room temperature under stirring for 24 hours. The reaction solution was then transferred and dialyzed in H_2O for 24 hours. Boc-NH-PEG-DOTA (LS (A)-1) was obtained by freeze-drying.

Boc-NH-PEG-DOTA 20 mg was dissolved in 6 ml ddH_2O, subsequently 0.5 ml hydrochloric acid (HCl, Sigma, Germany) of 1 M was added. The reaction was kept in room temperature under stirring for 4 hours. H_2N-PEG-DOTA (LS (A)-2) was obtained by freeze-drying.

H_2N-PEG-DOTA 20 mg in round-bottom flask was set up in Schlenk line to insure water free condition. Extra dry dimethylformamide (DMF, Acros, Germany) 4 ml was taken and added into flask under argon flux to dissolve H_2N-PEG-DOTA. Then 4 µl 3-(triethoxysilyl)propyl isocyanate ($(EtO)_3Si$-NCO, Sigma, Germany) and 5 µl triethylamine (TEA, Sigma, Germany) were added into reaction flask under argon flux as well. The argon flux ran for 0.5 hour, then the reaction solution was kept closed in Schlenk system and kept stirring for 24 hours. The reaction solution was dialyzed in ethanol for 34 hours, then concentrated and dried under vacuum to yield the third product $(EtO)_3Si$-PEG-DOTA (LS (A)-3).

5.1.1.2.2 Synthesis of linear functional PEG molecule (without RGD peptide) by method *b*

Metal ion chelator BCN-DOTA-GA 22 mg in 25 ml round-bottom flask was set up in Schlenk line to insure water free condition. A mixture solvent of 3 ml methanol and 2 ml DMF was used to dissolve BCN-DOTA-GA under argon flux. Then 61 mg

$(MeO)_3Si$-PEG-N_3 of molecular weight 3000 Dalton (Iris Biotech GmbH, Germany) was added into solution under argon flux. The argon flux ran for 0.5 hour, then the reaction solution was kept closed in Schlenk system and kept stirring for 24 hours. The reaction solution was dialyzed in extra dry methanol until excess of BCN-DOTA-GA precipitated. After filtrating the excess of BCN-DOTA-GA, the reaction solution was further dialyzed in methanol for 2 days before being concentrated and dried under vacuum to yield the product $(MeO)_3Si$-PEG-DOTA (LS (B)).

5.1.1.2.3 Synthesis of Y-shape functional PEG molecule

$(MeO)_3Si$-PEG-N_3 28 mg in round-bottom flask was set up in Schlenk line to insure water free condition. Then it was dissolved by adding 4 ml extra dry DMF into flask under argon flux. Subsequently 8 mg (1R,8S,9s)-Bicyclo[6.1.0]non-4-yn-9-ylmethyl N-succinimidyl carbonate (BCN-NHS, Sigma, Germany) was added into flask under argon flux and dissolved in reaction solution. The reaction solution was kept stirring in Schlenk line for 6 hours to render $(MeO)_3Si$-PEG-NHS (YS-1) without further purification. Then cyclic(RGDfK)C (Peptide Specialty Laboratories GmbH, Germany) 15 mg and 6 µl TEA were added into flask under argon flux. The argon flux ran for 0.5 hour, then the reaction solution was kept closed in Schlenk system and kept stirring for 24 hours. The reaction solution was dialyzed in extra dry methanol for 3 days before being concentrated and dried under vacuum to yield $(MeO)_3Si$-PEG-RGD (YS-2).

$(MeO)_3Si$-PEG-RGD 35 mg in round-bottom flask was set up in Schlenk line to insure water free condition. Then it was dissolved by adding 4 ml extra dry DMF into flask under argon flux. 10 mg 2,2',2"-(10-(1-carboxy-4-((2-(2,5-dioxo-2,5-dihydro-1H-pyrrol-1-yl)ethyl)amino)-4-oxobutyl)-1,4,7,10-tetraazacyclododecane-1,4,7-

triyl)triacetic acid (maleimide-DOTA-GA, Chematech, France) and 6 µl TEA were added into flask under argon flux and dissolved in reaction solution. The argon flux ran for 0.5 hour, then the reaction solution was kept closed in Schlenk system and kept stirring for 24 hours. The reaction solution was dialyzed in extra dry methanol for 24 hours before being concentrated and dried under vacuum to yield the third product $(MeO)_3Si$-PEG-RGD-DOTA (YS-3).

5.1.1.2.4 Surface coating of Y-shape and linear functional PEG molecule

LS (B) and YS-3 were coated onto glass slides and silicon wafers for further experiments. All slides were first washed in acetone and ethanol by ultrasound for 5 minutes for each. After being rinsed by ddH_2O, slides were immersed in fresh Piranha for 1 hour. Then the slides were washed by ddH_2O and dried completely by nitrogen gas. The clean slides were put into flask and set up in Schlenk line to insure water free condition. 1 mM LS (B) or YS-3 in extra dry toluene solution was added into flask under argon flux, together with 4 µl TEA. The argon flux ran for 0.5 hour, then the reaction solution was kept closed in Schlenk system and kept at 80 °C for overnight. The coated slides were washed by ethanol, ddH_2O, and dried by nitrogen gas.

5.1.1.3 Bottom-up construction of Y-shape force sensor

All coating procedures were tested on glass slides, silicon wafers, and Q-sensor silica slides before being applied on silica-coated diamonds.

5.1.1.3.1 Linear bottom-up coating

All glass slides and silicon wafers were washed by the same procedure as described in 5.1.1.2.4. Qsensor slides were washed in acetone and ethanol, subsequently put in UV Ozone Cleaner (ProCleaner™ Plus, BioForceNanosciences) for 20 minutes. Then they were coated by 1 mM $(MeO)_3Si$-PEG-N_3 in extra dry toluene at water free condition by the same protocol in 5.1.1.2.4 to obtain LC-1 (N_3). LC-1 (N_3) slides were then reacted with 1 mg/ml BCN-DOTA-GA in DMF for 3 hours to achieve LC-2 (DOTA). After washed and dried, the slides were further reacted with 1 mg/ml 1-Ethyl-3-(3-dimethylaminopropyl)carbodiimide (EDC) and 1 mg/ml N-Hydroxysuccinimide (NHS) in DMF for 3.5 hours. After being washed by acetone and dried, the slides were further reacted with 0.2 mg/ml cyclic(RGDfK) (Peptide Specialty Laboratories GmbH, Germany) in DMF for overnight and LC-3 (RGD) slides were obtained. Gadolinium ions were loaded either on LC-2 (DOTA) or on LC-3 (RGD) by immersing the slides in 2 mg/ml $GdCl_3*6H_2O$ water solution for overnight.

5.1.1.3.2 Y-shape bottom-up coating 1st strategy

All glass slides and silicon wafers were washed by the same procedure as described in 5.1.1.2.4. Qsensor slides were washed in acetone and ethanol, subsequently put in UV Ozone Cleaner (ProCleaner™ Plus, BioForceNanosciences) for 20 minutes. Then they were coated by 1 mM $(MeO)_3Si$-PEG-N_3 in extra dry toluene at water free condition by the same protocol in 5.1.1.2.4 to achieve YC-1 (N_3). YC-1 (N_3) slides were then coated with BCN-NHS by immersing in 1 mg/ml BCN-NHS in DMF for 6 hours to achieve YC-2 (NHS). After being washed by acetone and dried, YC-2 (NHS)

slides were coated with cyclic(RGDfK)C by immersing in 0.2 mg/ml c(RGDfK)C in DMF containing 4 µl TEA as catalyst for 24 hours to achieve YC-3 (RGD). Then YC-3 (RGD) slides were coated with maleimide-DOTA-GA by immersing in 1 mg/ml maleimide-DOTA-GA in DMF containing 4 µl TEA and 0.1 ml $NaHCO_3$ as buffer for 24 hours to render YC-4 (RGD+DOTA). Finally gadolinium ions were loaded by immersing the slides in 2 mg/ml $GdCl_3*6H_2O$ water solution for overnight to achieve YC-5 (RGD+DOTA+Gd^{3+}).

5.1.1.3.3 Y-shape bottom-up coating 2nd strategy

YC-1 (N_3) and YC-2 (NHS) were obtained by the same procedure as described in 5.1.1.3.2. Then RGD-DOTA 2-in-1 molecule was obtained by reacting 1 equivalent of c(RGDfK)C and 1.2 equivalent of maleimide-DOTA together in DMF for 24 hours. YC-2 (NHS) slides were coated with RGD-DOTA molecule by immersing in RGD-DOTA (containing 0.1 mg/ml RGD) in DMF containing 2 µl TEA for 48 hours to achieve YC-3 (RGD + DOTA). Finally gadolinium ions were loaded by immersing the slides in 2 mg/ml $GdCl_3*6H_2O$ water solution for overnight to achieve YC-4 (RGD+DOTA+Gd^{3+}).

5.1.1.3.4 Y-shape bottom-up coating 3rd strategy

YC-1 (N_3) slides were obtained by the same procedure as described in 5.1.1.3.2. Then BCN-RGD-DOTA 3-in-1 Y-shape molecule (BRD) was obtained by reacting 1.5 equivalent of RGD-DOTA and 1 equivalent of BCN-NHS in DMF in the present of TEA as base for overnight. By the same procedure another 3-in-1 Y-shape molecule DBCO-RGD-DOTA (DRD) was obtained by reacting Dibenzocyclooctyne-PEG4-N-

hydroxysuccinimidyl ester DBCO-PEG_4-NHS (Synaffix BV, Netherlands) with RGD-DOTA. YC-1 (N_3) slides were coated with BRD or DRD molecules by immersing in BRD or DRD (containing 0.1 mg/ml RGD) in DMF or DMF/H_2O 1:9 mixed solution for 24 hours to achieve YC-2 (RGD+DOTA). Finally gadolinium ions were loaded by immersing the slides in 2 mg/ml $GdCl_3$*$6H_2O$ water solution for overnight to achieve YC-3 (RGD+DOTA+Gd^{3+}).

5.1.1.3.5 Y-shape bottom-up coating for Y-shape S

YC-1 (N_3) slides were obtained by the same procedure as described in 5.1.1.3.2 but using $(MeO)_3$Si-PEG-N_3 with molecular weight 800 Dalton. Then BRD molecule was obtained and coated onto YC-1 (N_3) in DMF by the same procedure as described in 5.1.1.3.4. Gd^{3+} ions were loaded by the same protocol as described in 5.1.1.3.4.

5.1.1.4 Surface immobilization of cell-simulated microbeads

Microbeads (beads A without BSA and beads B with BSA) with 6 μm diameter and with amine groups on the surface were kindly provided by Andrea Zappe (3. PhysikalischesInstitut, Stuttgart University). Both beads A and beads B were diluted into 1% wt by DMF. Then 20 μl of each bead solution was added into 500 μl 10 mg/ml BCN-NHS solution respectively. After being kept shaking for more than 48 hours, the two reaction tubes were put into centrifuge to remove the rest BCN-NHS. The beads were washed by ddH_2O for 2 times before being centrifuged to achieve BCN-beads A/B. Three kinds of glass surfaces were prepared: azide functional surface was prepared by coating $(MeO)_3$Si-PEG-N_3 (MW3000), PEG functional surface was prepared by coating $(EtO)_3$Si-PEG-OMe (MW2000, Iris-GmbH,

Germany), NHS functional surface was prepared by reacting BCN-NHS on azide functional surface. BCN-beads A/B and original amine contained beads A/B were loaded onto different surfaces in a concentration of 0.01% and the slides were kept shaking for over 48 hours. After the slides were washed by ddH_2O and dried by nitrogen gas, the images were taken by 20X objective microscopy.

5.1.2 E-cadherin mimetic HAV peptide functionalized surfaces

5.1.2.1 Homogeneous gold surface and gold nanostructured surface

Prior to the fabrication of gold surfaces, glass slides as substrates were first cleaned in acetone and ethanol by ultrasound for 5 minutes for each. Then they were immersed in fresh piranha solution for about 1 hour. Finally the glass slides were cleaned by deionized water thoroughly and dried by nitrogen gas.

Homogeneous thin layer gold (Au) surface was kindly provided by Frank Thiele (Department Schuez, MPI-IS). 10 nm titanium (Ti) was first sputtered onto glass slides, subsequently 25 nm gold was sputtered on top of Ti layer.

Gold nanoparticle (AuNP) structured surfaces with different spacing were fabricated as well. We used the protocol for depositing 9 nm AuNPs on glass surface by block copolymer micelle nanolithography (BCMN) using polystyrene-block-poly(2-vinylpyridine) (PS-b-P2VP), which is based on the previous work.[113-114] In order to fabricate 12 nm, 39 nm, 66 nm, 89 nm, and 112 nm inter-particle distance substrates, 5 different micelle solutions were prepared and deposited by spin coating with different parameters. 5 different polymers with different numbers of PS repeating units 154, 288, 1200, 501, 1824 (Polymer Source Inc, Canada) were

dissolved at different concentrations in extra dry toluene (Sigma, Germany). Different amounts of $HAuCl_4 \cdot 3H_2O$ (Sigma, Germany) were then added into the polymer solutions. Then these solutions were deposited onto clean glass slides by spin-coating method at different spinning speed. All parameters in fabricating different spacing AuNPs patterned surfaces, including polymers used, concentrations, gold loading values and spin-coating velocities, are listed in ***table 5.1.2***. By hydrogen plasma treatment (0.1 mbar, 200 W) for 45 minutes, organic compounds were removed, resulting in the coalescence of the 9 nm AuNPs with different spacing. The obtained AuNPs patterned surfaces were imaged by scanning electron microscope (SEM, Zeiss Ultra 55 SEM, Carl Zeiss AG Germany). Then they were passivated by silane-PEG with molecular weight 2000 Da (Iris-GmbH, Germany) at 80°C at water free condition for 18 hours, with triethylamine as a catalyst.

Table 5.1.2 Parameters for fabricating AuNPs patterned surfaces with different spacing

Achieved spacing (nm)	Polymer (repeating units of styrene)	Polymer concentration (mg/ml)	Loading	Spinning velocity (rpm)
12	154	4	0.3	4000
39	288	4	0.3	5000
66	1200	2	0.3	8000
89	501	3	0.3	12000
112	1824	2	0.3	5000

5.1.2.2 Substrate of traction force microscopy

Sterilized glass bottom Petri-dish 35 mm (D35-20-0-N, Cellvis, USA) was first activated by an activation solution constituted of 20 ml EtOH, 600 µl 10% acetic acid (in H_2O) (Sigma, Germany), and 100 µl 3-trimethoxysiylpropyacrylate (Sigma, Germany) at 65 °C for 3 hours. They were then washed by ddH_2O and dried by nitrogen gas. AuNPs patterned glass slides with 12 nm spacing were prepared according to the protocol in 5.1.2.1. Then polyacrylamide (PAAm) hydrogels containing fluorescent microbeads as well as AuNPs patterned surface were fabricated. A mixed solution containing 988 µl acrylamide/bis-acrylamide mixture (Sigma), 6.5 µl dye labeled beads (0.5 µm red) (L3280, Sigma), 5 µl ammonium persulfate (APS), and 0.5 µl tetramethylethylenediamine (TEMED) was added onto the AuNPs patterned glass slide. Subsequently, the droplet was covered by activated Petri-dish upside-down. After the gelation completely finished, the petri dish was turned over with gel inside and glass slide on top. By immersing in PBS for several days, the glass slide was removed, with AuNPs transferred onto the surface of PAAm hydrogel. The fluorescent microbeads were concentrated at the internal surface of PAAm hydrogel.

5.1.2.3 Immobilization of HAV peptide on gold surfaces

Peptides immobilization on these gold surfaces were achieved by immersing Au surfaces or AuNPs patterned slides in peptide solutions of 25 µM in H_2O for 18 hours at 4°C. Three peptides, RGD [cyclic(RGDfK)-(PEG5)2-C], HAV [LYS-HAV-SSNG-(PEG5)2-CCC], SCR [NSG-HYL-SVAS-(PEG5)2-CCC] (Peptide Specialty Laboratories, Germany) have been used. To obtain RGD, HAV, and SCR

immobilized surfaces, slides were immersed in related peptide solutions. To obtain RGD/HAV or RGD/SCR mixed immobilized surfaces, slides were immersed in RGD:HAV 1:400 or RGD:SCR 1:400 mixed peptide solutions. For traction force microscopy, hydrogels were immersed in RGD: HAV1:9, or RGD:SCR=1:9 mixed peptide solutions.

5.2 Characterization methods

5.2.1 Substrate characterization

5.2.1.1 Scanning electron microscope (SEM)

A scanning electron microscope (SEM) provides sample images by scanning the surface with a focused beam of primary electrons (PE) of approx. 1-10 keV. A lens system focuses the electron beam on the sample surface to a spot of 1-10 nm in diameter. The information about the sample is gained by the interaction of the sample with the electrons. Both the interaction of the primary electrons with the surface and the diameter of the electron probe determine the resolution of SEM images.

The incident primary electron beam causes several interactions with the sample. Primary electrons can be scattered inelastically by interaction with atomic electrons generating secondary electrons (SE). Their kinetic energy is < 100 eV. They derive from a depth of 1 - 2 nm of the sample. The detection of SE provides the information of surface morphology of the sample, which is a common use of SEM. PE can also be scattered elastically by electrostatic interaction with atomic nuclei generating backscattered electrons (BSE). BSE have high kinetic energy (> 100 eV) and are detected at an angle of > 90°. They emerge from deeper locations within the sample.

Therefore the resolution of BSE images is lower than SE images. However, BSE images can provide information about the distribution of different elements in the sample, making it possible to be used in analytical SEM.

The gold nanoparticle (AuNP) patterned surfaces were imaged by SEM after plasma treatment. To prevent charging of the non-conductive sample due to electron irradiation, the surfaces were coated with a thin conductive layer of graphite (approx. 10 nm) using a sputter coater (BAL- 47 Material and Methods TEC MED 020). Imaging was performed using Zeiss Ultra 55 SEM (Carl ZeissAG Germany) by a 50,000X magnitude. Spacing of the gold nanoparticles was analyzed by the dot analyzer plugin created by Dr. Philippe Girard for ImageJ (Research Services Branch, Image Analysis Software, NIH, USA).

5.2.1.2 Ellipsometry

Ellipsometry measures the change in polarization when light reflects or transmits from a material structure. The polarization change is represented as an amplitude ratio, Ψ, and the phase difference, Δ. The measured response depends on the optical properties and the thickness of individual materials. Therefore, ellipsometry is primarily used to determine film thickness and optical constants of a material.

Light can be described as a plane wave, which consists of electric field vector $\boldsymbol{E}$ and wave vector $\boldsymbol{k}$, $\boldsymbol{E} \perp \boldsymbol{k}$. $\boldsymbol{k}$ indicates the direction of light propagation. $\boldsymbol{E}$ oscillates only in the polarization direction after the light pass through a polarizer, so-called linear polarized light. The ***s***-component $\boldsymbol{Es}$ is perpendicular to the plane of incidence, and the ***p***-component $\boldsymbol{Ep}$ is parallel to the plane of incidence. When the linear polarized light passes through the compensator, which is set after polarizer, there will be a phase shift of these two components described by amplitude ratio Ψ, and the phase

difference Δ. After the light is reflected on the material, there will be again a phase shift depending on material thickness and optical properties, which is collected by analysator on the other side. By adjusting the angles of polarisator and analysator, the phase shift caused by materials is compensated via that caused by compensator. Then the reflected light is a linear polarized light and the intensity detected by the detector should be zero. This is so-called null ellipsometry. According to the ellipsometry equation and the angles of polarisator and analysator, Ψ and Δ can be calculated, in order to give the thickness and optical information of material.

Silicon wafers with different steps of coatings were tested by ellipsometry (M-2000V, EC-400, J. A. Woollam). A model of Si with native oxide of 1.53 nm was used to fit out the thickness of silica layer coated on silicon wafer. A model of three layers constituted of Si, fixed SiO_2 1.53 nm and PEG on top was used to fit out the thickness of PEG coating of different steps.

5.2.2 Surface analysis

5.2.2.1 Quartz crystal microbalance with dissipation monitoring (QCM-D)

A QCM sensor consists of a thin quartz disc sandwiched between a pair of electrodes. The electrodes are normally made of gold, which can be coated with a wide range of different materials. By applying an AC voltage across the electrodes, the quartz crystal can be excited to oscillation due to the piezoelectric properties of quartz. The resonance frequency (f) of the sensor depends on the total oscillating mass, including solvent in the system (normally water) coupled to the oscillation. The frequency decreases when a thin film is attached to the sensor. If the film is thin and rigid，the

decrease in frequency is proportional to the mass of the film, which can be described by Sauerbrey relation.[115] The mass of the adhering layer can be calculated as: $\Delta m = -(C \cdot \Delta f)/n$, $C = 17.7$ ng Hz^{-1} cm^{-2} for a 5 MHz quartz crystal. n = 1, 3, 5, 7 is the overtone number. In this way, the QCM behaves as a very sensitive balance. Compared with other QCMs, QCM with dissipation (QCM-D) has the advantage of monitoring the frequency and energy dissipation response of the freely oscillating sensor, thus generating results more accurately and faster.

In this thesis, Qsense with open module was used in both part I and part II. In part I, QCM-D was used to determine the reaction amount from each step of bottom-up strategies. The bovine serum albumin (BSA, PAA Laboratories, Inc) adsorption on Y-shape constructed surfaces was tested by QCM-D. Qsensors with silica layer were cleaned and coated with silane-PEG-N_3 as the protocol described in 5.1.1.3.1. Baseline was run either in 200 µl water or in 200 µl DMF, depending on the relative loading reactants. 200 µl reactants with the same concentration as described in 5.1.1.3 were loaded for 1 hour, followed by water or DMF washing. For BSA adsorption, after PBS baseline was run for a short time after Y-shape construction, 200 µl 2 mg/ml BSA in PBS was loaded followed by PBS washing. In part II, QCM-D was used to determine the adsorption amount of E-cadherin (R&D systems, cat. 8505-EC-050) and fetal bovine serum (FBS, Gibco, Thermo Fisher Scientific, USA) on peptide immobilized Qsensors. First of all Qsensors with Au layer were cleaned as the protocol in 5.1.1.3.1. For peptide immobilization, the cleaned Au sensors were immersed in 25 µM HAV or SCR peptide in H_2O for 18 hours at 4°C, as described in 5.1.2.4. For E-cadherin adsorption, baseline was run in 200 µl PBS with 0.01 mg/ml $CaCl_2$, (Sigma, Germany) in a static modulus. Then 10 µg/ml E-cadherin in PBS with Ca^{2+} was loaded onto the peptide immobilized Au sensor for 1.5 hours, followed by

washing with the same PBS solution for three times, each time 5 minutes. Afterwards slides were washed by 2% Hellmanex for 30 minutes, before being washed by PBS three times again. For FBS adsorption, baseline was run in 200 µl PBS. Then PBS containing 5% FBS was loaded for 15 minutes, followed by PBS wash for three times. The original data was condensed and export as excel data by Q-Tools software. The figures show representative data from F3 and D3.

5.2.2.2 Water contact angle

The contact angle is conventionally measured through the liquid, where a liquid-vapor interface meets a solid surface. It quantifies the wettability of a solid surface by the shape of a liquid via the Young-Laplace equation. A given system of solid, liquid, and vapor at a given temperature and pressure has a unique equilibrium contact angle which reflects the relative strength of the liquid, solid, and vapor molecular interaction.

In general, if the water contact angle is smaller than 60°, the solid surface is considered hydrophilic and if the water contact angle is larger than 60°, the solid surface is considered hydrophobic.[116]

Water contact angle (Dataphysics Contact Angle system OCA, DataPhysics Instruments) was used to determine the wetting ability of functional surfaces in different steps in bottom-up coating strategies as shown above. Water dispense volume was 1 µl at a medium rate. Contact angle was calculated by Laplace-Young fitting.

5.2.2.3 X-ray photoelectron spectroscopy (XPS)

X-ray photoelectron spectroscopy (XPS) is a surface-sensitive quantitative spectroscopic technique that measures the elemental surface composition (except for H and He) and the electronic structure of a material. By irradiating a material with a beam of X-rays, photoelectrons are escaped from the material when atom inner electrons or valence electrons are excited. XPS spectra are obtained by analyzing the kinetic energy and number of photoelectrons escaped from the top 0 to 10 nm of the material. XPS spectrum is constituted by the number of the detected photoelectrons versus the binding energy of the related photoelectrons. Each element from the analyzed material exhibits specific peaks at the characteristic binding energy values. These peaks are related to the configuration of the atom electrons, e.g., 1s, 2s, 2p, 3s, etc. The amount of the elements can be analyzed by the numbers of the detected photoelectrons. However, the raw signal must be divided by relative sensitivity factor (RSF) and normalized over the analyzed elements, in order to obtain element percentage values.[117]

In this work, functional PEG coated surfaces were analyzed with the help of Kathrin Müller (Interface Analysis Service Group, MPI-IS, Stuttgart) and Michael Noeske (Fraunhofer IFAM, Bremen). The XPS measurements were performed on a Kratos system with 4×10^{-10} mbar base pressure, sample neutralization applying low energy electrons, hybrid mode, take off angle of electrons (0°), pass energy (160 eV), and excitation of photoelectrons by monochromatic $Al_{k\alpha}$ radiation ($h\nu$ = 1486.6 eV) at 300 W (15 kV Å~ 20 mA). The detected region was elliptically shaped (300 μm × 700 μm for main axes).

5.2.3 Molecular synthesis analysis

5.2.3.1 Mass spectrometry (MS)

Mass spectrometry is a powerful analytical technique that measures the masses of molecules in a sample. It can be used to identify unknown molecules within a sample, and to elucidate the structures and chemical properties of different molecules. Mass spectrometry is applied to pure samples as well as complex mixtures and can be used in many different fields.

The molecules need to be first converted into gaseous ions by different ionization source. The ionic fragmentation may be generated from the molecules. The gaseous ions are then be detected according to the mass-to-charge ratio (m/z) and the relative abundances. The mass spectrum of molecules is further produced, by converting the ions into electrical signals and processing the signals from the detector that are transmitted to the computer. The spectrum displays the ion abundance versus m/z value. The structure of the original molecules can be expected from the mass of the ions.[118]

In this work, the reaction of BCN-RGD-DOTA 3-in-1 Y-shape molecule was detected with the help of Dr. Stephan Rauschenbach (Nanoscale Science Department, Max-Planck-Institute for Solid State Research) by a homebuilt, linear, orthogonal extraction Time-of-flight mass spectrometry (TOFMS). First the reaction between c(RGDfK)C and maleimide-DOTA-GA was detected by mixing them together with different equivalent ratios: 1:1.1, 1:1.5, 1:2, 1:5. The reactions were kept in DMF at the concentration of 0.1 mg/ml for c(RGDfK)C for 1 day. Then the solutions were diluted by methanol into 1.4×10^{-4} M for c(RGDfK)C. Two references of c(RGDfK)C and maleimide-DOTA-GA at the same concentration were also prepared.

Secondly the reaction between BCN-NHS and RGD-DOTA was detected by mixing them with different equivalent ratios: 1: 1.2, 1: 1.5, 1: 2. 2 μl TEA was added as catalyst in each solution. The reactions were kept in DMF at the concentration of 0.1 mg/ml for c(RGDfK)C for 1 day, then diluted by methanol into 1.4×10^{-4} M for c(RGDfK)C. Another solution of BCN-NHS in the same concentration was also prepared as a reference.

5.2.3.2 Proton nuclear magnetic resonance spectroscopy (NMR)

Proton nuclear magnetic resonance (proton NMR, hydrogen-1 NMR, or 1H NMR) is a high precise technique to determine the structures of molecules, based on the application of nuclear magnetic resonance in NMR spectroscopy with respect to hydrogen-1 nuclei within the molecules.

Hydrogen nuclei are sensitive to the hybridization of the atom to which the hydrogen atom is attached and to electronic effects coming from the chemical environments. Upon application of an external magnetic field, these electrons in the environment move in response to the field and generate local magnetic fields that oppose the much stronger applied field. This local field thus "shields" the proton from the applied magnetic field, which therefore must be increased in order to achieve resonance. This “shielding effect” can be described by chemical shift δ, which is usually expressed in parts per million (ppm) by frequency.[119] Nuclei tend to be deshielded by groups that withdraw electron density. Deshielded nuclei resonate at higher δ values, whereas shielded nuclei resonate at lower δ values. For instance, the proton peak from an aldehyde is shifted ca. 10 ppm compared to a hydrocarbon peak, since the carbonyl as an electron-withdrawing group deshields the proton by reducing the local electron density.

Since simple NMR spectra are often recorded in solution, using of deuterated (deuterium = ^2H, often symbolized as D) solvents can prevent the interference from solvent protons. Previously, a small amount of tetramethylsilane (TMS), typically 0.1%, can be added into the deuterated solvents to work as an internal marker. Therefore only one single signal can be obtained from the protons in TMS, which is defined to be chemical shift δ= 0 ppm to calibrate the shifts of the analyzed protons.[120] In a modern way, the residual proton in the solvent (e.g. the $CHCl_3$, 0.01% in 99.99% $CDCl_3$) can be used for calibration, since the TMS is volatile.

The shape and area of peaks are indicators of chemical structure. Software allows analyzing the intensity of peaks by calculating the area under a curve, which correlates with the number of protons of the related molecules.

In this work, all synthesized products in 5.1.1.2 were analyzed with the help of Dr. Günter Majer (New Materials and Biophysics Department, MPI-IS) and Dr. Igor Moudrakovski (Physical Chemistry of Solids Department, MPI-FKF) by a nuclear magnetic resonance spectrometer JEOL 400YH (JEOL, USA) at 300MHz. For each product, 600 µl of chosen deuterated solvent were used to dissolve all of the products, which were then transferred into NMR tube for test. The results were analyzed by software Delta V5.0.4.

5.3 Cell experiments

5.3.1 Cell culture

In Part I, MC3T3 cell line and Lifeact-Madin-Darby Canine Kidney (LA-MDCK) cell line were used. In Part II, Lifeact-Madin-Darby Canine Kidney (LA-MDCK) cell line was used. MEM (Gibco, Thermo Fisher Scientific, USA) with a supplement of 10%

Fetal Bovine Serum (Gibco, Thermo Fisher Scientific, USA) and 1% Penicillin Streptomycin (Gibco, Thermo Fisher Scientific, USA) was used as a growth media for MC3T3 cells. For LAMDCK cells, Dulbecco's Modified Eagle Medium + GlutaMAX (DMEM, Gibco, Thermo Fisher Scientific, USA) with a supplement of 5% Fetal Bovine Serum (Gibco, Thermo Fisher Scientific, USA) and 1% Penicillin Streptomycin (Gibco, Thermo Fisher Scientific, USA) was used as a growth media. Cells were cultured at 37 °C in a humidified atmosphere with 5% CO_2 and were harvested by 0.05% trypsin-EDTA (Gibco, Thermo Fisher Scientific, USA) treatment for 7 minutes for LAMDCK cells, and 5 minutes for MC3T3 cells. In the experiments in the presence of RGD peptide in Part II, Opti-MEM Reduced Serum Medium (Opti-MEM,Gibco, Thermo Fisher Scientific, USA) containing 1% Penicillin Streptomycin, 0.5% Bovine Serum Albumin (w/v) (PAA Laboratories, Inc), HEPES (Sigma, Germany) as a concentration of 50 mM, with final pH 7.4 was used. In all cell experiments, the functional surfaces in Part I and Part II were sterilized by 70% ethanol, and then were washed by sterilized PBS for three times.

5.3.2 Cell adhesion and cell mobility

In Part I, MC3T3 cell adhesion and LAMDCK cell adhesion experiments were carried out on Y-shape force sensor constructed slides. In Part II, LAMDCK cell adhesion experiments were carried out on different peptides immobilized surfaces. In all cell adhesion experiments, a cell density of 4000/cm^2 was used. After 1 hour and 4 hours of culturing, cells were imaged.

Cell mobility experiments were carried out in Part II. The peptide immobilized slides were glued onto 6-well plate by picodent twinsil speed22 before sterilization. Then a density of 3333/cm^2 of LAMDCK cells was loaded onto slides.

5.3.3 Cell monolayer experiments

Cell monolayer experiments were performed in Part II. The wells of 96-well plates were first coated by 20 μg/ml fibronectin in PBS. 0.05 million LAMDCK cells were seeded into each well. The cells were cultured for 18 hours in growth medium DMEM until cell monolayers were formed. Then they were incubated with 4 mM ethylene glycol tetraacetic acid (EGTA, Sigma, Germany) in 50 mM HEPES buffer for 30 minutes, in order to disrupt the cell-cell contact of the monolayer. After washed by PBS, the treated monolayers were incubated with 0.5 mM HAV or SCR peptide in growth medium.

5.3.4 Cell clusters

Cell cluster experiments were performed in Part II. To prepare cell clusters, cells were seeded in 6-well plate with peptide functional slides in a density of 0.06 million/cm^2 and cultured till the size of cell clusters reached 30-60 cells per cluster. It normally required 4-5 hours. The clusters were then imaged under microscope and the circularity of the cells in clusters was analysed by ImageJ. The cells on the border of the clusters were excluded from analysis.

5.3.5 Traction force microscopy

Traction force microscopy was performed in Part II. In 35 mm petri-dish containing peptide immobilized PAAm hydrogel with fluorescent microbeads embedded, 3 ml LAMDCK cell medium was added. Cells were harvested and loaded onto the gel in

dish by a density of 3333/cm^2. Then the gel with cells loaded was incubated until the cells started to spread. CO_2 and temperature on fluorescence microscope was opened the night before. Dish was then put into the microscope incubator and fixed by rubber band. A time-lapse program imaged cells and beads separately. Finally, cell medium was taken out, cells were washed by warm PBS without touching the microscopy stage. After treated by warm trypsin for at least 15 minutes, cells were washed off by warm PBS. Images at the same positions were taken, regarded as reference images without cell force.

5.4 Biochemistry methods

5.4.1 Fibronectin adsorption

In Part I, fibronectin non-specific adsorption was performed to confirm the anti-fouling effect of silane-PEG-N_3 coated surface. The silane-PEG-N_3 coated surface was incubated by 118 μg/ml fluorescein isothiocyanate (FITC) labeled fibronectin at room temperature for 0.5 hour avoiding light. A bare glass slide was tested as well by the same procedure as a reference. Images were acquired on Axiovert 200 M - Carl Zeiss Microscope.

5.4.2 Inhibition experiments

Inhibition experiments were carried out in Part II. To block HAV-induced cell adhesion, 20 μl of 8 mg/ml HAV or SCR in H_2O solution was added into 2 ml Opti-MEM right after loading LAMDCK cells on peptide immobilized slides. To block E-cadherins on cell surface, cells in culture were first washed by PBS, and then

incubated with 0.5 mM EDTA (Sigma, Germany) in PBS solution for 10 minutes to impair cell-cell contact. Cells were subsequently harvested by trypsin treatment for less than 3 minutes. A part of the harvested cells was incubated with 10 μg/ml anti-E-cadherin (ab11512, Abcam) on ice for 15 minutes. The rest cells were incubated on ice without any antibody for 15 minutes as a control group. After adding cells onto respective samples, the antibody blocking samples were further treated by anti-E-cadherin in 10 μg/ml for constant blocking. For blebbistatin inhibition experiments, 10 μM blebbistatin (Sigma, Germany) was added into the cell culture media.

5.4.3 Immunostaining

In Part II, immunostaining was used to visualize focal adhesions and adherens junctions in cells. LAMDCK cells were loaded onto sample surface by a density of 2000/cm^2 in 6-well plate, and fixed after 4 hours of incubation by 4% paraformaldehyde (Sigma, Germany) at room temperature for 15 minutes. Fixed samples were then washed three times with PBS. Afterwards cells were treated by 0.25% (v/v) Triton-X 100 (Sigma, Germany) in PBS for 10 minutes at room temperature for permeabilization and washed three times with PBS to remove the detergent. Then non-specific antibody binding was blocked by incubating the samples with 1% (w/v) Bovine Serum Albumin (BSA) in PBST (0.1% v/v Triton-X 100 in PBS) at room temperature for 45 minutes and washed briefly with PBST. Next, the samples were incubated with the primary antibody diluted in PBST with 1% BSA for 1 hour at room temperature and washed twice with PBST then three times with PBS. After that, samples were incubated with the secondary antibody diluted in PBST with 1% BSA for 1 hour at room temperature and washed twice with PBST then three times with PBS. Finally samples were transferred to glass bottom well-plate upside-

down in PBS with 1% Penicillin Streptomycin and 1 µg/ml DAPI. Immunofluorescence images were acquired on Axiovert 200 M - Carl Zeiss Microscope.

Primary antibodies used were 1:50 mouse anti-vinculin (v9131, Sigma-Aldrich), 1:100 rat anti-E-cadherin (ab11512, Abcam), and 1:50 mouse anti-β-catenin (610154, BD Pharmingen). Secondary antibodies used were 1:500 Alexa Fluor 568 linked anti-mouse IgG (A11031, Thermo Fisher Scientific) and 1:500 Alexa Fluor 647 linked anti-rat IgG (A21247, Thermo Fisher Scientific).

5.4.4 SDS-PAGE and western blot

In Part II, western blot was used to quantify analyze the protein expression within LAMDCK cells on different peptide immobilized samples. Prior to western blot, SDS-PAGE with 8% acrylamide, 1 mm spacer was fabricated. Two clean glass slides (one with spacer 1 mm and a smaller one without) were mounted in fixing device, with smaller glass in front. The bottom was kept straight and sealed with 1 cm wide parafilm. A mark was made at clamp for separating gel. Then glasses with fixing device were put into a pouring device, with smaller glass in front. Afterwards all components for separating gel were pipetted together according to ***table 5.4.1***. Solution was mixed carefully to avoid generating bubbles. When TEMED was added, the mixture was immediately filled into the gap between glasses till mark (about 5 ml per gel). 200 µl isopropanol was put on top of the solution to remove the bubbles. It required 30 minutes for sufficient polymerization at room temperature. Then most of the isopropanol was then removed by tissue paper and the trace rest could be evaporated. Components of collecting gel were then pipetted together according to ***table 5.4.2***. When TEMED was added, mixture was filled on top of separating gel. A

pocket device with 1 mm spacer was immediately inserted into the gel between glass slides.

Table 5.4.1 Components for 8% separating gel

Gel concentration	Milli Q water (ml)	30 % acrylamide (ml)	1.5 M Tris (ml)
8 %	9.3	5.3	5

Table 5.4.2 Components for 5% collecting gel

Gel amount (ml)	Milli Q water (µl)	30 % acrylamide (µl)	1 M Tris (µl)	10 % SDS (µl)	10 % APS (µl)	TEMED (µl)
8	5500	1300	1000	80	80	8

In order to extract total cell proteins, LAMDCK cells of density 12000/cm^2 were seeded onto samples in 12-well plate. After incubation in Opti-MEM for 5 hours, cell medium was removed and cells were lysed without washing by Pierce RIPA buffer with supplements of Halt Protease&Phosphatase inhibitor and EDTA at mixed ratio 100:1:1 (Thermo Fisher Scientific, USA) on ice for 5 minutes. Each sample was covered completely by 50 µl buffer solution. Then each slide was scratched by a scraper and all the liquid was collected into eppendorf tubes then centrifuged in 16 rcf for 15 minutes at 4°C to remove the unsolved impurities. Proteins in cell lysates were colored by Quickstart Bradford Dye Reagent (BIO-RAD, Germany), and the relative concentration was tested by Tecan Infinite M200 Plate Reader. Afterwards, all samples were adjusted to contain identical concentrations by diluting with RIPA buffer.

Then western blot analysis was carried out according to the procedure described in the following. 20 µl sample (cell lysate) was mixed with 20 µl 2X Laemmli sample buffer (constituted by 2X 90 µl Laemmli buffer and 25 µl DTT). The sample mixture was heated for 5 minutes at 95 °C and kept on ice until loading. At the same time gel apparatus was prepared by putting gel into gel holder and fill basin with 1X Laemmli buffer. The pocket device was removed. 39 µl sample mixture was then loaded into each pocket of the gel. 5 µl of molecular weight marker (26619, Thermo Fisher Scientific) was added into the first well. Gel was run at 130 V for roughly 1 hour until the lowest molecular weight coming down. While it was running, new transfer buffer was prepared according to ***table 5.4.3***. Then gel was equilibrated in transfer buffer for 10 minutes on the shaker to remove detergent. Nitrocellulose membrane was also equilibrated for 10 minutes, soak sponges (X2) and filter pater (X2) as well. Cassette was assembled as following: black side of cassette, sponge, filter paper, gel, nitrocellulose membrane, filter paper, sponge, clear side of cassette. Cassette was folded and placed in rack, together with ice tray. Transfer buffer was added in order to cover membranes completely. The gel with nitrocellulose membrane was run at 100 V for about 1 hour. At the same time 500 ml blocking buffer was prepared according to ***table 5.4.4***. After running at 100 V, proteins were transferred onto nitrocellulose membrane. The transferred proteins were confirmed by incubating with 1 M Poucau in 0.1 % acetic acid for 5 minutes. Nitrocellulose membrane was then cut out according to locations of different molecular weight of different proteins. The pieces were put in blocking buffer for 1 hour in the cold room. Then they were washed for 3 times in washing buffer PBST for 5 minutes for each. Primary antibodies were diluted into 5 ml filtrated BSA/PBST buffer, and the membranes were immersed in it for overnight on shaker at 4ºC. On the second day they were washed for 3 times in

washing buffer PBST for 5 minutes for each. Secondary antibodies were diluted into 5 ml filtrated BSA/PBST buffer, and the membranes were placed inside for 1-2 hours on shaker at room temperature. The membranes were finally washed for 6 times in washing buffer PBST for 5 minutes for each. The primary antibodies and secondary antibodies used are listed in ***table 5.4.5***.

Table 5.4.3 Components for transfer buffer

Tris (g)	Glycine (g)	Methanol (ml)	Distilled water (ml)
3.03	14.4	200	400

Table 5.4.4 Components for blocking buffer

1 M Tris pH 7.44 (ml)	NaCl (g)	Tween 20 (µl)	Nonfat milk (g)	Distilled water (ml)
12.5	4.383	500	5	487.5

Table 5.4.5 Antibodies used in western blot analyze

Antibody types	Sources	Dilution ratios
Primary antibodies		
rabbit anti-E-cadherin	Sc-7870, Santa Cruz Biotechnology	1:1000
mouse anti-β-catenin	610154, BD Pharmingen	1:500
mouse anti-β1-integrin	610468, BD Biosciences	1:2000
rabbit anti-β3-integrin	AB1968, Merck Millipore	1:1000
mouse anti-β-actin	A1978, Sigma-Aldrich	1:2000
Secondary antibodies		
anti-rabbit HRP-conjugated IgG	7074, Cell Signaling Technology	1:2000
anti-mouse HRP-conjugated IgG	7076, Cell Signaling Technology	1:2000

Chemiluminescence was detected by Fujifilm LAS-3000 Imager and associated with Amersham ECL Prime Western Blotting Detection Reagent (GE Healthcare). The detection solution ECL Plus Detection Kits was first equilibrated at room temperature for 20 minutes. Then component A (luminol) and component B (peroxide) were mixed together in a ratio of 1:1 to a working solution of 5 ml. The excess wash buffer from the washed membranes was drained and membranes were placed together in a suitable box with proteins side up. Detection reagent was added onto the membrane, making sure the membrane was completely covered by it. The membrane was incubated by detection reagent for 5 minutes at room temperature in dark. Then excess detection reagent was drained off by holding the membrane edge gently against a tissue. The membrane with proteins side up was put onto a sample tray, which was then placed in Fujifilm LAS-3000 Imager with a CCD camera. Suitable function and exposure time were selected, in order to get proper images of protein bands. ImageJ was used to determine the intensity of E-cadherin, β-catenin, β1-integrin, β3-integrin, and β-actin bands.

5.5 Cell imaging and data analysis

5.5.1 Cell imaging

MC3T3 cell adhesion images and LAMDCK cell fluorescence images were taken under Axiovert 200 M - Carl Zeiss. LAMDCK cell mobility time-lapse images were taken by the same microscopy under 10X objective in time-lapse program. The microscopy was equipped with a homebuilt incubation chamber for constant temperature of 37 °C and 5% CO_2 pressure. LAMDCK cell traction force microscopy

images were taken by the same microscopy in time-lapse program as well, under 20X objective. Cells and microbeads beneath were focused and imaged separately.

5.5.2 Image processing and data analysis

All images were processed by ImageJ software. Brightness and contrast of microscopy images were adjusted for the presentation. The software was further used to measure cell area in phase contrast images and to quantify bands of western blots. Cell velocity was analyzed by a manual tracking plugin, cell detach ratio was obtained by counting the contact times and detach times of all cells within a video. In traction force microscopy, fluorescence beads images were first aligned by template matching plugin. The displacement field in a spread cell region was subsequently calculated by a particle image velocimetry (PIV) plugin. The obtained result was reconstructed by the Fourier transform traction cytometry (FTTC) plugin, in order to generate traction force field as a vector plot. Background subtraction was applied on the images using the mean intensity of a selected ROI (region of interest) and subtracting the obtained value from each pixel within the image.

Data were analyzed by GraphPad Prism 7. Statistical significance was evaluated through unpaired *t test* with Welch's correction where explicitly stated (significant value with $p < 0.05$). All plotted data show mean values with standard deviations calculated from at least 3 independent experiments (samples in duplicates or triplicates).

5.6 Relaxation measurement and data analysis

NV spin relaxation measurements were performed in collaboration of Prof. Wrachtrup's group (3. PhysikalischesInstitut, Stuttgart University). Two electronic grade (Element 6) diamond membranes with 2.5 keV and 4 keV nitrogen implantation (dose ~ 10^{13} N+/cm^2) were prepared in Prof. Wrachtrup's group. After each measurement, the diamond was washed in saturated NaOH solution at 80ºC for overnight, and then washed by strong acid solution for reuse. The diamond membranes were all glued with PDMS on 70 μm thick coverslip (with the NV proximal side facing the air) before further surface functionalization. The 1st relaxation measurement was performed on NV diamond immobilized with PEG chain and chelator DOTA as a linear shape, LC-2 (DOTA), as described in 5.1.1.3.1. Gd^{3+} ions were loaded by incubating the diamond membrane in 2 mg/ml $GdCl_3$*$6H_2O$ water solution for 8 hours. Then relaxation measurements were performed in sequence of in ambient condition, in water, in isopropanol, and again in ambient condition. Three relaxation measurements were performed on Y-shape force sensor constructed by different strategies on diamond membranes, as described in 5.1.1.3. The Y-shape force sensor constructed diamond membranes were loaded by Gd^{3+} ions, washed by 0.1 mM EDTA water solution for about 1 hour to remove the trapped Gd^{3+} ions in PEG chains. Then they were sterilized by 70% ethanol, washed with PBS for 3 times and loaded with MC3T3 cells in a density of 4000/cm^2. After incubation for 4 hours, they were performed with relaxation measurements.

Specially, the relaxation measurements were carried out in Prof. Wrachtrup's lab using a wide-field quantum diamond microscopy as shown in ***figure 5.6.1***. The 532 nm laser (Verdi 5W, Coherent) with 2 W power was focused on the acousto-optical-modulator (AOM, Crystal Technology). The laser light can be switched in ~ns scale

with an extinction ratio of 48 dB. When the laser was focused onto the back-focal plane of the oil objective (100X, NA=1.49, Olympus), the wide-field illumination could be achieved. The fluorescence from excited NVs was spectrally filtered (LP650, Omega) and finally detected by 512 × 512 EM-CCD camera (CascadeII, RoperScientific) cooled at -80 ºC. Finally an effective pixel size of ~115 nm was yielded.

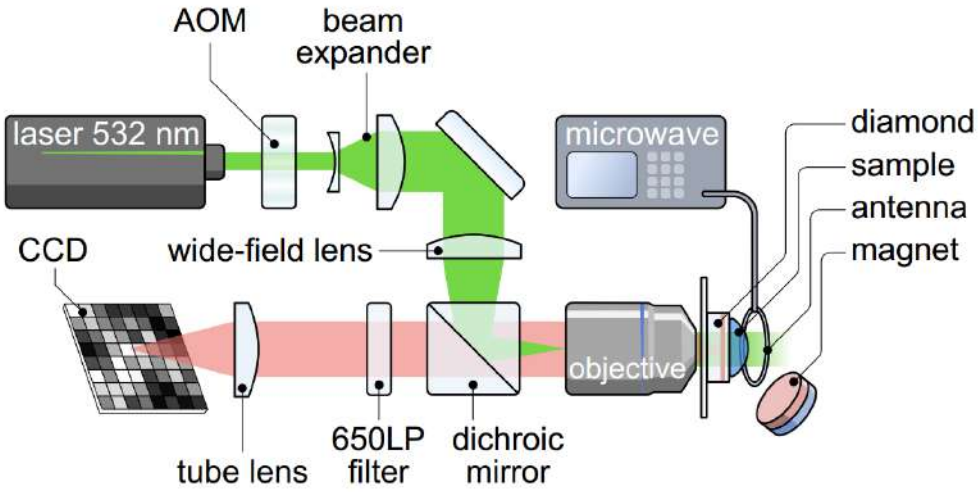

Figure 5.6.1 Wide-field quantum diamond microscopy.

6 Results and Discussion

6.1 Part I: Nitrogen-Vacancy (NV) diamond based force sensor for cell adhesion study

Nitrogen-vacancy (NV) centers are spin defects existing in diamond lattice. Because of their spin-dependent photoluminescence, NV centers can work as prospective quantum sensor, which provides imaging with atomic resolution.[121] The NV center consists of a substitutional nitrogen atom and an adjacent lattice vacancy and is oriented along the direction in the diamond lattice. The negative charged NV centers (NV^-) has been widely applied in sensing and quantum technologies due to its optical and electronic properties. The electronic structure of NV^- center possesses a sharp optical zero-phonon line for fluorescence and broad vibronic side bands. In particular, the NV centers has long coherence time in the range of ms at ambient conditions. In addition, the NV centers is photostable when subjected to intensive illumination. The NV centers can either exist in nanodiamond or bulk diamond modalities.

The NV spin relaxation time (e.g., T1) is sensitive to surrounding magnetic noise, thus such noise occurring at the spin transition frequency can be quantified through NV relaxometry. For instance, when paramagnetic Gd^{3+} ions are closed to NV^- center in diamond, the T1 relaxation time rapidly decays. This is because the gigahertz fluctuations of the Gd^{3+} ions (S=7/2) as strong magnetic noise has an dominant effect on NV center.[121]

Nanodiamond (ND) with NV centers, considered as stable fluorescence biomarkers, has been widely used in biosensing applications. It has additional unique advantage from its nano properties. However, ND requires surface functionalization to achieve

better colloidal stability and covalently attachment of varieties of biomolecules as well, after being fabricated with NV centers.[122] NDs obtained by high-pressure high-temperature method normally need to be treated by strong acid, rendering carboxyl groups rich surface. Then the carboxyl groups can be converted into different functional groups as required. For example, by specific reactions, the carboxyl groups can be converted into acid chloride groups, hydroxyl groups, or amino groups. The surface properties of NDs can also be modified by biopolymer coatings or silica coatings. Surface functionalization of NDs provides the way to conjugate antibodies,[124] DNA,[124] enzymes,[125] and some other functional proteins,[126] which renders the possibilities of diamond sensing in living biological systems. NDs have been used as magnetic resonance imaging (MRI) reagents and drug delivery systems.[127-135] When cell ligands are immobilized on NDs surfaces, the NDs can be targeted to living cells for cell adhesion study.

In this chapter, Y-shape force sensor was constructed on Nitrogen-Vacancy (NV) diamond surface for cell adhesion force study. Three essentials are required: (1) adhesive peptides which induce specific cell adhesion on the surface; (2) metal ions which result relaxation time (T1) change by spin-spin coupling with NVs in diamond; (3) elastic spring which connect the metal ion and NVs. When NV diamond surface constructed by this Y-shape force sensor is loaded by cells, adhesive peptides induce strong cell adhesion, through which traction force subsequently exerts along the elastic spring. The deformation of elastic spring under force render a distance change between metal ion and NVs. This results in a change of relaxation time (T1), which can be detected by a wide-field setup. In this project, arginylglycylaspartic acid (RGD) peptide was chosen as an adhesive peptide motif to analyze the force of integrin-based adhesion. RGD is the most common peptide motif to mimic extracellular matrix

(ECM) for cell adhesion.[136] By functionalizing the surface with RGD peptide, cell adhesion proteins integrins specifically recognize and bind to this sequence, resulting in a strong cell adhesion on the surface. For generating effective T1 signal, gadolinium was chosen. Gadolinium is a chemical element with symbol Gd and atomic number 64. Its electron configuration is $[Xe]4f^7\ 5d^1\ 6s^2$. In the great majority of its compounds, gadolinium adopts the oxidation state +3. Gd^{3+} ion, as paramagnetic ions, has 7 unpaired electrons in outer shell, rendering itself a high spin species. Therefore it is expected to exhibit strong interactions with NVs in diamond resulting in significant changes of relaxation time T1. Gd^{3+}, like most lanthanide ions, forms complexes with high coordination numbers. Chelating agent DOTA, an octadentate ligand was chosen as a proper carrier of Gd^{3+} in this Y-shape force sensor system.[137] Furthermore, the relaxation time T1 is sensitive to the distance between Gd^{3+} and NVs. Therefore polyethylene glycol (PEG) with different molecular weight was used in this project as an elastic spring to connect Gd^{3+} and NVs. PEG is very commonly used as biocompatible material getting in contact with cells. It is chemically stable and biocompatible at the environment of cell experiments.[138] At the same time, PEG chain is relative elastic and easy to be modeled. Therefore, in this project, RGD peptide, Gd-DOTA, and PEG macromolecule were designed to react together through functional groups, and be immobilized onto NV diamond surface by different strategies, in order to achieve optimized Y-shape force sensor. A scheme illustrating the final structure of Y-shape force sensor is shown **in *figure 6.1.1*.**

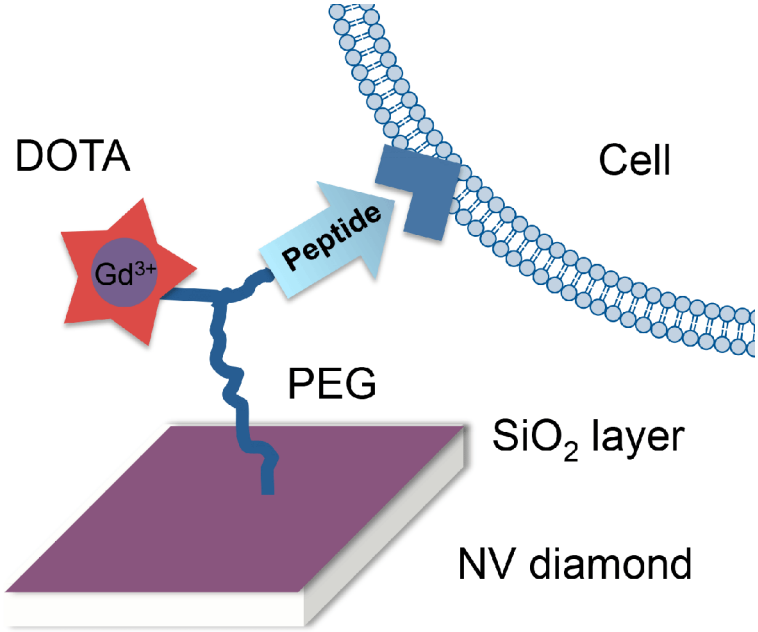

Figure 6.1.1 Y-shape NV diamond based force sensor. NV diamond was first coated with a thin silica layer, and then immobilized with functional PEG chains. RGD peptide was immobilized together with metal ion Gd^{3+} onto NV diamond surface through functional PEG chain.

6.1.1 Cell-mimetic microbeads on NV diamond

In order to simulate Gd^{3+}-NV distance change during cell adhesion on diamond surface, microbeads containing Gd^{3+} ions were immobilzied on NV diamond surface. By binding microbeads on the surface through PEG chains, the distance change resulted T1 change can be modulated by controlling the liquid flowing speed in a flow chamber, where the NV diamond was set. The immobilizing of microbeads was first tested on glass slides coated with PEG molecules prior to NV diamond.

Figure 6.1.2 shows the binding results of 6 μm microbeads onto PEG surfaces through different functional groups. Both beads A and beads B have active amine groups on the surfaces. Beads B were further modified by BSA, which also contains

amine groups. In groups 1 and 2, beads A/B were reacted with BCN-NHS firstly, and then bound onto PEG-N_3 surface and PEG-OMe surface (for comparison) respectively. There were slightly more beads bound onto PEG-N_3 surface in group 1, due to the strain-promoted alkyne-azide cycloadditions (SPAAC) click reaction.[139] There was almost no difference between beads A and beads B binding amount. In groups 3 and 4, beads A/B with amine groups were bound to PEG-NHS surface and PEG-N_3 surface (for comparison) respectively. However, in these two groups, there were very little microbeads bound on surfaces. As the results, reacting BCN-NHS modified beads A/B onto PEG-N_3 surface can be selected as the proper way of immobilizing the microbeads onto NV diamond surface.

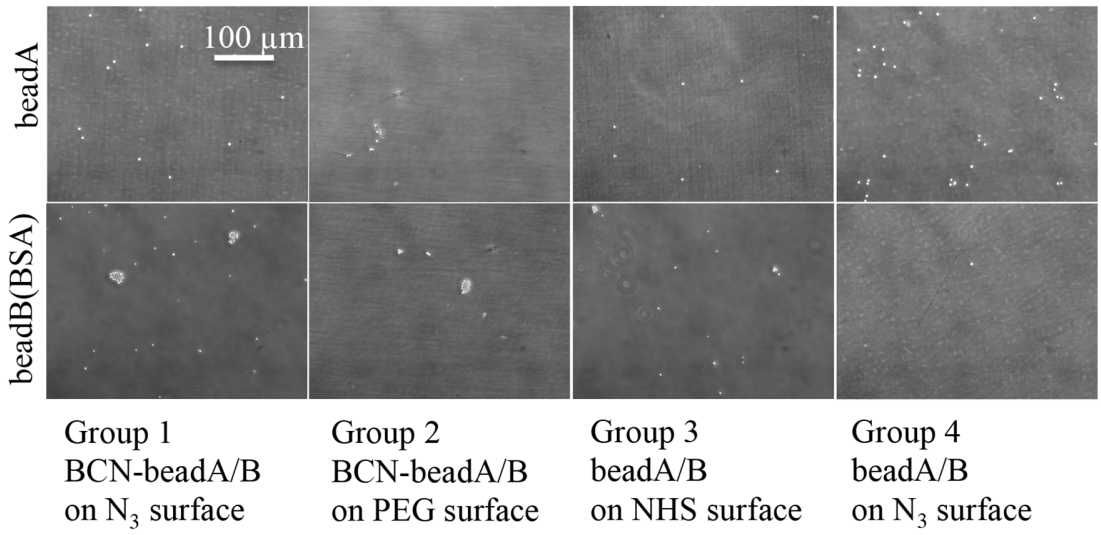

Figure 6.1.2 Representative images of microbeads immobilized on PEG surfaces. There were slightly more BCN-NHS functional beads A/B bound onto PEG-N_3 surface in group 1, compared with other groups. There was no significant difference between beads A and beads B binding.

6.1.2 Preparation of Y-shape force sensor on NV diamond

6.1.2.1 Silica coating

In order to process cell adhesion study on nitrogen-vacancy (NV) diamond, diamond surface needs to be functionalized by a Y-shape force sensor containing three elements: RGD peptide, gadolinium chelator DOTA together with Gd^{3+}, and polymer PEG which functions as an elastic spring when cell force exerts.

NV diamond surface is treated by strong acid, generating carboxyl/hydroxyl groups and other oxidized groups on the surface. However, the amount of active groups on diamond surface is still far from enough to generate a functionalized monolayer. Thus further functionalization is required to construct Y-shape force sensor. In this work, a crosslinked thin silica (SiO_2) layer was constructed firstly on acid-treated diamond surface. Further stable functionalization was then achieved through silane coupling agents. The SiO_2 layer should fulfill two requirements: on one hand they should be stable enough for further functionalization; on the other hand, the SiO_2 layer should be as thin as possible to achieve strong signal between Gd^{3+} and NVs for latter relaxation T1 tests. Thin homogeneous SiO_2 layers were prepared by two methods: method *a* and method *b* shown below.

First, thin SiO_2 layers were obtained by Stöber method as method *a*,[140] constituting of two steps. In the first step, (3-Aminopropyl)triethoxysilane (APTES) was adsorbed onto the negative charged surface through amine groups. In the second step, tetraethyl orthosilicate (TEOS) was added for hydrolysis and condensation in the present of 25% ammonia solution as catalyst. The molecular structures are shown in ***figure 6.1.3.*** By adjusting the coating parameters, e.g. concentration of APTES and TEOS, and the coating time of the 2nd step, SiO_2 layers of different thickness were achieved as shown

in ***table 6.1.1***. At high concentration of APTES and TEOS (4 times more than the condition of low concentration), SiO_2 layer with thickness ~30 nm was achieved by coating TEOS for 1 hour, which was measured by ellipsometry. However, this is too thick for effective sensing of Gd^{3+} with NVs. At low concentration, the thickness of SiO_2 layers was controlled by coating time of TEOS in the 2nd step. SiO_2 layer of ~1.5 nm was achieved by coating TEOS for 1 hour, SiO_2 layers with thickness ~5 nm and ~10 nm were achieved by coating TEOS for 2 and 3 hours, respectively. Since cell adhesion studies are performed in aqueous condition, SiO_2 coating has to be stable in aqueous environment. However, SiO_2 coatings achieved by this method *a* were not stable enough in PBS as shown in ***table 6.1.2***. After being immersed in PBS for 3 days, SiO_2 coatings with different thickness did not exist any more.

APTES

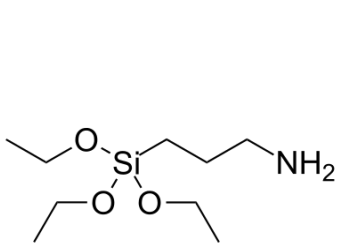

TEOS

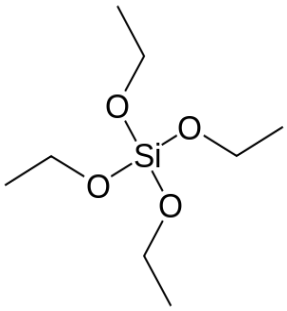

Figure 6.1.3 Molecular structures of (3-Aminopropyl)triethoxysilane (APTES) and tetraethyl orthosilicate (TEOS)

Table 6.1.1 Silica layer thickness obtained by method a

	High concentration	**Low concentration**		
Duration of 2nd step	1 h	1 h	2 h	3 h
Ellipsometry (nm)	30.56	1.43	5.39	9.74

Table 6.1.2 Thickness of SiO_2 layer by method a before and after immersing in PBS

Coating time	Thickness right after coating (nm)	Thickness after in PBS 3 d (nm)
1 h	1.09	0.27
2 h	5.07	0.02
3 h	12.15	0.05

Method *b* is an improved method based on method *a*. 1,2-bis(triethoxysilyl)ethane (BTSE) was used additionally in the 2nd step for more efficient intralayer crosslinking, in order to achieve stable SiO_2 layer. The molecular structure is shown in ***figure 6.1.4***. The thickness of SiO_2 layer was also controlled by coating time of TEOS and BTSE in 2nd step as shown in ***table 6.1.3***. These SiO_2 coatings were stable after being immersed in PBS for three days, but the thickness slightly decreased after being immersed for 2 or 4 weeks. The thinner SiO_2 coating exhibited better stability in PBS. Therefore, the thickness of ~2 nm was considered as a proper thickness for further functionalization. On one hand, it is stable enough; on the other hand, it is thin and homogeneous according to ellipsometry results.

Since the NV diamond is not easy to be fabricated, the reuse should be considered. A proper cleaning method is required to remove SiO_2 coating, and at the same time, it should be safe for NVs in diamond. By immersing in saturated NaOH solution at 80°C for 12 hours, SiO_2 coatings of different thickness were washed away completely, as shown in ***table 6.1.4***.

BTSE

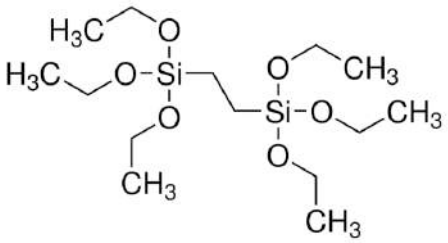

Figure 6.1.4 Molecular structure of 1,2-Bis(triethoxysilyl)ethane (BTSE)

Table 6.1.3 Thickness of SiO_2 layer by method b and after immersing in PBS

Coating time	Thickness right after coating (nm)	Thickness after in PBS 3 d (nm)	Thickness after in PBS 2 weeks (nm)	Thickness after in PBS 4 weeks (nm)
1 h	1.01	1.07	0.96	0.96
1.5 h	2.00	1.95	2.10	1.83
2 h	2.74	2.40	2.08	1.70
3 h	4.02	3.20	2.95	2.55

Table 6.1.4 Silica layer thickness after NaOH treatment

Original SiO_2 thickness (nm)	SiO_2 thickness after treated in NaOH 6 h	SiO_2 thickness after treated in N_aOH 12 h	SiO_2 thickness after treated in N_aOH 24 h
30.56	1.13	0	-
1.43	-	-	0

6.1.2.2 Multi-step synthesis of Y-shape force sensor

Three different functional silane-PEG macromolecules were synthesized in this part, in order to achieve different constructions on SiO_2 coated diamond surface for different cell adhesion study.

First, a linear functional PEG molecule $(EtO)_3Si$-PEG-DOTA without RGD peptide was synthesized by method *a* constituting of three steps as shown in ***figure 6.1.5***. Boc-NH-PEG-NH_2 with molecular weight 3000 Dalton was chosen to react with BCN-DOTA-GA as the 1st step. Statistically, one of the four carboxyl groups from the chelator was activated by EDC, subsequently attacked by amine group from the polymer to form amide bond. LS (A)-1 Boc-NH-PEG-DOTA was obtained, the ^{1}HNMR result is shown in ***figure 6.1.6***. The peaks of BCN-DOTA-GA were detected by NMR and the grafting ratio was ~50%. In the 2nd step, Boc-protected amine groups were reversed into amine groups with the help of hydrochloride solution. LS (A)-2 NH_2-PEG-DOTA was obtained, and the ^{1}HNMR result is shown in ***figure 6.1.7.*** The Boc peak could not be detected in NMR, indicating successful deprotection of Boc groups. The Boc groups were almost completely removed. In the 3rd step, the terminal amine group from NH_2-PEG-DOTA reacted with isocyanate group from $(EtO)_3$-Si-NCO in the present of TEA as a catalyst. LS (A)-3 $(EtO)_3Si$-PEG-DOTA was obtained, the ^{1}HNMR result is shown in ***figure 6.1.8***. The peaks of ethyl groups in silane were detected by NMR and the grafting ratio was ~82%.

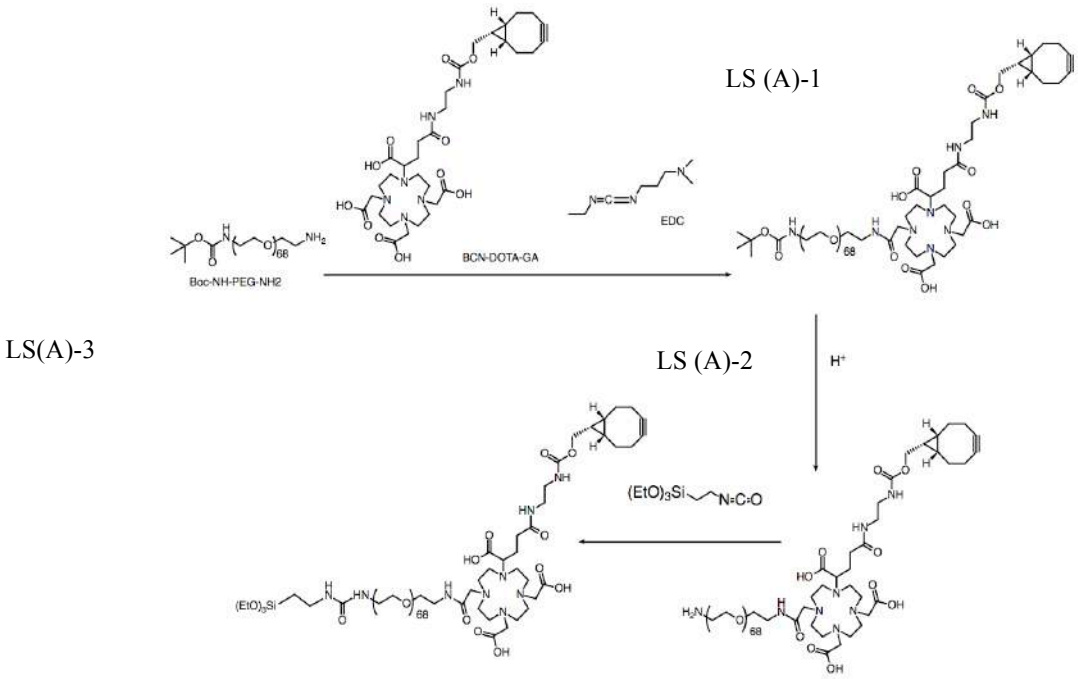

Figure 6.1.5 Linear functional PEG molecule (without RGD peptide) synthesis by method a

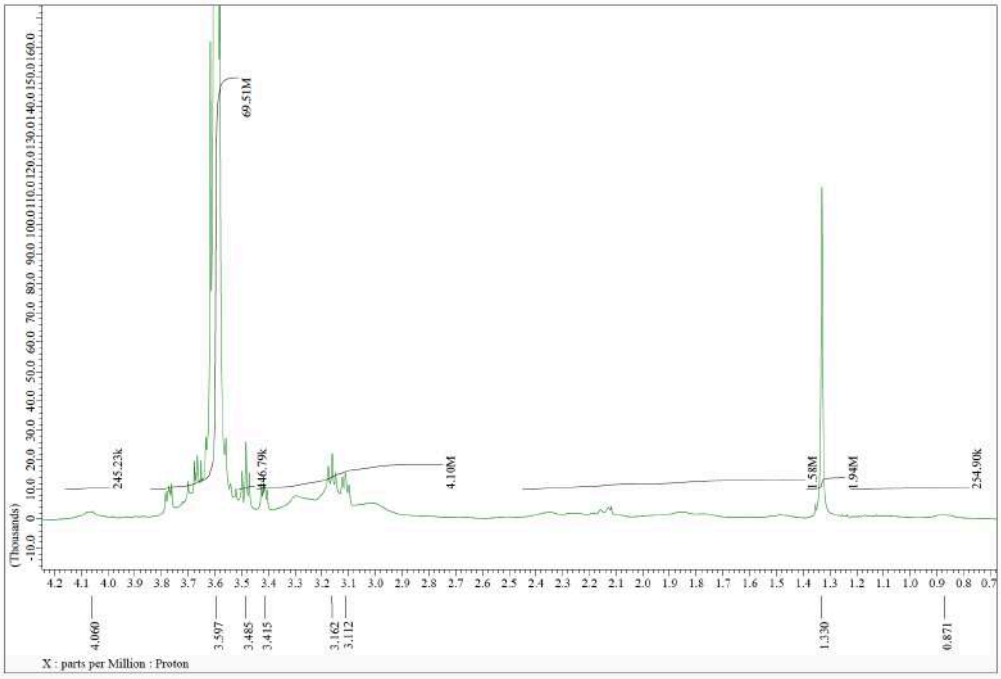

Figure 6.1.6 ^{1}HNMR result of LS (A)-1 Boc-NH-PEG-DOTA. Boc-NH-PEG-DOTA (Yield: 87%) ^{1}H NMR (300 MHz; D_2O): δ = 4.15-4.00 (OCOCH2CH, of BCN); 3.82-3.46 (PEG backbone); 3.46-2.75 (CH2CCCH2 of BCN, and CHCH2CH2CONH of DOTA, and (CH2CH2)4 of DOTA ring); 2.45-1.45 (CH2CHCHCH2 of BCN ring, and OCONHCH2CH2NHOCO of BCN-DOTA-GA); 1.33 ((CH3)3, of Boc); 0.94-0.80 (CHCHCH, of BCN) ppm.

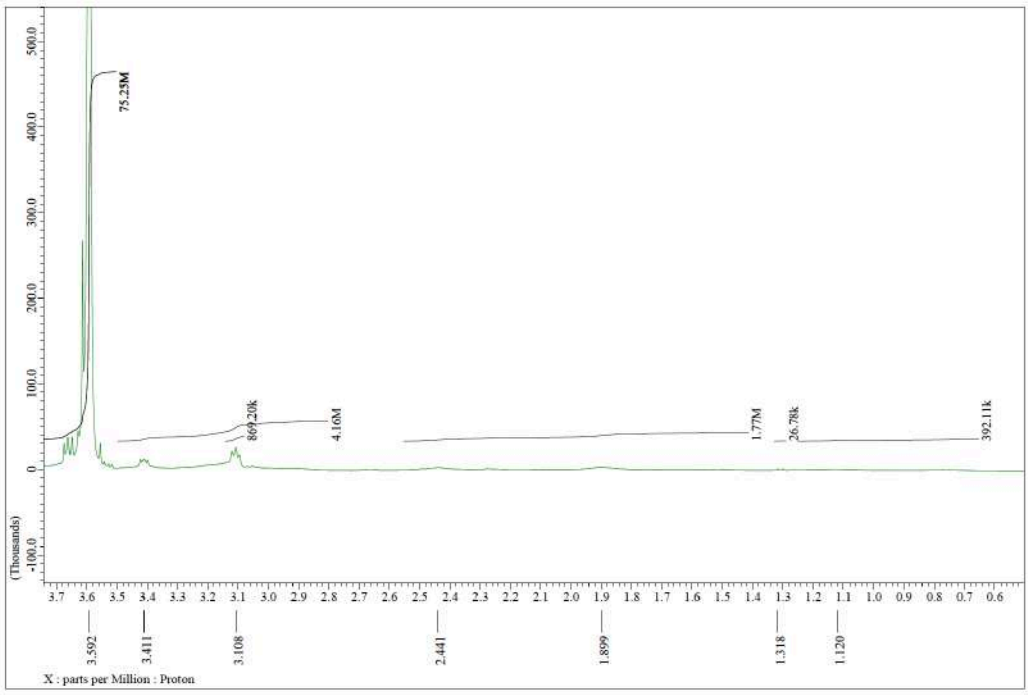

Figure 6.1.7 ^{1}HNMR result of LS (A)-2 NH_2-PEG-DOTA. NH_2-PEG-DOTA (Yield: 80%) ^{1}H NMR (300 MHz; D_2O): δ = 3.70-3.48 (PEG backbone); 3.45-2.75 (CH2CCCH2 of BCN, and CHCH2CH2CONH of DOTA, and (CH2CH2)4 of DOTA ring); 2.55-1.40 (CH2CHCHCH2 of BCN ring, and OCONHCH2CH2NHOCO of BCN-DOTA-GA); 1.15-0.60 (CHCHCH, of BCN) ppm.

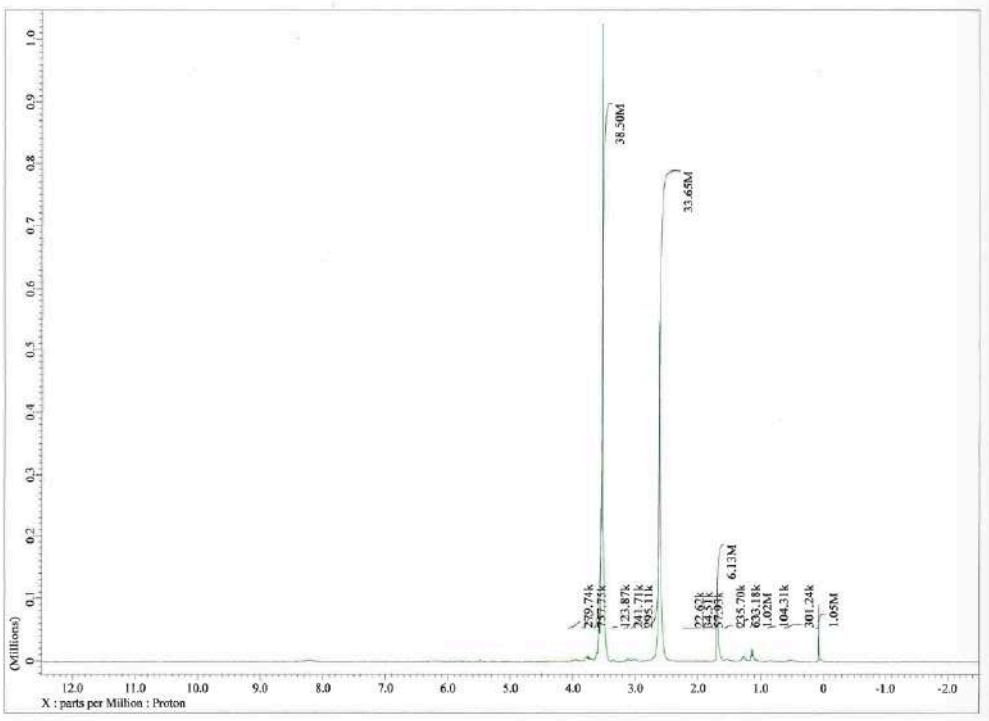

Figure 6.1.8 ^{1}HNMR result of LS (A)-3 $(EtO)_3$Si-PEG-DOTA. $(EtO)_3$Si-PEG-DOTA (Yield: 85%) ^{1}H NMR (300 MHz; THF-D8): δ =4.00-3.45 (PEG backbone and (CH3CH2O)3Si); 3.40-2.90 (CH2CCCH2 of BCN, and CHCH2CH2CONH of GA, and (CH2CH2)4 of DOTA ring); 2.00-0.30 (CH2CHCHCH2 of BCN ring, and OCONHCH2CH2NHOCO of BCN-DOTA-GA, and CHCHCH of BCN); 0.05 (Si(OCH2CH3)3, of (EtO)3Si) ppm.

Another method of one-step method *b* was also developed for synthesizing $(MeO)_3$Si-PEG-DOTA as shown in ***figure 6.1.9***. $(MeO)_3$Si-PEG-N_3 with MW 3000 Dalton directly reacted with BCN-DOTA-GA by high effective click chemistry SPAAC. LS (B) $(MeO)_3$Si-PEG-DOTA was obtained, and the ^{1}HNMR result is

shown in ***figure 6.1.10***. The peaks of BCN-DOTA-GA were detected by NMR and the grafting ratio was >95%. Compared with method *a*, this method *b* is a much more effective and simple way to synthesis linear functional PEG molecule without RGD peptide, silane-PEG-DOTA.

LS (B)

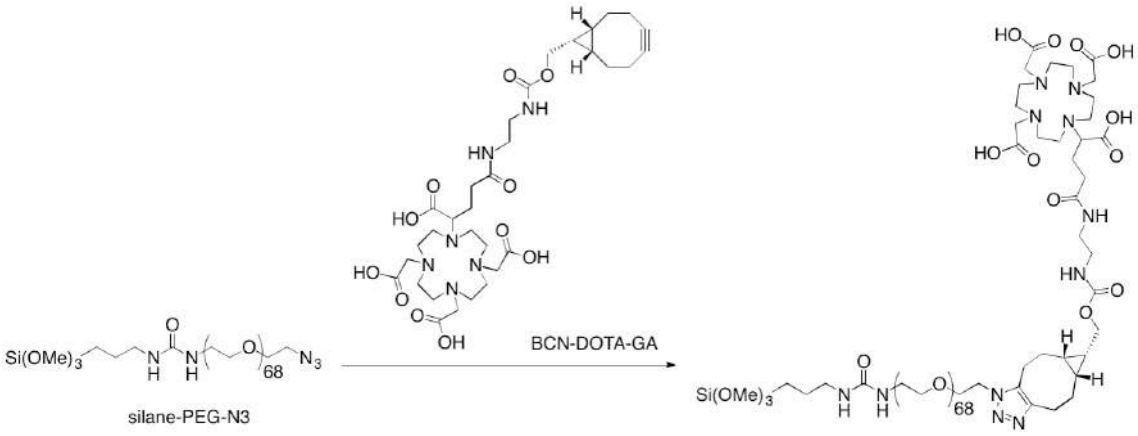

Figure 6.1.9 Linear functional PEG molecule (without RGD peptide) synthesis by method b

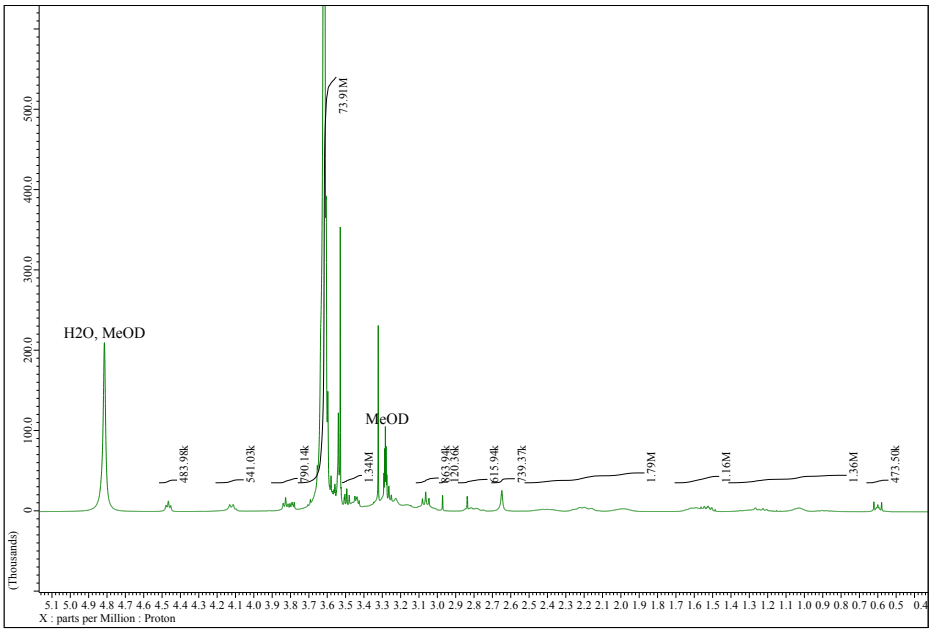

Figure 6.1.10 ^{1}HNMR result of LS (B)-3 $(MeO)_3$Si-PEG-DOTA. $(MeO)_3$Si-PEG-DOTA (Yield: 82%) ^{1}H NMR (300 MHz; MeOD): δ =4.20-4.09 (CHCH2OCO, of BCN); 3.88-3.74 (OCH2CH2N3, of PEG); 3.74-3.57 (PEG backbone backbone and (CH3O)3Si); 3.54-3.40 ((CH2COOH)3, of DOTA); 3.00-1.15 (CH2CCCH2 of BCN, and CHCH2CH2CONH of DOTA, and (CH2CH2)4 of DOTA ring, and CH2CHCHCH2 of BCN ring, and OCONHCH2CH2NHOCO of BCN-DOTA-GA, and (MeO)3SiCH2CH2CH2, of PEG); 1.10-1.00 (CHCHCH of BCN); 0.65-0.50 ((MeO)3SiCH2CH2, of PEG) ppm.

RGD and DOTA functionalized Y-shape PEG molecule was synthesized by two steps as shown in ***figure 6.1.11***. $(MeO)_3$Si-PEG-N_3 with MW 3000 Dalton first reacted with BCN-NHS by SPAAC, subsequently the NHS group reacted with amine group on cysteine from cyclic(RGDfK)C in the presence of TEA. These two reactions were performed in one-pot. YS-(1+2) $(MeO)_3$Si-PEG-RGD was obtained. The ^{1}HNMR result is shown in ***figure 6.1.12***. The peaks of RGD were detected by NMR and the grafting ratio was >95%. Then maleimide group from maleimide-DOTA-GA reacted with thiol group on cysteine from $(MeO)_3$Si-PEG-RGD in the presence of TEA. YS-3 $(MeO)_3$Si-PEG-(RGD+DOTA) was then obtained. The ^{1}HNMR result is shown in ***figure 6.1.13***. The peaks of DOTA were detected by NMR and the grafting ratio was ~40%.

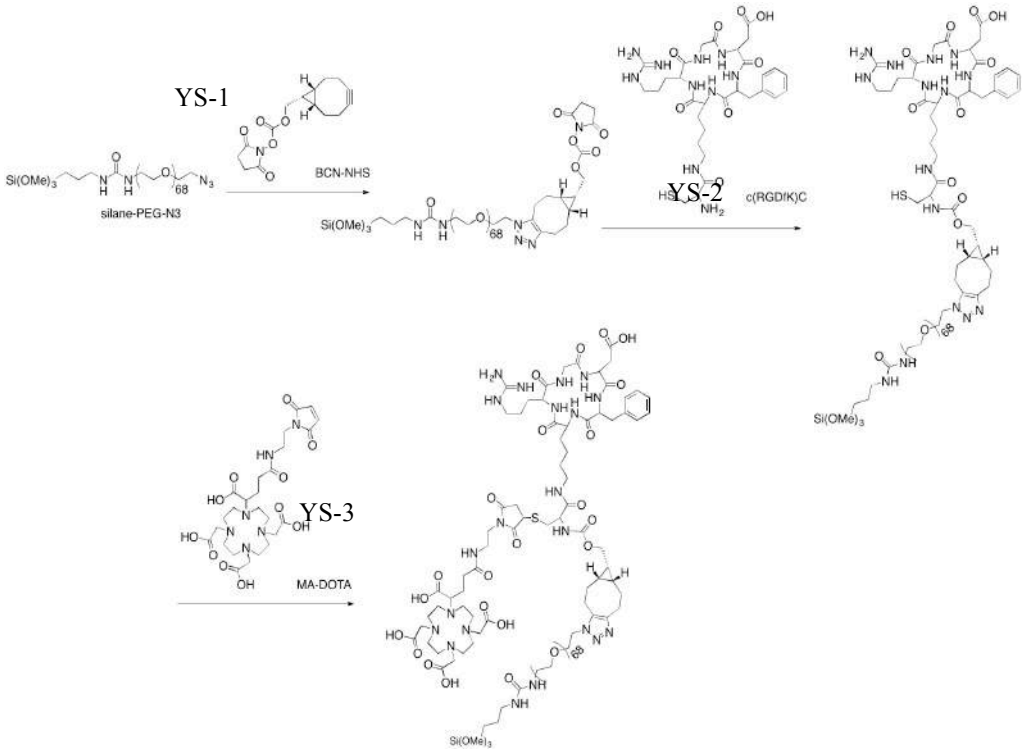

Figure 6.1.11 Y-shape functional PEG molecule synthesis

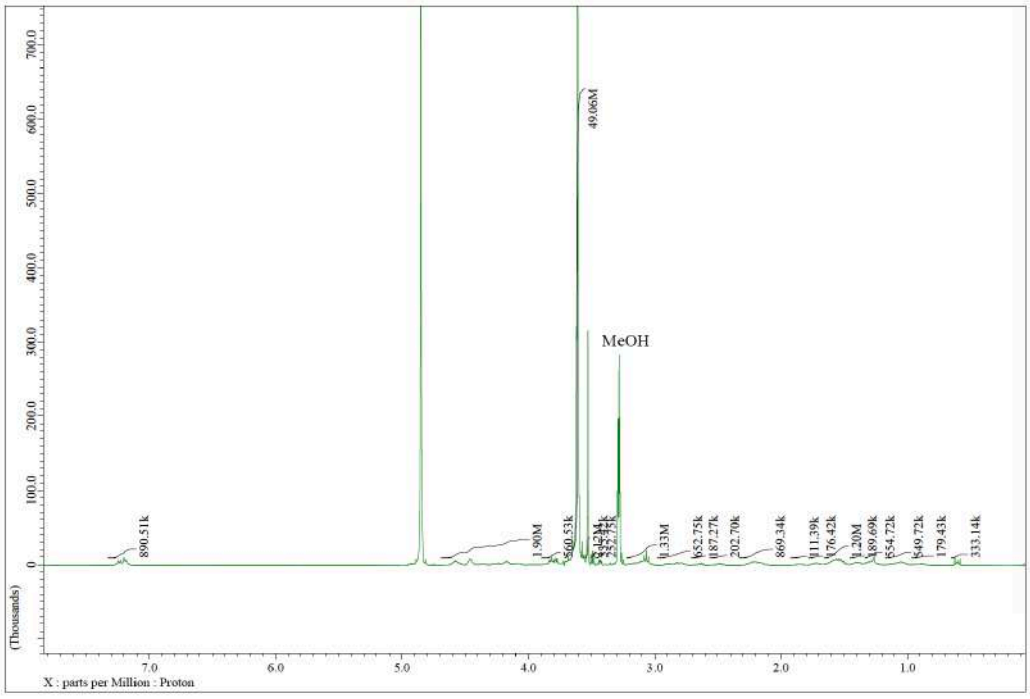

Figure 6.1.12 ^{1}HNMR result of YS-(1+2) $(MeO)_3Si$-PEG-RGD. $(MeO)_3Si$-PEG-RGD (Yield: 70%) ^{1}H NMR (300 MHz; MeOD): δ =7.30-7.10 (C6H5, of phenylalanine in RGD); 4.70-4.00 (CHCH2OCO of BCN, and HNCH(CH2SH)CONH of cysteine in RGD, and RGD backbone); 3.90-3.75 (OCH2CH2N3, of PEG); 3.70-3.55 (PEG backbone and (CH3O)3Si); 3.10-3.00 (CHCH2C6H5, of phenylalanine in RGD); 3.00-2.00 (CH2CCCH2 of BCN, and CHCH2COOH of aspartate in RGD, and CHCH2SH of cysteine in RGD); 2.00-0.80 (CHCHCH of BCN, and CH2CHCHCH2 of BCN ring, and (MeO)3SiCH2CH2CH2 of PEG, CHCH2CH2CH2CH2NHCO of lysine in RGD, and CHCH2CH2CH2NH of arginine in RGD); 0.6 ((MeO)3SiCH2CH2, of PEG) ppm.

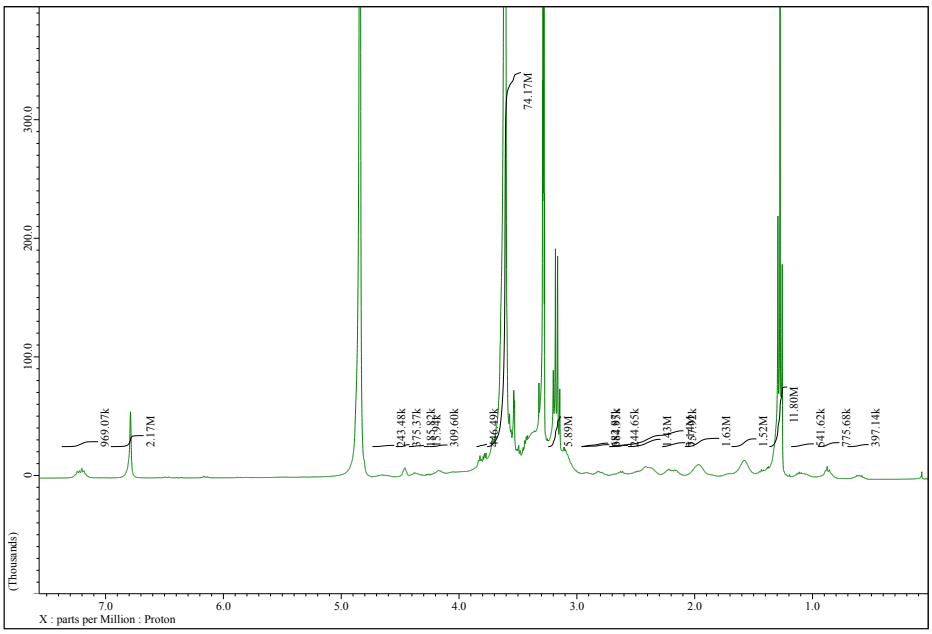

Figure 6.1.13 ^{1}HNMR result of YS-3 $(MeO)_3$Si-PEG-(RGD+DOTA). $(MeO)_3$Si-PEG-(RGD+DOTA) (Yield: 75%) ^{1}H NMR (300 MHz; MeOD): δ =7.30-7.10 (C6H5, of phenylalanine in RGD); 4.70-4.00 (CHCH2OCO of BCN, and HNCH(CH2SH)CONH of cysteine in RGD, and RGD backbone); 3.90-3.55 (OCH2CH2N3 of PEG, and PEG backbone, and (CH3O)3Si); 3.00-2.10 (CH2CCCH2 of BCN, and CHCH2COOH of aspartate in RGD, and CHCH2SH of cysteine in RGD, and (CH2CH2)4 of DOTA, and CHCH2C6H5 of phenylalanine in RGD); 2.10-0.80 (CHCHCH of BCN, and CH2CHCHCH2 of BCN ring, and (MeO)3SiCH2CH2CH2 of PEG, CHCH2CH2CH2CH2NHCO of lysine in RGD, and CHCH2CH2CH2NH of arginine in RGD, and CHCH2CH2CONH of DOTA); 0.6 ((MeO)3SiCH2CH2, of PEG) ppm.

After functional PEG molecules silane-PEG-DOTA and silane-PEG-(RGD+DOTA) were synthesized, they were coated onto glass surfaces and silicon surfaces through silane groups. The characterization results of these functionalized surfaces are listed in ***table 6.1.5***. Polymer coating thickness and water contact angle were tested on silicon wafers, while cell adhesion on polymer coating was tested on glass slides. Bare silicon wafer after piranha treatment was very hydrophilic (8.3°) and polymer thickness was fitted out to be 0 by ellipsometry. After coated by LS (B) $(MeO)_3$Si-PEG-DOTA, a thickness of ~1.2 nm coating was detected and the surface became more hydrophobic (33.6°), which matched the typical water contact angle of a PEG-like coating on SiO_2 surface.[141] YS-3 $(MeO)_3$Si-PEG-(RGD+DOTA) coated surface exhibited similar hydrophilicity and thickness further increased to ~2 nm.

Table 6.1.5 Characterization results of Y-shape and linear functionl PEG coated surfaces

Different surfaces	Thickness tested by Ellipsometry (nm)	Water contact angle (°)	Cell-adhesion experiment (4 h)
Bare slide	0	8.3	Some cells adhered
LS (B) $(MeO)_3Si$-PEG-DOTA	1.24	33.6	Almost no cells adhered
YS-3 $(MeO)_3Si$-PEG-(RGD+DOTA)	2.17	35.3	Some cells adhered

Cell spreading on these two functionalized surfaces was tested by incubating MC3T3 cells on these surfaces for 4 hours, as shown in ***figure 6.1.14***. Compared with bare slide, on which cells non-specifically adhered, there were almost no cells adhered on $(MeO)_3Si$-PEG-DOTA coated surface. Therefore, the successful immobilization of functional PEG LS (B) was once more confirmed and both PEG chains and DOTA groups were proved not to cause cell adhesion. $(MeO)_3Si$-PEG-DOTA coated surface can be used as a negative control in future cell adhesion study on NV diamonds. In the meanwhile, only some cells not all cells spread on $(MeO)_3Si$-PEG-(RGD+DOTA) coated surface. The possibilities can be either RGD peptide lost its activity or silane group lost functionality during multi-step reactions. Silane groups were very sensitive to water. In order to confirm the synthesized products and polymer coatings on surfaces, $(MeO)_3Si$-PEG-DOTA and $(MeO)_3Si$-PEG-(RGD+DOTA) coated silicon wafers were loaded by Gd^{3+} and analyzed by XPS, which is shown in ***table 6.1.6***. Compared with on bare Si slide, the content of element Si dramatically decreased, while the contents of elements O, C, N increased and Gd was detected on two polymer $(MeO)_3Si$-PEG-DOTA and $(MeO)_3Si$-PEG-(RGD+DOTA) coated slides. Furthermore, the content ratio of N/C on both surfaces

matched the N/C atom constitution of the relative polymers. Therefore both LS (B) $(MeO)_3Si$-PEG-DOTA and YS-3 $(MeO)_3Si$-PEG-(RGD+DOTA) were successfully coated onto surfaces as shown by XPS results. However, the density of coatings may be not enough to efficiently cover the whole substrate surfaces based on the cell adhesion tests above.

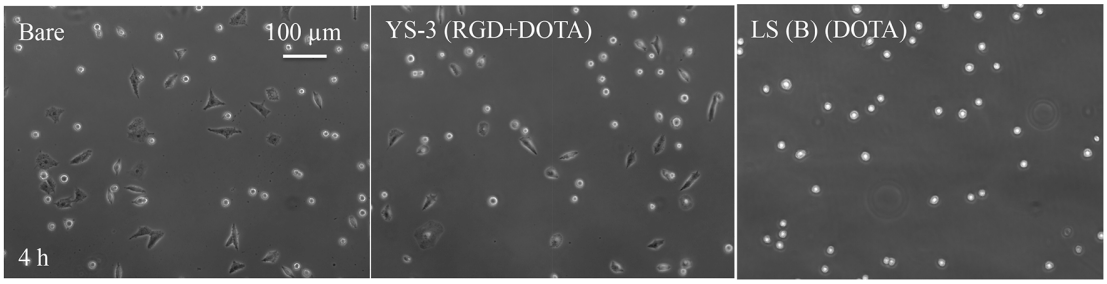

Figure 6.1.14 Representative images of MC3T3 cell adhesion on Y-shape and linear functionl PEG coated surfaces. There were almost no cells adhered on LS (B) (DOTA) coated surface. In the meanwhile only some cells not all cells spread on YS-3 (RGD+DOTA) coated surface. The possibilities can be either RGD peptide lost its activity or silane group lost functionality during multi-step reactions.

Table 6.1.6 Atom constitutes on LS (B) and YS-3 coated surfaces by XPS

Samples		**Elements**				
		Si	O	C	N	Gd
Bare	Area percentage %	54.95	36.06	8.34	0.65	-
LS (B) $(MeO)_3Si$-PEG-$(DOTA+Gd^{3+})$	Area percentage %	52.74	36.82	9.65	0.71	0.08
	Theoretical atom number	-	80	174	11	1
YS-3 $(MeO)_3Si$-PEG-$(RGD+DOTA+Gd^{3+})$	Area percentage %	50.74	39.16	9.36	0.72	0.01
	Theoretical atom number	-	90	207	21	1

6.1.2.3 Bottom-up construction of Y-shape force sensor with long PEG chain (Y-shape L)

The method of multi-step synthesis for Y-shape force sensor has the drawback that silane groups are very sensitive to water and easily lost activity during reactions. Therefore, bottom-up coating methods for constructing Y-shape force sensors on substrate surface were developed. Y-shape L refers to the methods of using long PEG chain of MW 3000 Dalton, in contrast with using short PEG chain (Y-shape S) as shown in next section.

Before the construction of Y-shape L, a linear force sensor constructed on glass slides and silicon wafers was obtained by bottom-up coating procedure as shown in ***figure 6.1.15***. $(MeO)_3Si$-PEG-N_3 with MW 3000 Dalton was coated onto slide surfaces through silane groups as the 1st step to render LC-1 (N_3). In the 2nd step, BCN-DOTA-GA was coated onto the surfaces to render LC-2 (DOTA) through SPAAC between BCN and azide groups. Afterwards one of the four carboxyl groups on DOTA chelator was statistically activated by EDC and NHS, followed by amide coupling to immobilize cyclic(RGDfK) as the 3rd step. LC-3 (RGD) was therefore obtained. Gd^{3+} were loaded onto chelator DOTA either before or after the immobilization of c(RGDfK) to render LC-4 (RGD+Gd^{3+} before) and LC-5 (RGD+Gd^{3+} after) respectively. Characterization results of linear bottom-up coating surfaces of each step are listed in ***table 6.1.7***. Bare slides that were washed by piranha were very hydrophilic. In addition, the thickness of polymer layer fitted by ellipsometry was 0. After coated by $(MeO)_3Si$-PEG-N_3, the surface became more hydrophobic, and the thickness of polymer layer was fitted to be ~2.6 nm. LC-2

(DOTA) exhibited similar thickness and hydrophilicity as LC-1 (N_3). LC-3 (RGD) became even more hydrophobic while the thickness almost remained the same. The immobilization of both BCN-DOTA-GA and c(RGDfK) did not cause obvious thickness change, since molecular weights of these two molecules are relatively small. Cell-adhesion images on these surfaces for 4 hours are shown in ***figure 6.1.16.*** There were only a few cells adhered on bare surface, and there were almost no cells adhered on LC-1 (N_3) and LC-2 (DOTA) surfaces. Therefore, azide groups and DOTAs on surfaces did not cause non-specific cell adhesion. This corresponded with the results in ***figure 6.1.17*** that LC-1 (N_3) surface prevented the adsorption of FITC labeled fibronectin. The adsorption amount of fibronectin on bare slide was much higher than that on LC-1 (N_3) surface, which was indicated by fluorescence intensity on two surfaces. In contrast with the anti-fouling effect on LC-1 (N_3) and LC-2 (DOTA), cells well spread on LC-3 (RGD), LC-4 (RGD+Gd^{3+} before), and LC-5 (RGD+Gd^{3+} after) surfaces because of RGD-integrin induced cell adhesion. Furthermore, Gd^{3+} was proved to be nontoxic for cells, which was important for cell adhesion studies on NV diamond. LC-5 (RGD+Gd^{3+} after) surface was analyzed by XPS as well, as listed in ***table 6.1.8***. Compared with bare Si slide, the content of Si decreased, while the contents of O, C, N all increased, and Gd was detected on the linear bottom-up coated surface LC-5 (RGD+Gd^{3+} after). The content ratio of N/C matched the N/C atom constitution of the polymer. Therefore the XPS results confirmed the successful construction of LC-5 (RGD+Gd^{3+} after) on surface. Linear bottom-up coating is a straightforward method to produce an RGD and DOTA functionalized force sensor. However, it is possible that the structure of chelator DOTA is deformed under cell force, because it is directly connected to RGD where cell force exerts. This could lead to a release of Gd^{3+} or even rupture of the chain, resulting in a failure of cell adhesion

study on NV diamond. Moreover, the amount of RGD immobilized on the DOTA chelator was only statistically to be one. The molecular structure of the force sensor cannot be well controlled.

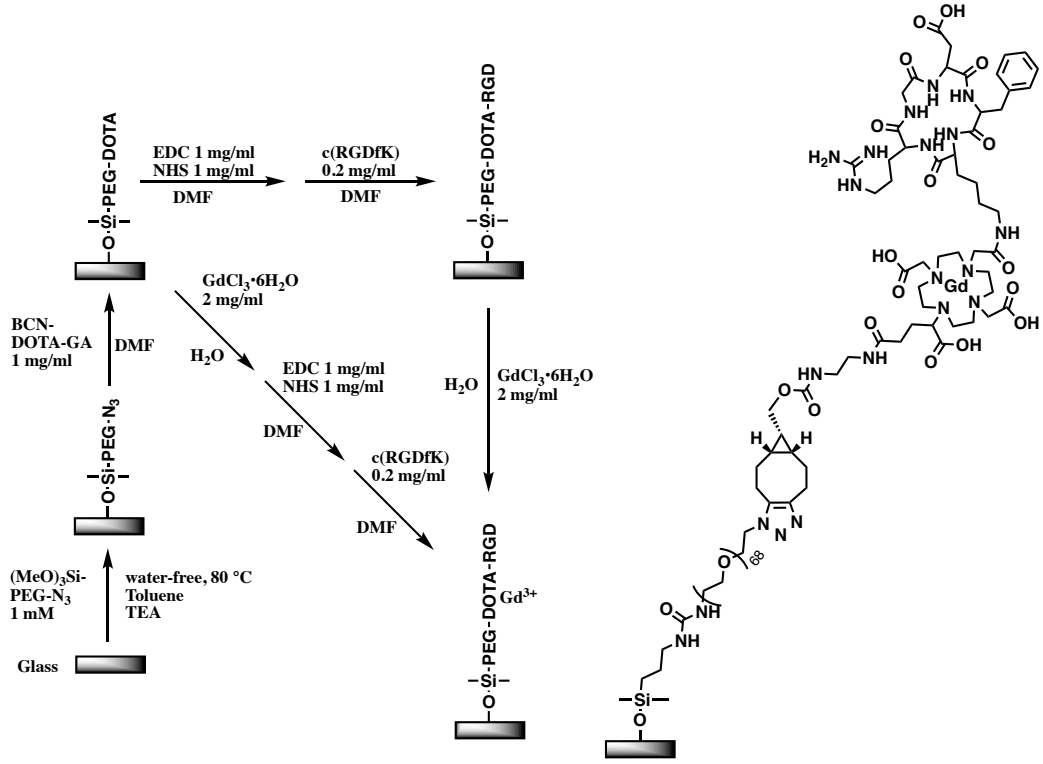

Figure 6.1.15 Linear bottom-up coating procedure. $(MeO)_3Si\text{-}PEG\text{-}N_3$ was first coated onto slide surfaces, and then BCN-DOTA-GA was coated onto the PEG surfaces. Afterwards Gd^{3+} chelator DOTA was activated by EDC and NHS, subesequently attacked by amine group from cyclic(RGDfK). Gd^{3+} ions were loaded onto chelator DOTA either before c(RGDfK) reaction or after c(RGDfK) reaction.

Table 6.1.7 Characterization results of linear bottom-up coating surfaces

Different surfaces	Thickness tested by Ellipsometry (nm)	Water contact angle (°)	Cell-adhesion experiment (4 h)
Bare slide	0	8.3	Some cells adhered
LC-1 (N_3)	2.60	35.84	Almost no cells adhered
LC-2 (DOTA)	2.93	30.9	
LC-3 (RGD)	2.89	38.83	Cells adhered very well
LC-4 (RGD + Gd^{3+} before)	-	-	
LC-5 (RGD + Gd^{3+} after)	-	-	

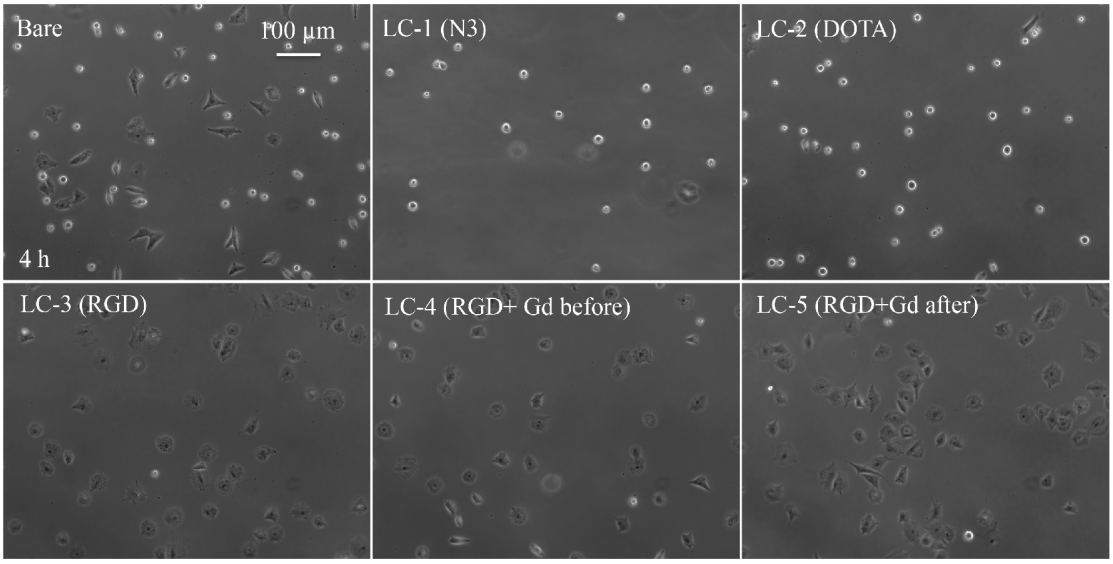

Figure 6.1.16 Representative images of MC3T3 cell adhesion on linear bottom-up coating surfaces. There were almost no cells adhered on LC-1 (N_3) and LC-2 (DOTA) surfaces, while cells spread very well on LC-3 (RGD), LC-4 (RGD+Gd^{3+} before) and LC-5 (RGD+Gd^{3+} after) surfaces because of RGD-integrin induced cell adhesion. Gd^{3+} was proved to be nontoxic for cells.

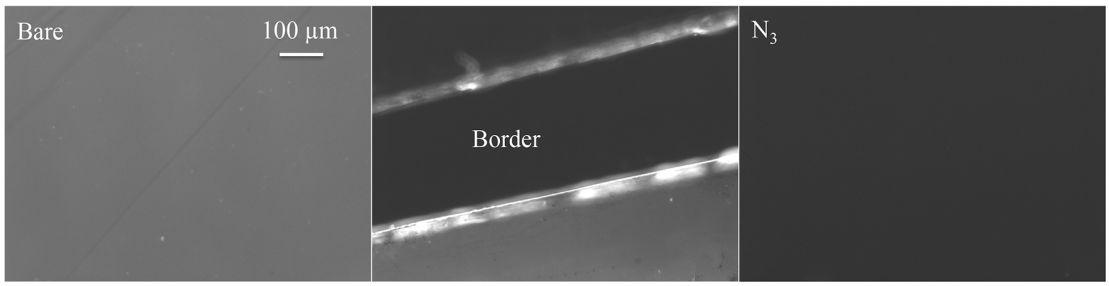

Figure 6.1.17 Representative images of fibronectin adsorption on PEG-azide coated surface. The adsorption amount of fibronectin on bare slide was much higher than that on LC-1 (N_3) surface, indicating the anti-fouling effect on LC-1 (N_3) surface.

Table 6.1.8 Atom constitutes of LC-5 (RGD+Gd^{3+}) surface by XPS

Samples		Elements				
		Si	O	C	N	Gd
Bare	Area percentage %	54.95	36.06	8.34	0.65	-
LC-5 (RGD+Gd^{3+})	Area percentage %	50.60	37.54	10.86	0.98	0.01
	Theoretical atom number	-	86	202	20	1

Bottom-up construction of Y-shape force sensors was achieved by three strategies. The 1st Y-shape strategy is described in ***figure 6.1.18***. The same as in linear bottom-up coating introduced above, $(MeO)_3Si$-PEG-N_3 with MW 3000 Dalton was coated onto clean slide surfaces firstly. YC-1 (N_3) was obtained, which was actually the same as linear bottom-up coating LC-1 (N_3). Then BCN-NHS was coated onto the surfaces to render YC-2 (NHS) through SPAAC between BCN and azide groups. Afterwards, cyclic(RGDfK)C, which contained thiol group and free amine group on the terminal amino acid cysteine was loaded onto YC-2 (NHS). NHS groups on the surface reacted

with amine groups in the presence of TEA as a base, to render YC-3 (RGD). The remained thiol group then reacted with maleimide-DOTA-GA in the presence of TEA and $NaHCO_3$, rendering YC-4 (RGD+DOTA). Gd^{3+} ions were loaded finally. Characterization results of coated surfaces in each step by the 1st Y-shape strategy are listed in ***table 6.1.9***. Bare slides that were washed by piranha were very hydrophilic, and the thickness of coatings fitted by ellipsometry was 0. After being coated by $(MeO)_3Si$-PEG-N_3, YC-1 (N_3) surface became more hydrophobic, and coating thickness was fitted to be ~2.6 nm. Coatings in following steps YC-2 (NHS), YC-3 (RGD), YC-4 (RGD+DOTA), and YC-5 (RGD+DOTA+Gd^{3+}) had similar thickness. The little difference of thickness should be the derivation during ellipsometry tests. Among these surfaces, YC-3 (RGD) exhibited highest hydrophobicity, corresponding with the result from linear bottom up coating. The cell adhesion on the surfaces for 4 hours corresponded with linear bottom-up coatings as well (***figure 6.1.19***). YC-1 (N_3) surface prevented cell adhesion, while some cells adhered on YC-2 (NHS) due to the interaction between NHS group and ECM proteins.[142] In contrast, cells well adhered on YC-3 (RGD), YC-4 (RGD+DOTA), and YC-5 (RGD+DOTA+Gd^{3+}), which indicated the successful immobilization of RGD for cell adhesion. The coating procedure was monitored by QCM-D as well, as shown in ***figure 6.1.20***. SiO_2-based Qsensor was first coated by $(MeO)_3Si$-PEG-N_3 with MW 3000 Dalton. Meanwhile, BCN-c(RGDfK)C was synthesized by reacting BCN-NHS with c(RGDfK)C in the present of TEA for overnight. BCN-c(RGDfK)C was added onto $(MeO)_3Si$-PEG-N_3 coated Qsensor in a static modulus for QCM-D measurements. The frequency shifted after washing by water for 3 times, from which the binding amount of BCN-c(RGDfK)C was calculated to be 245.68 ng/cm^2. However, the subsequent loading of maleimide-DOTA-GA and $GdCl_3*6H_2O$ did not cause any frequency change in

QCM-D. On one hand, the molecular weights of maleimide-DOTA-GA and $GdCl_3*6H_2O$ may be too small to be detected in QCM-D. On the other hand, the grafting ratio of maleimide-DOTA-GA may be too small, due to the large steric effect of the immobilized RGD and the maleimide-DOTA. The maleimide-thiol reaction was therefore limited to a large extent. The immobilization strategies need to be improved.

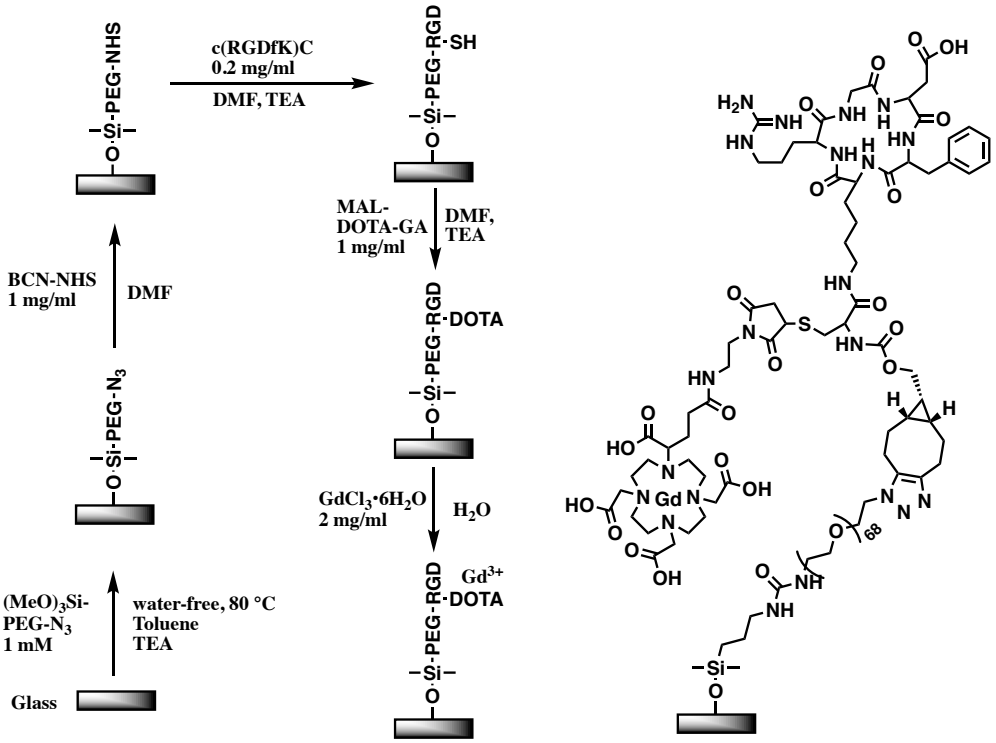

Figure 6.1.18 1st Y-shape bottom-up coating procedure. $(MeO)_3Si\text{-}PEG\text{-}N_3$ was first coated onto slide surfaces. Then BCN-NHS was coated onto the PEG surfaces. cyclic(RGDfK)C was loaded onto NHS group functionalized surface through amine groups. The remained thiol group on cysteine residue then reacted with maleimide-DOTA-GA. Gd^{3+} ions were loaded finally.

Table 6.1.9 Characterization results of bottom-up coating surfaces by 1st Y-shape strategy

	Thickness tested by Ellipsometry (nm)	Water contact angle (°)	Cell-adhesion experiment (4 h)
Bare slide	0	8.3	Some cells adhered
YC-1 (N_3)	2.67	35.64	Almost no cells adhered
YC-2 (NHS)	2.81	-	Few cells adhesion
YC-3 (RGD)	3.03	43.67	Cells adhered very well
YC-4 (RGD + DOTA)	2.49	37.29	Cells adhered very well
YC-5 (RGD+DOTA+Gd^{3+})	1.92	34.69	Cells adhered very well

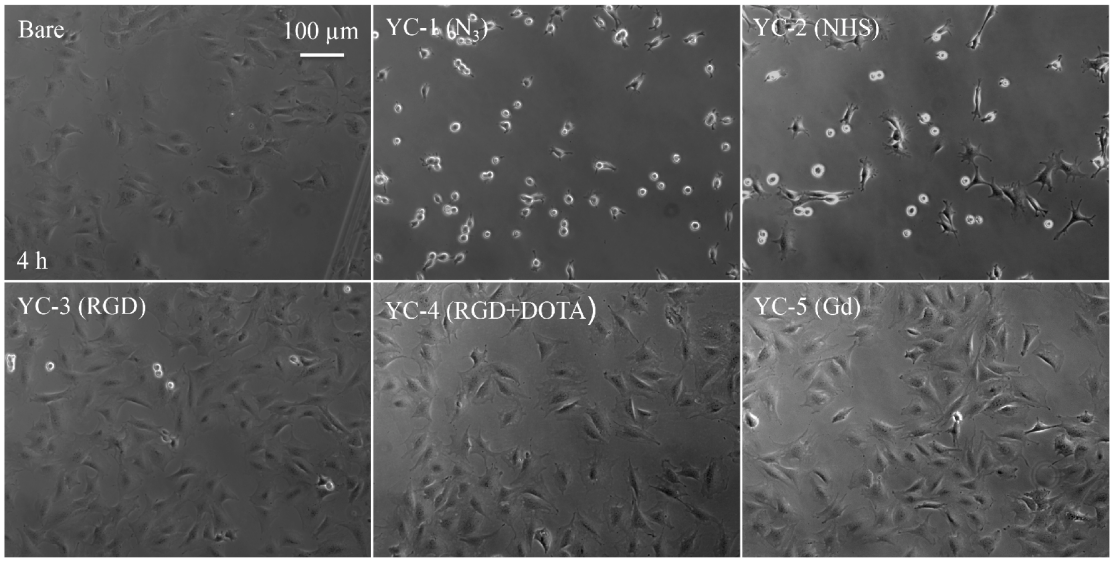

Figure 6.1.19 Representative images of MC3T3 cell adhesion on bottom-up coating surfaces by 1st Y-shape strategy. YC-1 (N_3) surface prevented cell adhesion, while some cells adhered on YC-2 (NHS) due to the interaction between NHS group and ECM proteins. Cells well adhered on YC-3 (RGD), YC-4 (RGD+DOTA), and YC-5 (RGD+DOTA+Gd^{3+}) because of RGD-integrin induced cell adhesion.

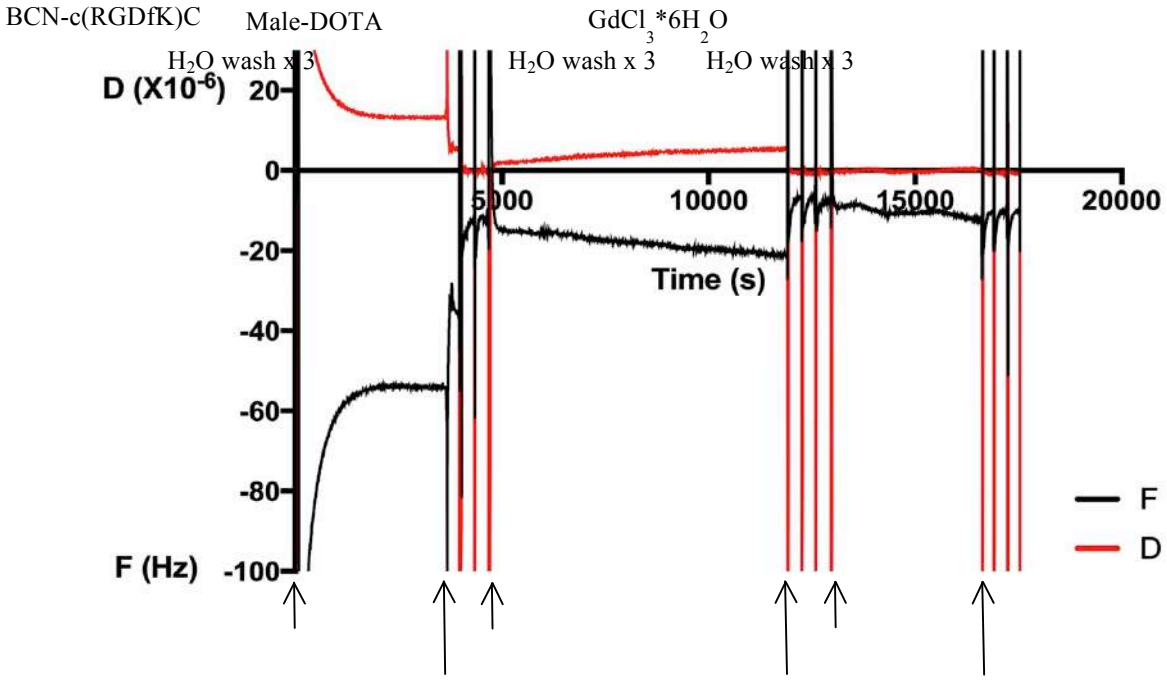

Figure 6.1.20 QCM frequency (F) and dissipation (D) shift as a function of time during adsorption of BCN-c(RGDfK)C, maleimide-DOTA and Gd^{3+} on $(MeO)_3Si$-PEG-N_3 coated Qsensor. The frequency shifted after binding of BCN-c(RGDfK)C, the binding amound was calculated to be 245.68 ng/cm^2. However, the subsequent loading of maleimide-DOTA-GA and $GdCl_3*6H_2O$ did not cause any frequency change in QCM-D.

The procedure of the 2nd Y-shape strategy is described in ***figure 6.1.21***. In order to improve the reaction efficiency between c(RGDfK)C and maleimide-DOTA-GA, they

were first mixed together to react completely via thiol-maleimide michael addition. Afterwards this RGD-DOTA 2-in-1 molecule was immobilized onto NHS functional PEG coated surface YC-2 (NHS) which was obtained by the same procedure in the 1st Y-shape strategy. The synthesis of RGD-DOTA 2-in-1 molecule was monitored by mass spectroscopy. It was confirmed that all RGDs were consumed up during reaction by mixing 1 equivalent of c(RGDfK)C and 1.2 equivalent of maleimide-DOTA-GA, as shown in ***figure 6.1.22***. There was no peak around 707 m/z which represented for c(RGDfK)C. While there was a peak around 600 m/z, indicating the residual maleimide-DOTA-GA molecules. Most important, the peak of RGD-DOTA 2-in-1 molecule was detected at around 650 m/z with 2 positive charges. The maleimide groups of maleimide-DOTA-GA might also react with the amine groups of RGD in certain conditions. However, no RGD was detected to react with two molecules of maleimide. Therefore, no free thiol groups, which can react with BCN, left in the product mixture, but the amine groups must be still active. Since RGD-DOTA was further immobilized onto NHS surface through amine group on RGD and all c(RGDfK)C were converted into RGD-DOTA, no RGD peptide without DOTA-GA could be immobilized on the surface. RGD peptide without maleimide-DOTA-GA on the surface could still induce cell adhesion but not the relaxation signal output. The residual NHS groups after RGD-DOTA immobilization could be easily hydrolyzed to hydroxyl groups. Characterization results of coated surfaces in each step by the 2nd Y-shape strategy are also listed in ***table 6.1.10***. Similar to the 1st Y-shape strategy, surfaces became more hydrophobic after polymer functionalization. Polymer thickness fitted by ellipsometry was ~2 nm. Cell adhesion for 4 hours is shown in ***figure 6.1.23***. YC-3 (RGD+DOTA) and YC-4 (RGD+DOTA+Gd^{3+}) induced obvious cell adhesion, however, not better than on YC-2 (NHS) surface, where cell adhesion

was induced by NHS groups. From these results, we can not conclude that RGD-DOTA was successfully coated onto NHS surface, since all three surfaces YC-2 (NHS), YC-3 (RGD+DOTA), and YC-4 (RGD+DOTA+Gd^{3+}) behaved the same. The steric effect may still be the problem. Thus the 3rd Y-shape strategy was developed based on this.

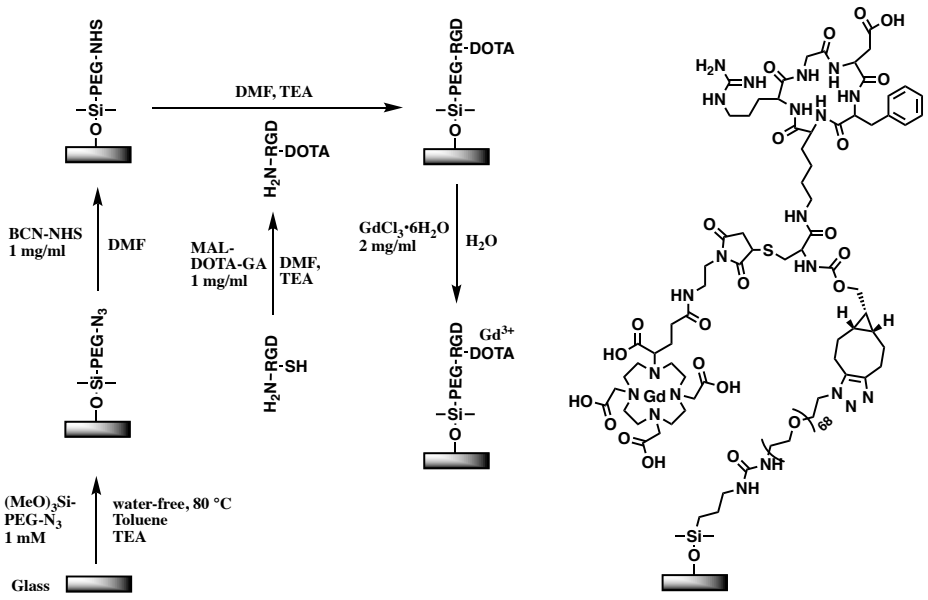

Figure 6.1.21 2nd Y-shape bottom-up coating procedure. c(RGDfK)C and maleimide-DOTA-GA were mixed together to react firstly. Then this RGD-DOTA 2-in-1 molecule was immobilized onto NHS functional PEG surface, which was obtained by the same procedure in the 1st Y-shape strategy.

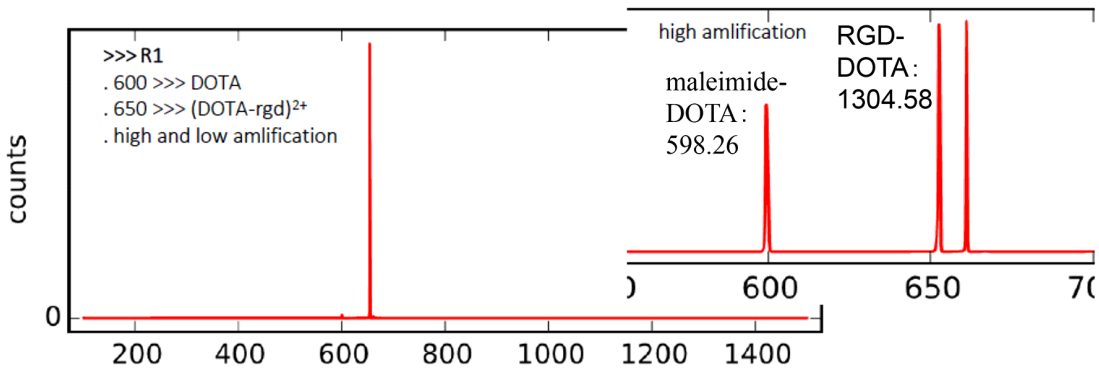

Figure 6.1.22 Mass spectroscopy result of c(RGDfK)C and maleimide-DOTA-GA reaction. There was no peak around 707 m/z which represented for c(RGDfK)C, indicating the complete consumption of c(RGDfK)C. While there was a peak around 600 m/z, indicating the residual maleimide-DOTA-GA molecules. The peak of RGD-DOTA 2-in-1 molecule was detected at around 650 m/z with 2 positive charges.

Table 6.1.9 Characterization results of bottom-up coating surfaces

	Thickness tested by Ellipsometry (nm)	**Water contact angle (°)**	**Cell-adhesion experiment (4 h)**
Bare slide	0	8.3	Cells adhered
YC-1 (N_3)	1.76	35.64	Almost no cells adhered
YC-2 (NHS)	2.18	-	Cells adhered
YC-3 (RGD + DOTA)	1.60	32.3	Cells adhered
YC-4 (RGD+DOTA+Gd^{3+})	1.53	34.62	Cells adhered

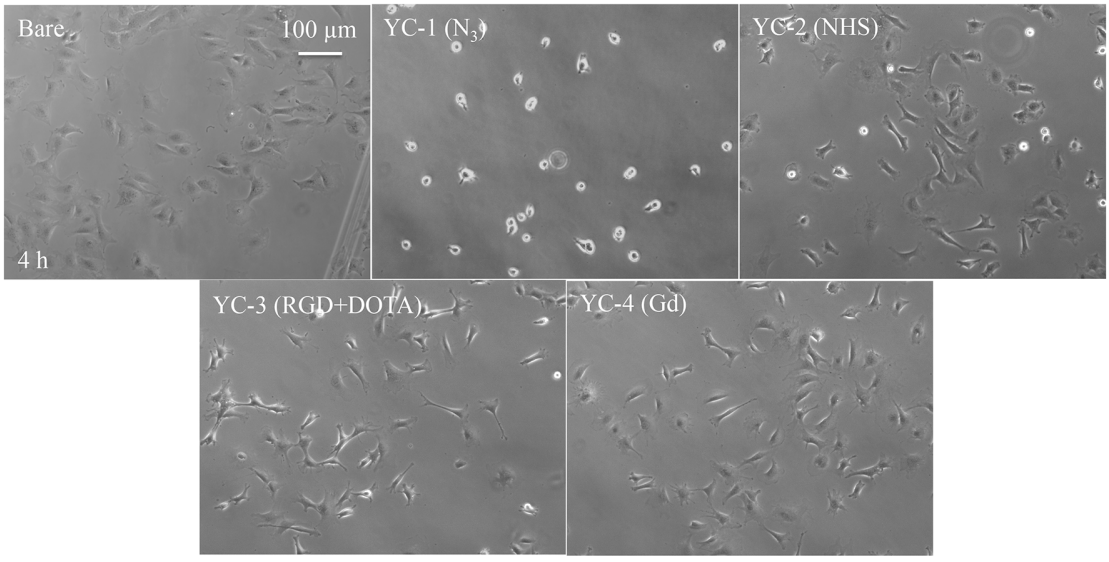

Figure 6.1.23 Representative images of MC3T3 cell adhesion on bottom-up coating surfaces by 2nd Y-shape strategy. YC-3 (RGD+DOTA) and YC-4 (RGD+DOTA+Gd^{3+}) induced obvious cell adhesion, however, not better than on YC-2 (NHS) surface.

The 3rd Y-shape strategy is described in ***figure 6.1.24***. c(RGDfK)C and maleimide-DOTA-GA were reacted first based on the 2nd Y-shape strategy. Afterwards BCN-NHS reacted onto this RGD-DOTA 2-in-1 molecule through NHS-amine reaction in the presence of TEA, thus **BCN-RGD-DOTA (BRD)** 3-in-1 Y-shape molecule was obtained. The molecular weight and size of BCN-NHS was relative small, which was expected to penetrate through the steric barrier to react with amine group. The grafted BCN-NHS could also serve as a spacer to let residual BCN react with azide on YC-1 (N_3) surface by high efficiency SPAAC click reaction. Excess RGD-DOTA was used to react with BCN-NHS for converting all BCN-NHS into BRD. Theoretically, even though the coating efficiency of BRD was not 100 %, there will be only BRD or azide groups on the surface. In the followed cell adhesion study on NV diamond surface constructed by this strategy, cell adhesion induced by RGD peptide will definitely cause a change of DOTA chelated Gd. By this strategy, a relatively "clean" surface without any interference could be obtained. As an alternative of BCN-NHS, DBCO-PEG_4-NHS (***figure 6.1.25***), which also contains cyclo-alkyne was used to react with RGD-DOTA as well, to render **DBCO-RGD-DOTA (DRD)**. The spacer of 4 repeating units of EGs may increase the efficiency to interact with azide on YC-1 (N_3) surface. BRD or DRD were coated onto YC-1 (N_3) surface either in DMF solution or in DMF/H_2O 1:9 mixed solution. The obtained different surfaces were compared. The thickness of polymers on surfaces coated by BRD or DRD in DMF or in DMF/H_2O

with Gd^{3+} loaded is listed in ***table 6.1.11***. Polymer thickness almost remained the same, after BRD or DRD was immobilized in DMF. Meanwhile, polymer thickness decreased a lot, after BRD or DRD was immobilized in DMF/H_2O. By coating with DRD in DMF/H_2O, polymer thickness was fitted to be close to 0. It meant coating in DMF/H_2O might be not stable. In order to further confirm whether the polymers existed or not after coating by BRD and DRD in DMF or in DMF/H_2O, BSA non-specific adsorption on these 4 different coated surfaces were tested in QCM-D. ***Figure 6.1.26~6.1.30*** show the BRD or DRD coating on Qsensors in DMF or in DMF/H_2O, as well as subsequent BSA adsorption on these coated surfaces. Neither coatings of BRD nor DRD caused any frequency shift due to the low reaction efficiency and small molecular weight. There was also technical problem that baseline in DMF could not get equilibrated. However, the adsorption of BSA on BRD and DRD coated surfaces behaved differently, as listed in ***table 6.1.12***. Large amount of BSA was non-specifically adsorbed on bare slide (***Figure 6.1.27***), while almost no BSA adsorption was detected on silane-PEG-N_3 coated surface, corresponding with anti-fouling effect on this surface described in earlier strategies. Similarly, almost no BSA adsorption was detected on surfaces coated by BRD in DMF and in DMF/H_2O, as well as surface coated by DRD in DMF, indicating the existence of PEG polymers on these surfaces. However, some BSA adsorbed on surface coated by DRD in DMF/H_2O. This indicated that some of the polymers might be detached in the coating process to leave exposed bare islands causing non-specific BSA adsorption. MC3T3 and LAMDCK cell adhesion experiments were also performed on BRD or DRD coated glass slides and Qsensors, respectively. Cell adhesion images are shown in ***figure 6.1.31~figure 6.1.33***. Both MC3T3 and LAMDCK cells spread slightly better on surfaces coated in DMF, than on surfaces coated in DMF/H_2O, indicating higher

stability or higher coating efficiency in DMF. Finally, BRD coated silicon wafers were analyzed by XPS, as shown in ***table 6.1.13***. Compared with bare Si slide, the content of Si decreased, while the contents of O, C, N all increased, and Gd was detected on the BRD coated surfaces. The content ratio of N/C on the surfaces matched the N/C atom constitution of respective polymers. Therefore the XPS results confirmed the successful binding of BRD both in DMF and in DMF/H_2O. Combining the results above, coating of BRD or DRD in DMF was more stable than coating in DMF/H_2O. Therefore, the 3rd Y-shape strategy with BRD grafting in DMF was regarded as an optimized method to fabricate Y-shape force sensor with long PEG chain (Y-shape L) on NV diamond for the following cell adhesion studies.

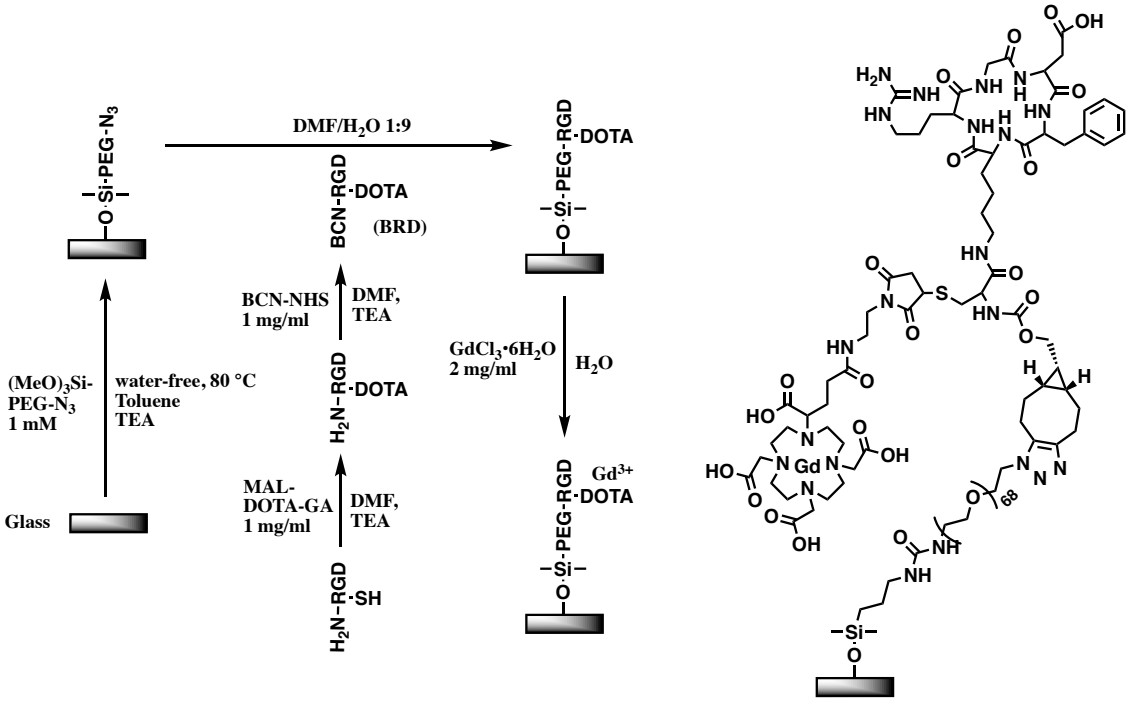

Figure 6.1.24 3rd Y-shape bottom-up coating procedure. c(RGDfK)C and maleimide-DOTA-GA were reacted together first. Then BCN-NHS was reacted onto this RGD-DOTA 2-in-1 molecule, generating BCN-RGD-DOTA (BRD) 3-in-1 Y-shape molecule. BRD was then coated onto YC-1 (N_3) surface by high efficiency SPAAC click reaction.

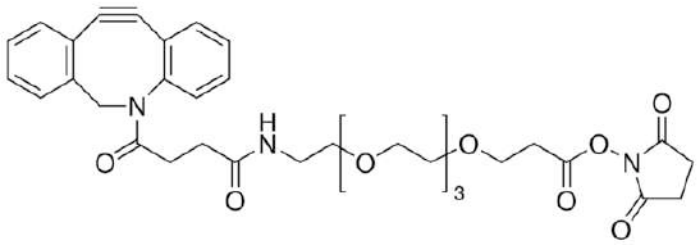

DBCO-PEG4-NHS

Figure 6.1.25 Molecular structure of dibenzocyclooctyne-PEG4-N-hydroxysuccinimidyl ester DBCO-PEG4-NHS

Table 6.1.11 Thickness (nm) of bottom-up coating surfaces by 3rd Y-shape strategy using 4 different methods

4 methods	BRD in DMF/H_2O	BRD in DMF	DRD in DMF	DRD in DMF/H_2O
Bare slide	0	0	0	0
YC-1 (N_3)	2.67	2.71	2.86	2.66
YC-3 (RGD+DOTA+Gd^{3+})	1.17	2.32	2.07	0.33

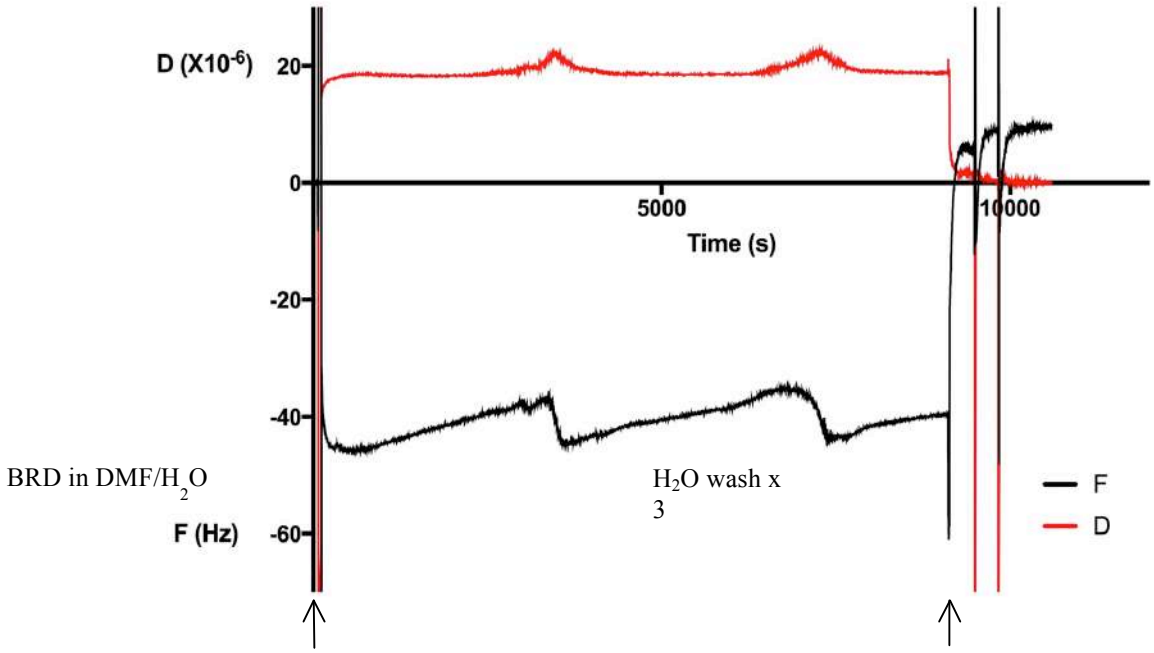

Figure 6.1.26 QCM frequency (F) and dissipation (D) shift as a function of time during binding of BCN-RGD-DOTA (BRD) on $(MeO)_3Si$-PEG-N_3 coated Qsensors in DMF/H_2O. Coating of BRD did not cause a frequency shift, thus the successful binding of BRD in DMF/H_2O could not be confirmed.

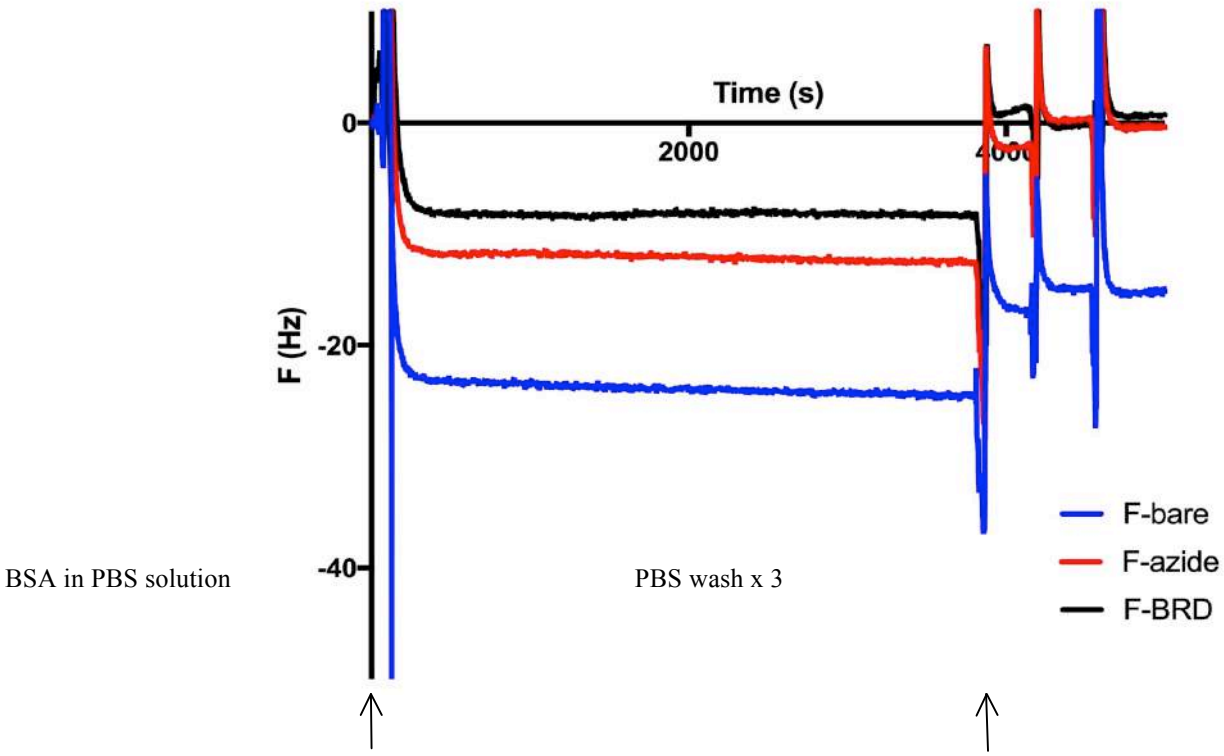

Figure 6.1.27 QCM frequency (F) and dissipation (D) shift as a function of time during adsorption of BSA on Y-shape surface constructed by BRD in DMF/H_2O. Large amount of BSA was non-specifically adsorbed on bare slide, while almost no BSA adsorption was detected on silane-PEG-N_3 coated surface and BRD coated surface.

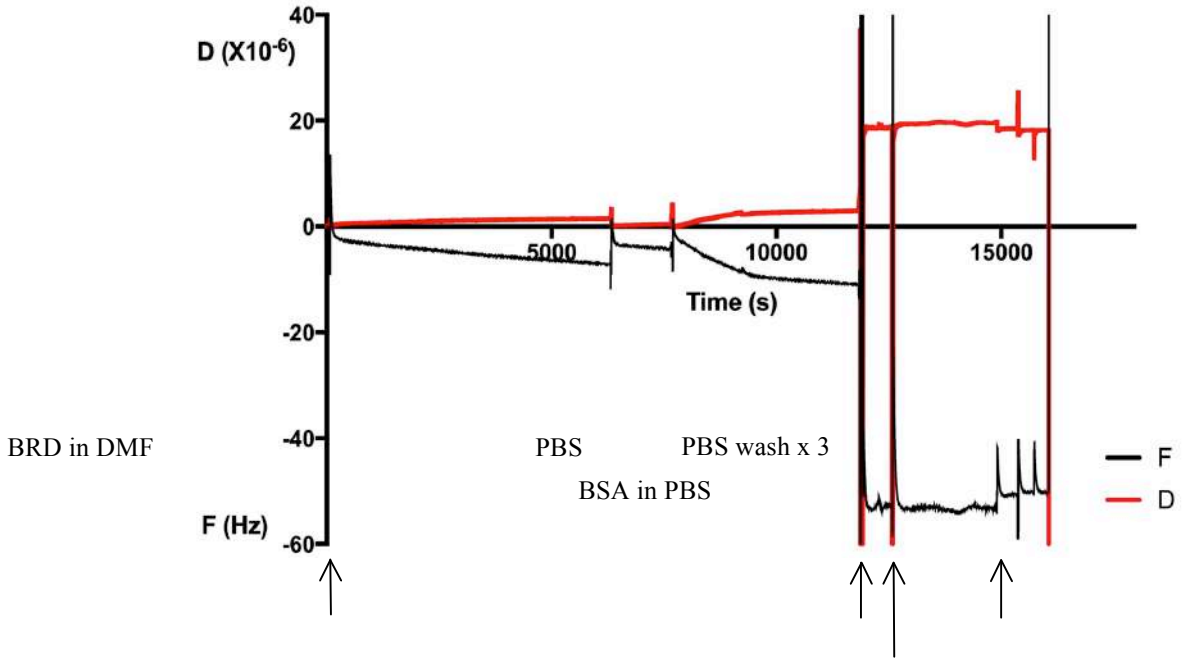

Figure 6.1.28 QCM frequency (F) and dissipation (D) shift as a function of time during binding of BCN-RGD-DOTA (BRD) on $(MeO)_3Si$-PEG-N_3 surface in DMF and subsequent adsorption of BSA. Coating of BRD did not cause an obvious decrease of frequency. However, subsequent BSA adsorption almost did not cause any frequency shift, indicating existence of anti-fouling PEG polymer monolayer on the surface.

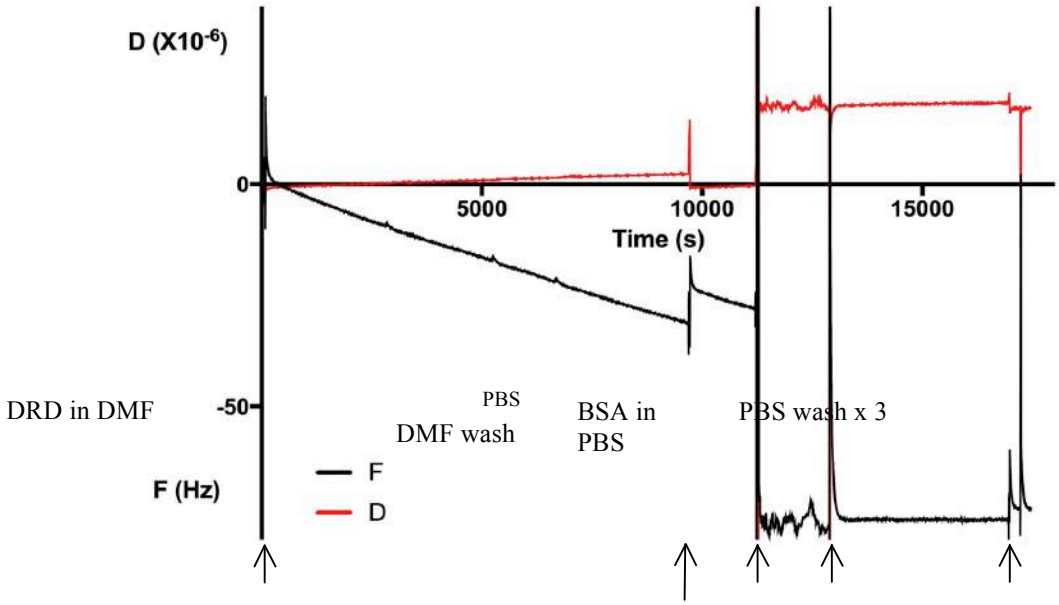

Figure 6.1.29 QCM frequency (F) and dissipation (D) shift as a function of time during binding of DBCO-RGD-DOTA (DRD) on $(MeO)_3Si$-PEG-N_3 surface in DMF and subsequent adsorption of BSA. Coating of DRD did not cause an obvious frequency shift. Subsequent BSA adsorption almost did not cause any frequency shift, indicating existence of anti-fouling PEG polymer monolayer on the surface.

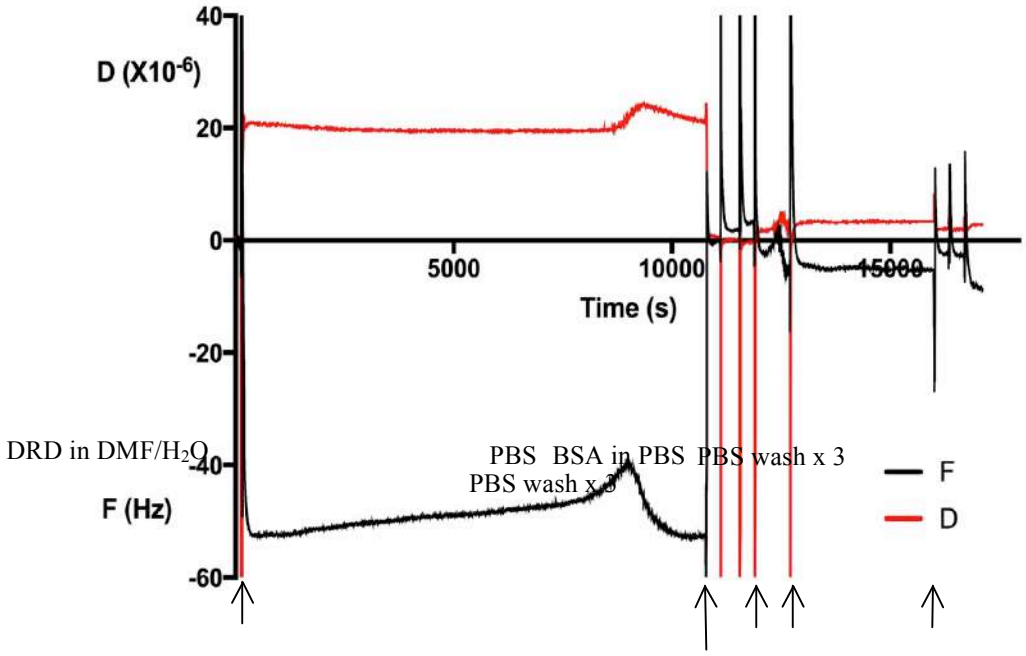

Figure 6.1.30 QCM frequency (F) and dissipation (D) shift as a function of time during binding of DBCO-RGD-DOTA (DRD) on $(MeO)_3Si$-PEG-N_3 surface in DMF/H_2O and subsequent adsorption of BSA. Coating of DRD did not cause an obvious frequency shift. Subsequent BSA adsorption did cause a frequency shift, indicating a BSA adsorption amount of around 70.8 ng/cm^2 on DRD coated surface. This indicated that some of the polymers might be detached in the coating process to leave exposed bare islands causing non-specific BSA adsorption.

Table 6.1.12 BSA adsorption on 3rd Y-shape strategy constructed surfaces by 4 different methods

Different surfaces	Bare slide	N_3	BRD in DMF/H_2O	BRD in DMF	DRD in DMF	DRD in DMF/H_2O
BSA adsorption amount (ng/cm^2)	265.5	0	0	0	0	70.8

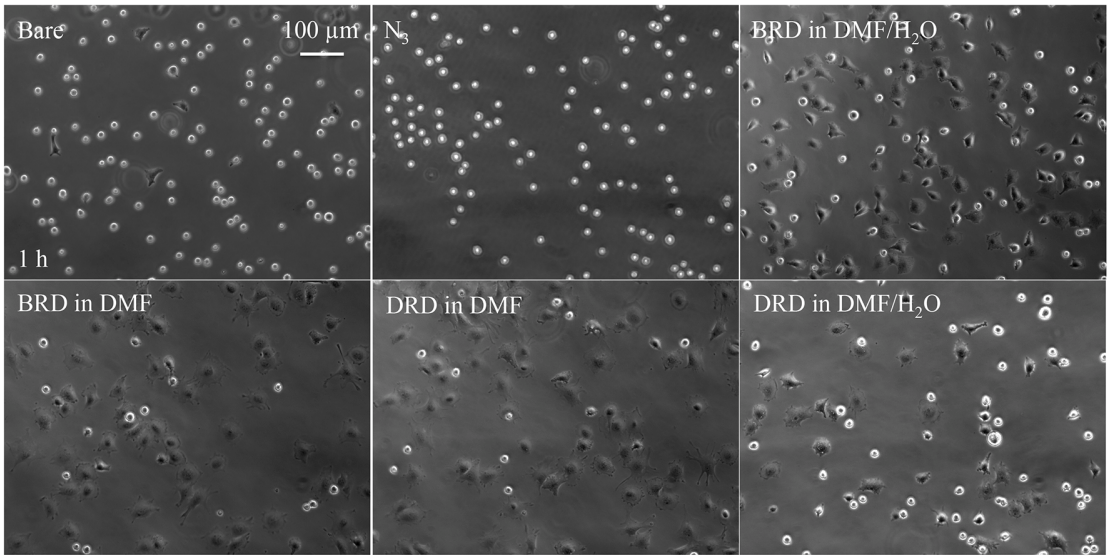

Figure 6.1.31 Representative images of MC3T3 cell adhesion at 1 h on bottom-up coating surfaces by 3rd Y-shape strategy using 4 different methods (1 h). On bare slide, there was little amount of cells adhered. On $(MeO)_3Si$-PEG-N_3 coated surface, there were no cells adhered since it is anti-fouling. On BRD or DRD coated in DMF surfaces, cells adhered better than on BRD or DRD coated in DMF/H_2O surfaces.

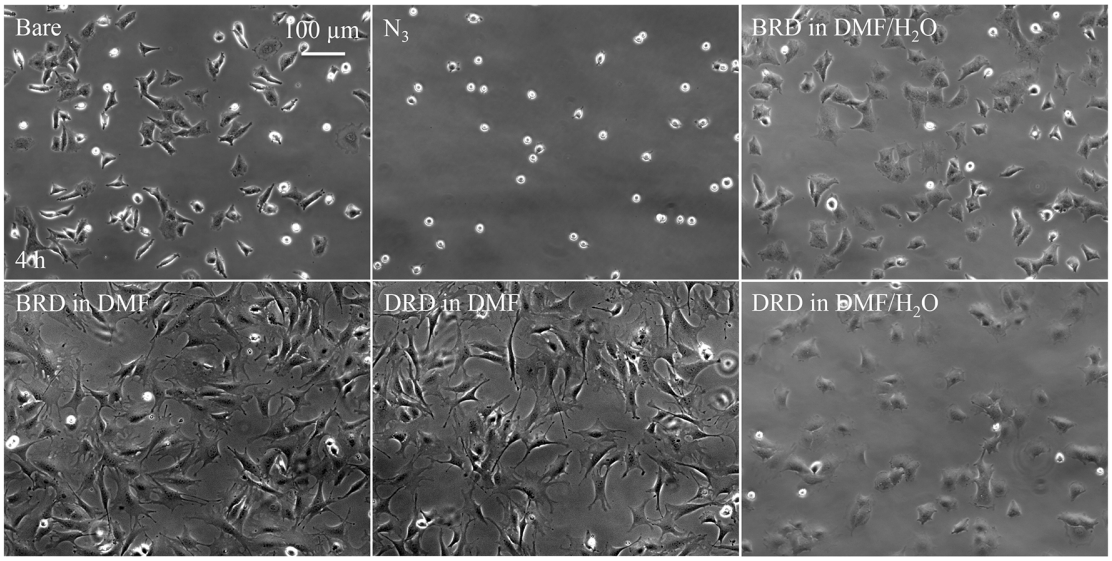

Figure 6.1.32 Representative images of MC3T3 cell adhesion at 4 h on bottom-up coating surfaces by 3rd Y-shape strategy using 4 different methods (4 h). On bare slide, there were some cells adhered. On $(MeO)_3Si$-PEG-N_3 coated surface, there were no cells adhered. On BRD or DRD surfaces coated in DMF, cells adhered much better than on in surfaces coated in DMF/H_2O.

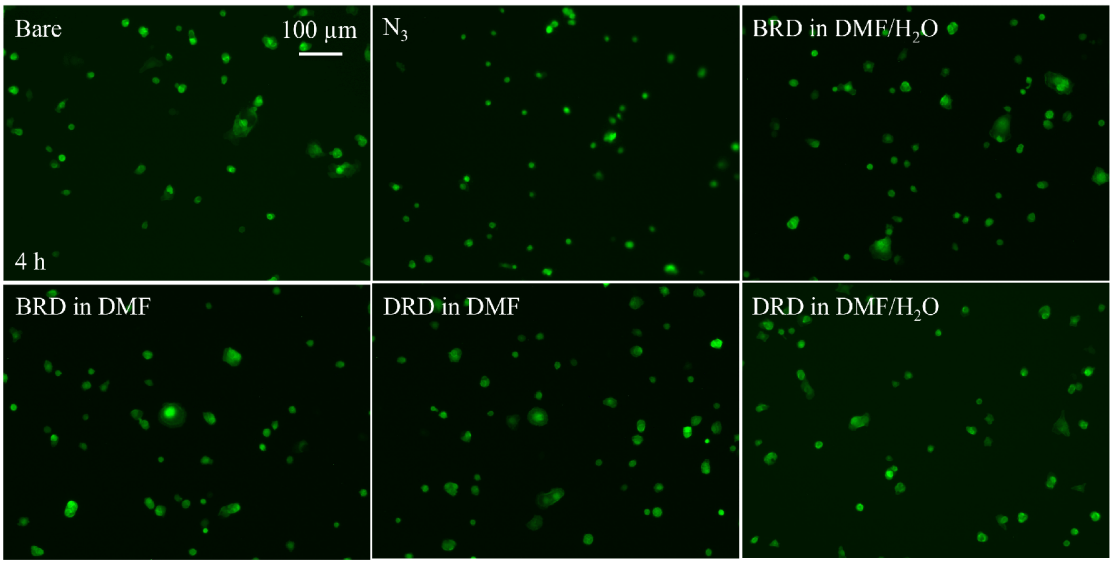

Figure 6.1.33 Representative images of LA-MDCK cell adhesion at 4 h on QCM-D sensors surfaces constructed by 3rd Y-shape strategy using 4 different methods (4 h). On bare slide, there were some cells adhered. On $(MeO)_3Si$-PEG-N_3 coated surface, there were little cells adhered since it is anti-fouling. On BRD or DRD surfaces coated in DMF, cells adhered better than on BRD or DRD surfaces coated in DMF/H_2O.

Table 6.1.13 Atom constitutes on 3rd Y-shape strategy constructed surfaces by XPS

Samples		Elements				
		Si	O	C	N	Gd
Bare	Area percentage %	56.67	32.06	10.56	0.29	-
YC-1 (N_3)	Area percentage %	41.43	31.06	26.67	0.84	-
	Theoretical atom number	-	69	142	5	0
YC-2 (RGD+DOTA+Gd^{3+}) BRD in DMF/H_2O	Area percentage %	46.97	32.11	19.10	0.77	0.78
	Theoretical atom number	-	90	207	21	1
YC-2 (RGD+DOTA+Gd^{3+}) BRD in DMF	Area percentage %	41.28	32.75	24.89	0.77	0.26
	Theoretical atom number	-	90	207	21	1

6.1.2.4 Bottom-up construction of Y-shape force sensor with short PEG chain (Y-shape S)

In Y-shape L, PEG of molecular weight ~3000 Dalton was used. However, if the PEG chain is too long, the distance between Gd^{3+} on one terminal of force sensor and NV at the bottom may be too long to get strong T1 signal. The distance between Gd^{3+} and NV is shorter, the stronger the signal can be. Therefore, Y-shape force sensor with short PEG chain (Y-shape S) was developed as an improved strategy, in which PEG with molecular weight ~800 Dalton was used.

In order to obtain Y-shape S, $(MeO)_3Si$-PEG-N_3 with MW 800 Dalton was first coated onto glass, silicon wafer, or SiO_2-based Qsensor through silane groups.

Afterwards BCN-RGD-DOTA (BRD) 3-in-1 Y-shape molecule was coated onto azide groups on the surface in DMF, as the same procedure to obtain Y-shape L described above. The thickness after each step of coating is listed in ***table 6.1.14***. The polymer layer thickness was fitted to be ~2 nm after silane-PEG-N_3 coating, and almost remained the same after BRD coating. After the constructed Y-shape S coating was immersed in PBS for 2 weeks, the polymer thickness did not change. This is evidence that Y-shape S obtained by this strategy is stable in physiological buffer. The immobilization of BRD was also monitored by QCM-D in DMF/H_2O 1:9 as shown in ***figure 6.1.34***. After washing by water, the binding amount of BRD was calculated to be ~177 ng/cm^2 from frequency shift. The smaller diameter of the short PEG chains led higher density of functional groups; and the functional groups on short chain can be better exposed on the surface. Thus the immobilization of BRD on short PEG chain was detected by QCM-D, which was not detected on long PEG chain. Additionally, cell spreading on BRD coated Qsensor in ***figure 6.1.35*** further confirmed the successful immobilization of BRD. MC3T3 cell adhesion on different surfaces is summarized in ***table 6.1.15***. Cell images are shown in ***figure 6.1.36***. Silane-PEG-N_3 coated surface was still anti-fouling, while cells spread very well due to RGD-integrin interaction on BRD coated surfaces. Gd^{3+} did not affect cell spreading. Therefore, Y-shape force sensor with short PEG chain (Y-shape S) obtained by this method can be used as a stable and effective force sensor.

Table 6.1.14 Thickness (nm) of bottom-up coating surfaces for Y-shape S

Different step of surface	Thickness (nm)
Bare slide	0
YC-1 (N_3)	2.02
YC-2 (RGD+DOTA)	2.23
After in PBS 2 weeks	2.30

BRD DMF/H_2O H_2O wash x 3

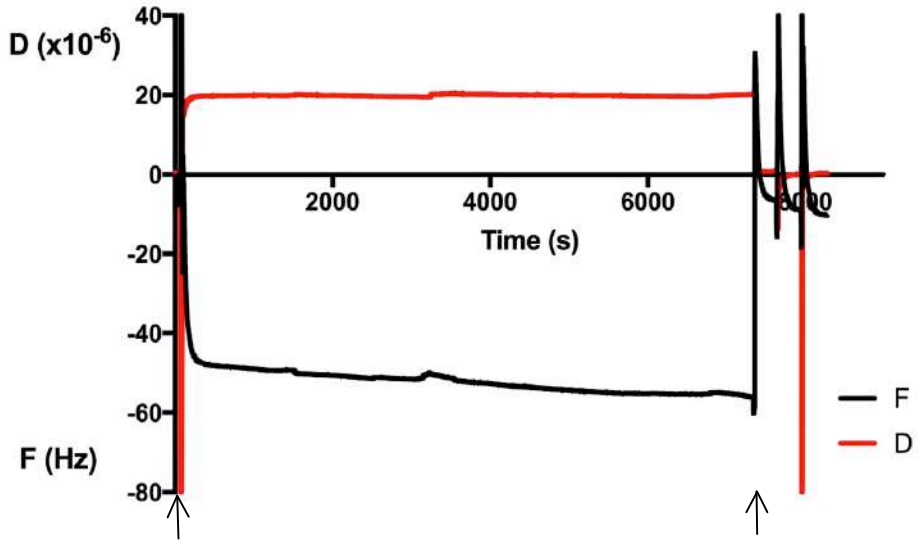

Figure 6.1.34 QCM frequency (F) and dissipation (D) shift as a function of time during binding of BCN-RGD-DOTA (BRD) on $(MeO)_3Si$-PEG-N_3 coated Qsensors in DMF/H_2O for Y-shape S. Coating of BRD caused an obvious frequency shift indicating a successful binding amount of around 177 ng/cm^2 BRD in DMF/H_2O.

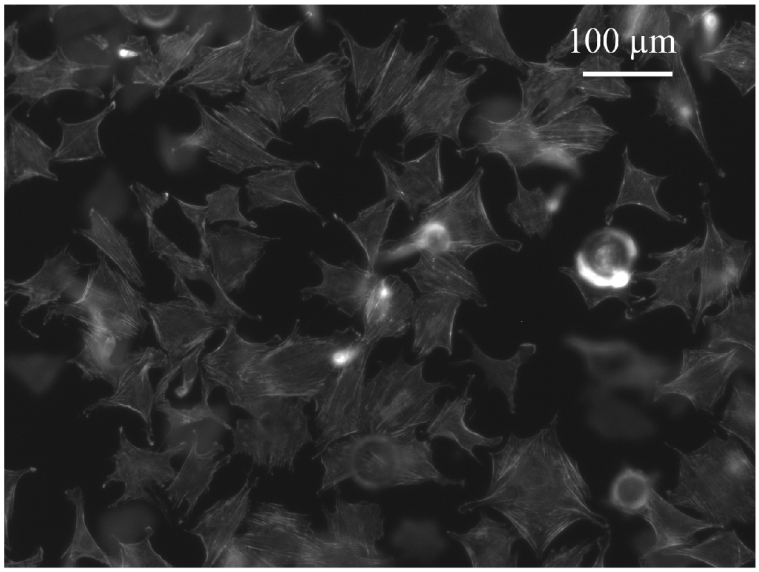

Figure 6.1.35 Representative images of stained MC3T3 cell adhesion on BRD bound Q-sensor for Y-shape S. Cells well adhered on BRD coated Qsensor, indicating successful binding of BRD in Y-shape S construction.

Table 6.1.15 MC3T3 cell adhesion on the Y-shape S constructed surfaces

Adhesion time	Bare slide	N_3	BRD in DMF	BRD+Gd^{3+}
1 h	Some cells adhered	Almost no cells adhered	Cells adhered very well	Cells adhered very well
4 h	Some cells adhered	Few cells adhered	Cells adhered very well	Cells adhered very well

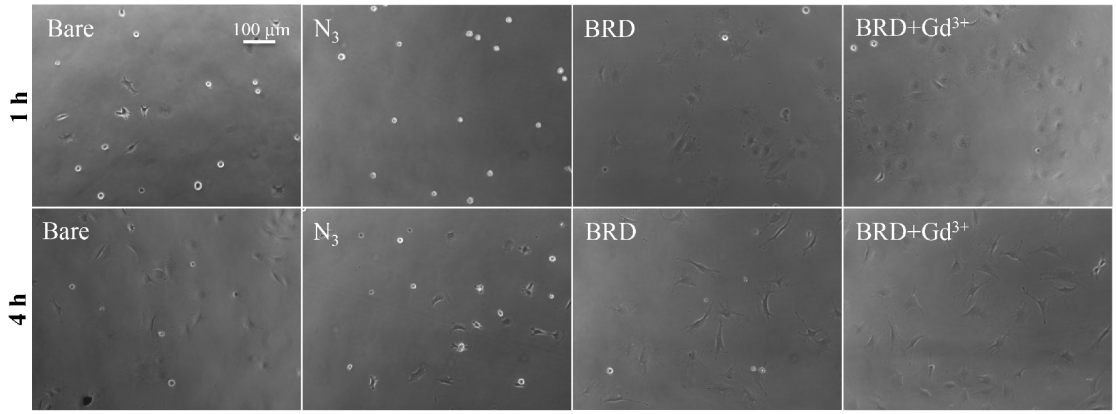

Figure 6.1.36 Representative images of MC3T3 cell adhesion images of bottom-up coating surfaces for Y-shape S. $(MeO)_3Si$-PEG-N_3 coated surface was almost anti-fouling. On BRD coated surfaces, cells spread very well due to RGD-integrin interaction. Gd^{3+} did not affect cell spreading.

6.1.3 Cell adhesion on Y-shape diamond force sensor

Y-shape L and Y-shape S strategies were tested on glass, silicon wafer, and Qsensor as described above. However, for the following cell-adhesion study on NV diamond, it needs to be proved that they can be applied onto diamonds as well, since diamond surface may differ from the tested surfaces. Cell adhesion experiments were performed with Y-shape L and Y-shape S functional diamond surfaces. For proving Y-shape L, one diamond testing sample was first coated with SiO_2 of ~5 nm by method *a*, then Y-shape L was constructed above. MC3T3 cells on this Y-shape L coated diamond surface spread much better than on bare diamond without any modification or on silica-coated diamond, as shown in ***figure 6.1.37***. For proving Y-shape S, one diamond testing sample was first coated with SiO_2 of ~2 nm by method *b*, then Y-shape S was constructed above. MC3T3 cell adhesion on Y-shape S coated diamond surface also spread much better than on bare diamond without any modification or on silica-coated diamond, as shown in ***figure 6.1.38***. In order to test the Y-shape S stability on diamond in aqueous condition, the adhered cells were washed off by trypsin and diamonds were immersed in PBS for 1 week. Cell adhesion was tested again and matched the results for the tests on fresh slides. These results demonstrated the successful construction of Y-shape S and it is stable in PBS for 1 week. Therefore both Y-shape L and Y-shape S could be applied on NV diamonds for relaxation time (T1) measurements in cell adhesion study.

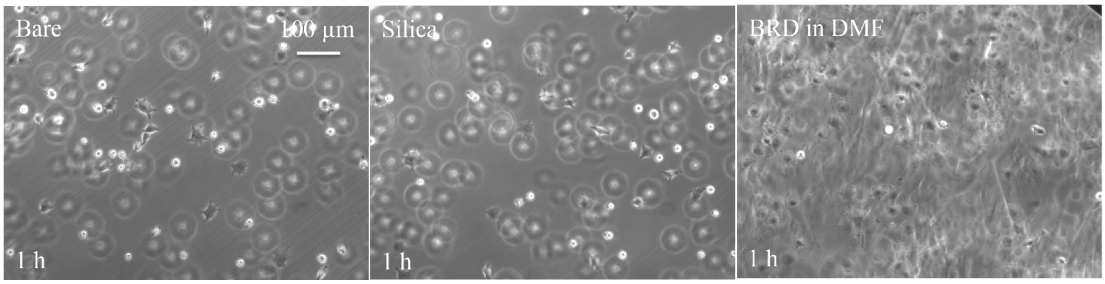

Figure 6.1.37 Representative images of MC3T3 cell adhesion at 1 h on Y-shape L constructed diamond surface (1 h). On Y-shape L constructed diamond surface by coating BRD in DMF, MC3T3 cells spread much better, than on bare diamond without any modification or on silica-coated diamond.

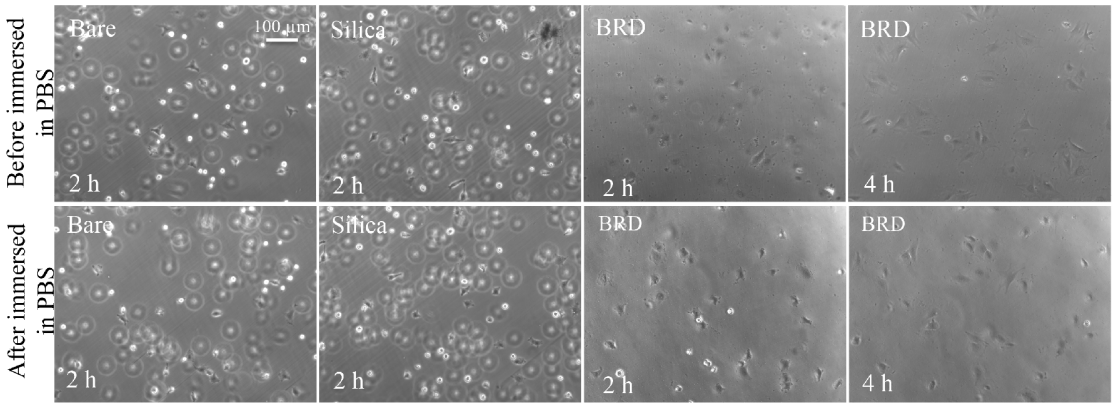

Figure 6.1.38 Representative images of MC3T3 cell adhesion at 2 h on Y-shape S constructed diamond surface (2 h). On both bare diamond and silica coated diamond, there were some cells adhered. On Y-shape S constructed diamond surface by coating BRD in DMF, cells adhered much better. After immersed in PBS for one week and loaded by cells again, cells still adhered very well, indicating good stability of Y-shape S construction in PBS.

6.1.4 Relaxation measurements

The constructions described above were applied onto diamond membranes, and loaded with Gd^{3+} ions. The Gd^{3+} rendered T1 changes were detected by relaxation measurements in wide-field setup. In order to estimate the T1 change on Y-shape force sensor on diamond membranes, a simple 2D model describing the construction was considered, as shown in ***figure 6.1.39***.

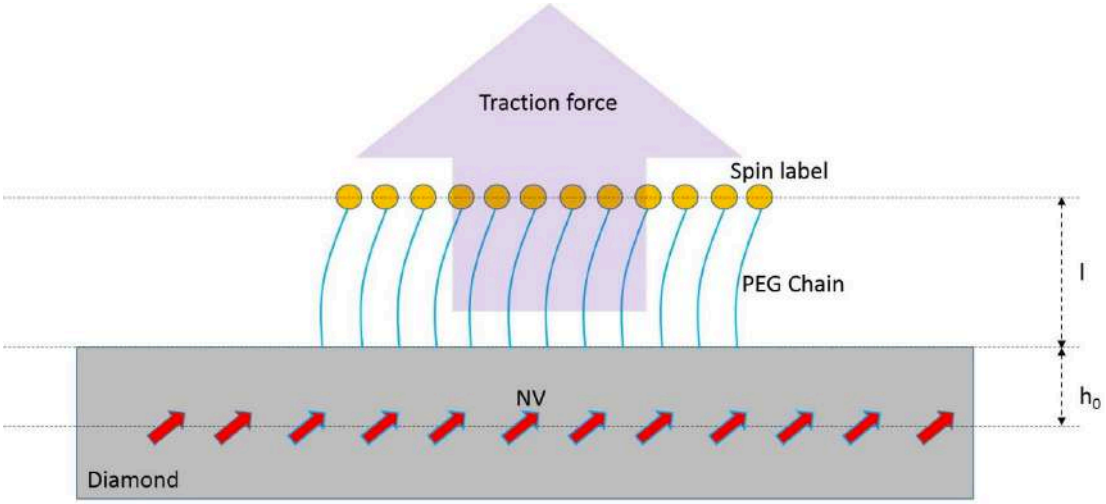

Figure 6.1.39 Y-shape force sensor 2D model. This illustrates NV sensing cell traction force when directly grafted PEG with spin label on top of diamond surface. Where $h=l+h_0$, l is the length of the PEG as spacer and h_0 is the typical NV implantation depth (e.g., 5 nm). As an example, the l=5 nm is chosen (see below description) and therefore $\boldsymbol{h}$=**10** $\boldsymbol{nm}$ is the typical value.

For convenience, we consider an area of A ~ 0.25 μm^2 (e.g., spot size of laser: 500 nm × 500 nm). We assume the force is along the axial of the PEG and consider an elastic model at the beginning (the linear relationship is only valid within certain range).[143] Therefore the $F = AEdx/L$, where A is the cross-section area ($A = N*a_0^2$,

N is the number of PEG molecules and a_0 is the diameter of a single PEG molecule), E is the Young's modulus and L is the length of PEG molecule. Under force F the exerted length change dx can be calculated: $dx = FL/(AE)$ (1)

Take some typical values for the system: we assume the typical length of PEG is L = 5 *nm*, and totally N = 5000 PEG molecules grafted inside the chosen area (grafting density is PEG/50 nm^2). The diameter of PEG is a_0 = 0.5 *nm*.[144] The Young's modulus is E = 1 *Mpa*.[145] From the literature, we found the relationship between traction force and contact area is ~ 5 nN/μm^2.[146] Thus the exerted force on the chosen area (0.25 μm^2) is ~ 1.25 nN. Therefore, the exerted length change (under 1.25 nN) is calculated through equation (1) to be: 5 nm. The NV relaxation rate $\Gamma = \Gamma_{int} + \Gamma_{ext}$, where Γ_{int} is the intrinsic feature of diamond (treated as constant) and Γ_{ext} depends on the external spin noise. After calculation,[147] the Γ_{ext} is found to scale with h^{-3}, where h is the distance between the NV and external spin label. From this, we can estimate the change of relaxation rate as a function of distance h as shown below.

Figure 6.1.40 shows calculated relative relaxation rate of NV centers (induced by spin labels) as a function of distance between NV and spin label. The relative rate at a given distance is calculated as a ratio to typical R_{10} (relaxation rate at h=10 *nm*) through h^{-3} scaling. The distance change of 5 nm is quite significant for our relaxometry detection, as shown in stretch from 10 nm to 15 nm $R_{10\text{-}15} = 3.375\ R_{10}$ (R is the relaxation rate at h=10 nm). This is quite significant change according to the T1 relaxation measurement, and therefore the force should be measurable.

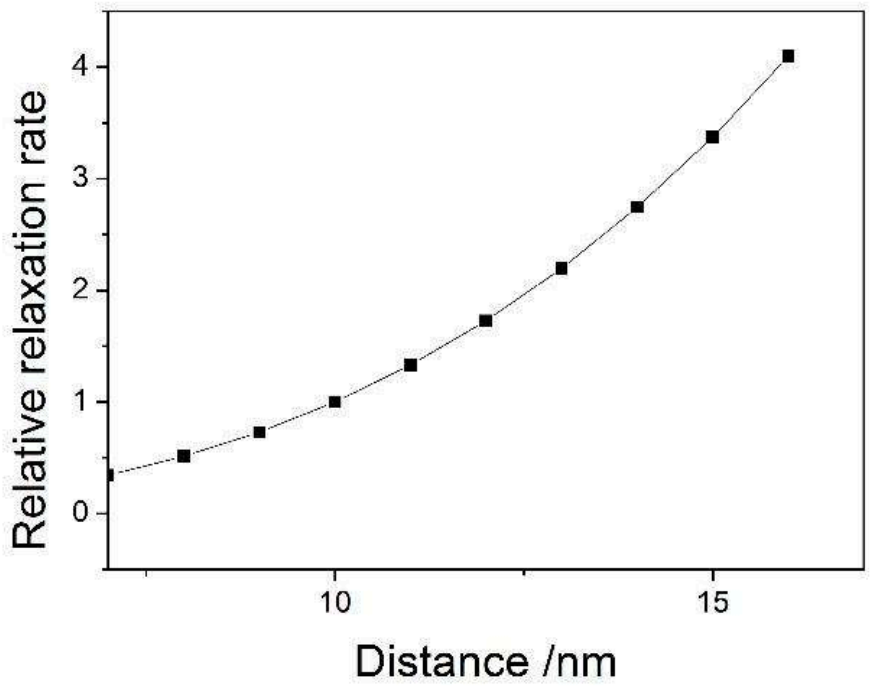

Figure 6.1.40 Calculated relative relaxation rate of NV centers (induced by spin labels) as a function of distance between NV and spin label. The relative rate at a given distance is calculated as a ratio to typical R_{10} (relaxation rate at h=10 nm) through h^{-3} scaling.

The influence of liquid pressure (h = 1 cm) is considered: $F = \rho ghA = 2.5\times10^{-2}\ nN$. Since this is two order smaller than the force we discussed, we can neglect this influence of liquid pressure. Similarly, we can also neglect the influence of gravity of a single cell, which is also on the order of $10^{-2}\ nN$.

An estimation of distance between Gd^{3+} and NVs in diamond was performed based on the fact that the depth of NV implantation was 5 nm.

d = D+S+L

where D is the depth of NV implantation 5 nm, S is the silica layer thickness 5 nm for Y-shape L, 2 nm for Y-shape S, L is the length of polymer chain, which can be considered by two times of Flory radius R_F.[148] $R_F \approx IN^{\lambda}$, where I is the monomer length 0.28 nm and N is the degree of polymerization, λ is the Flory exponent. The lengths of PEG in different states are listed in ***table 6.1.16***.

Table 6.1.16 PEG lengths in different states

	Dry state length (nm)	Hydrated length (nm)	Contour length (nm)
PEG 3000	**2.26**	**7.05**	**19.09**
PEG 800	**1.46**	**3.20**	**5.09**

6.1.4.1 Relaxation measurement for Y-shape L

For the first test, Gd^{3+} resulted T1 change was monitored by PEG length in different solvent. NV diamond was modified by LS (B): PEG with MW 3000 Da was directly combined with Gd^{3+} chelator DOTA. After loading with Gd^{3+} ions, T1 was measured in sequence of in ambient condition, in water, in isopropanol, and again in ambient condition. Isopropanol is a non-solvent for PEG. The PEG chains on the NV diamond surface are supposed to be collapsed in ambient condition or in isopropanol. This may cause a smaller distance between Gd^{3+} on top of the PEG chain and NVs in diamond, resulting a lower T1 value. As a comparison as in water, which is a good solvent for PEG, PEG chains are supposed to be extended. Therefore a longer distance between Gd^{3+} and NVs is expected, resulting a higher T1 value. ***Figure 6.1.41*** depicts the estimated distance between Gd^{3+} and NVs in different state. The implantation depth

of NVs in diamond was 5-10 nm, the silica coating was about 5 nm. According to ***table 6.1.16***, PEG length in dry state was 2.26 nm, roughly corresponding with the ellipsometry result 2.67 nm. PEG length in water was 7.05 nm. As shown in ***figure 6.1.42***, the T1 exhibited lower values in ambient condition and in isopropanol, compared with in water. However, when the system was dried after isopropanol treatment, the T1 value even increased. Therefore another series of T1 measurements were done in the order of in ambient condition, in isopropanol, in water, in isopropanol, and in water. However, the T1 values in these tests increased when the solvent was changed each time (***figure 6.1.43***). The intrinsic T1 value for the NV diamond sample without any chemistry treatment was around 2 ms, while in the first round of test the values were all below 100 μs. The abnormally low T1 values may be because large amount of Gd^{3+} ions were trapped in PEG chains. They were continuously washed out as each time by changing the solvent. Finally, steady state apparently reached: T1 of 300 to 400 μs in water, 500 μs in ambient condition and in isopropanol. The final results were the opposite of our expectations: shorter Gd^{3+}-NV distance leads to larger T1 value. There were two possible explanations: 1. Changing the PEG conformation may change the mutual interaction between Gd^{3+}. Stronger interaction between Gd^{3+} ions closed to each other in the collapsed state might lead to a broadened spectral density and effectively less noise at the NV transition frequency. 2. Intrinsic paramagnetic defects hosted on the surface of diamond were also expected to exist in the SiO_2 layer, which also interacted with the NVs as indicated in ***figure 6.1.44***. The fluctuations of these defects would be influenced by Gd^{3+} ions at different distances and positions, a broadening of the spectral density might lead to an increased relaxation time of the NVs. However, on the second sample with only the

silica layer on the surface (see below), T1 was measured as ~2 ms, indicating the paramagnetic defects only seemed to play a role when Gd^{3+} was also attached.

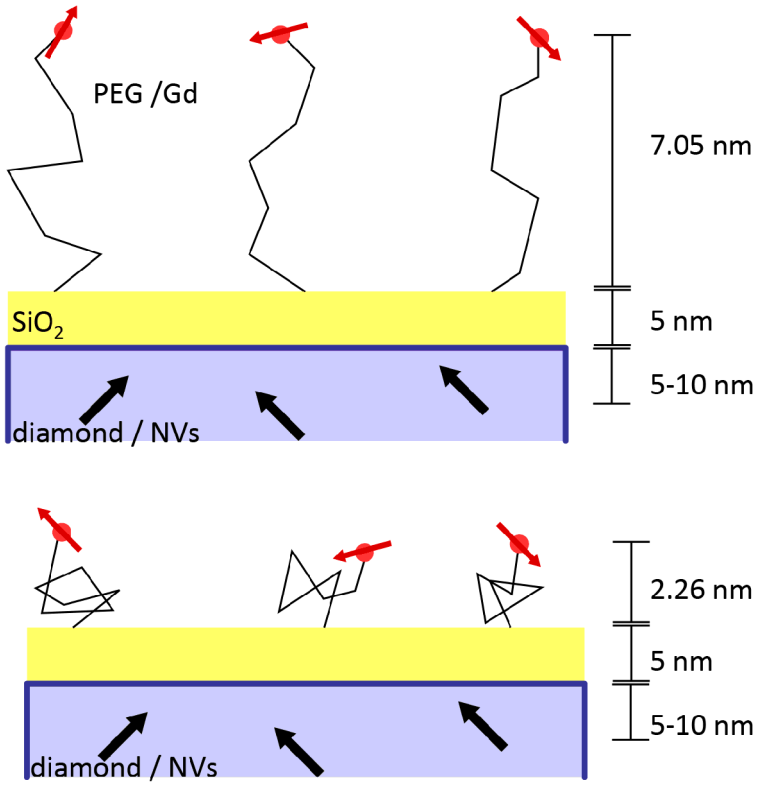

Figure 6.1.41 Distance between Gd^{3+} and NVs in different states. The implantation depth of NVs in diamond is 5-10 nm, silica coating of 5 nm was achieved by method *a*. PEG length in dry state was 2.26 nm, while in water was 7.05 nm.

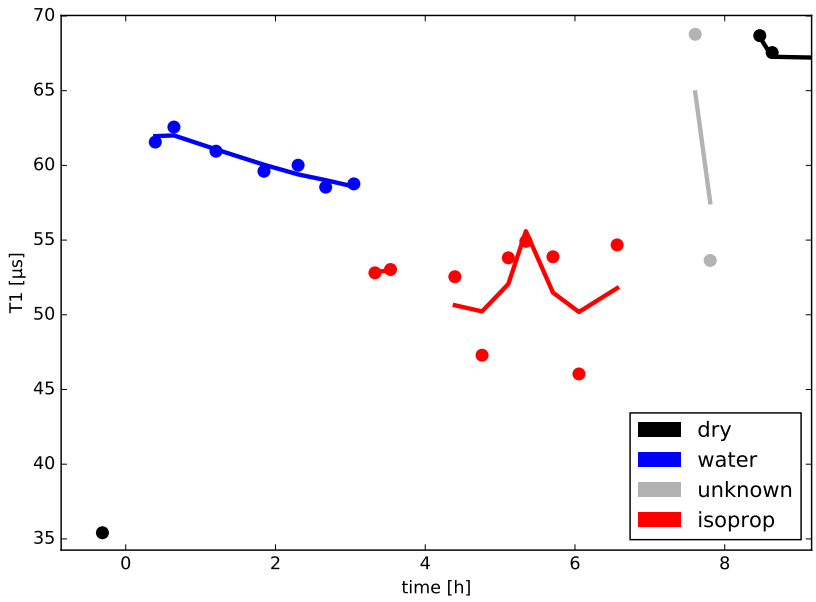

Figure 6.1.42 T1 measurement in different state (1st round). T1 value was lower in dry state and in isopropanol, compared with in water. However, when the system was dried again, the T1 value did not recover.

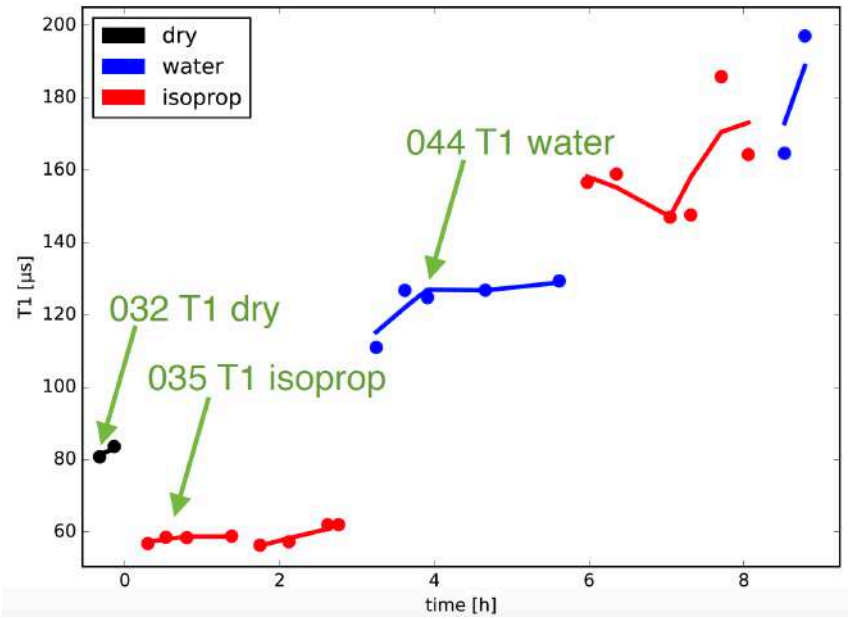

Figure 6.1.43 T1 measurement in different state (2nd round). T1 values in these tests increased as each time of changing the solvent.

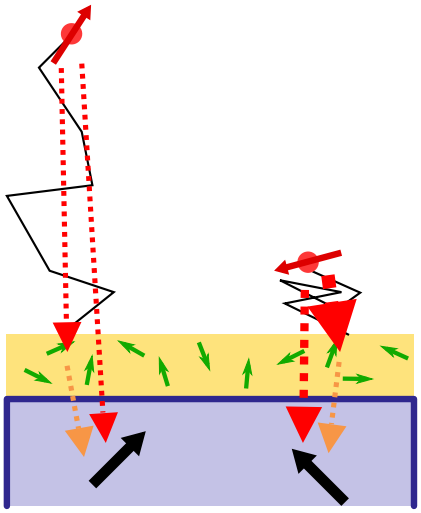

Figure 6.1.44 Paramagnetic defects in silica layer. In addition to direct influence of Gd^{3+} on the NVs, indirect interaction via paramagnetic defects in the silica layer may occur.

The second relaxation measurement was performed on NV diamond with Y-shape force sensor Y-shape L (PEG with MW 3000 Da). First T1 was measured after the generation of ~5 nm silica coating by method *a*. There was almost no influence of silica layer on T1 value compared with intrinsic T1 value (both were measured as ~2 ms). Then the Y shape force sensor Y-shape L was constructed based on the silica layer and Gd^{3+} ions were loaded. Since large amount of Gd^{3+} ions may be trapped by PEG chains as detected in the previous measurements shown above, EDTA was used to remove the unchelated Gd^{3+} ions but not influencing the Gd^{3+} ions in DOTA chelator.[149] The measured T1 was around 1 ms after removing unchelated Gd^{3+}. However, no difference was detected in water and in isopropanol. MC3T3 cells were incubated on the Y-shape L force sensor for 4 hours. Cells attached but did not spread as well as in the previous experiments on diamond testing samples. The reason may be the silica coating on NV diamond was not stable or the coating efficiency of RGD peptide was low. Nevertheless, T1 measurement was performed at the region of an

adhered cell. ***Figure 6.1.45*** shows the lifetime T1 map for a part of the adhered cell. The higher value of T1 around 1600-1800 μs corresponded with the region of cell edge as indicated in the figure, where lamellipoda exerted traction force on the substrate. The rest region mostly had lower T1 value, indicating smaller traction force under the inner part of cell and another side of cell edge without lamellipodia. This result revealed that the Y-shape L on NV diamond could be utilized as a cell force sensor. PEG chains contacted with cells through RGD-integrin interaction were stretched under cell traction force, leading to a larger distance between loaded Gd^{3+} ions and NVs in diamond. It resulted a notable increase of T1 value in this region. However, there was still high level of noise distributed in this area, which may come from the low sensitivity of NVs during measurement. When the distance between Gd^{3+} ions and NVs is large (e.g., >25 nm), the sensitivity of the NVs in diamond to Gd^{3+} is low. Therefore there was a demand of decreasing the length of polymer chain in Y-shape force sensor and the thickness of silica layer for obtaining high quality results.

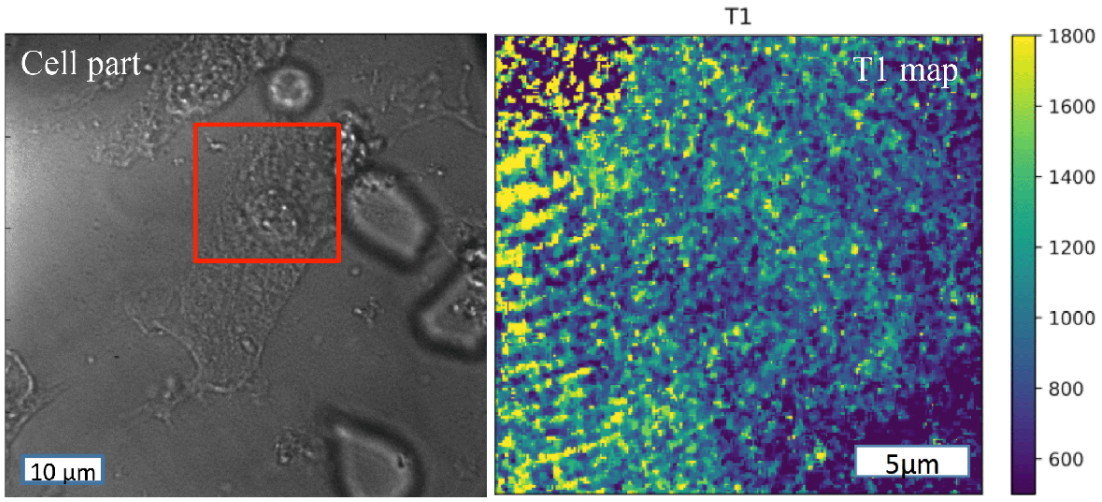

Figure 6.1.45 T1 map above an attached cell on Y-shape L constructed NV diamond. The higher value of T1 around 1600-1800 μs corresponded with the region of cell edge, where lamellipoda exerted traction force on the substrate. The rest region had lower T1 value, indicating smaller traction force under the inner part of cell and another side of cell edge without lamellipodia.

6.1.4.2 Relaxation measurement for Y-shape S

In order to decrease the distance between Gd^{3+} ions and NVs, the thickness of silica layer was reduced to around 1.5 nm by method *a*. Then Y-shape force sensor Y-shape S (PEG with MW 800 Da) was constructed on the silica layer. Gd^{3+} ions were loaded and followed by EDTA washing. The intrinsic T1 value of the diamond membrane was measured as 1-2 ms, while it was around 400 μs after Gd^{3+} loading. After MC3T3 cells were incubated on diamond for 4 hours, T1 was tested again. Since the NV density beneath the chosen cell region was low, the duration was long for single T1 measurement. It resulted an obvious change of cell location in the taken images due to the migration of the tested cell in this time period, as shown in ***figure 6.1.46***. After the measurement, the cell was treated by trypsin and washed off for a reference T1 test without cell on top. The results of two tests were combined together, generating a T1 map of difference (ΔT1). As indicated by the profile of the cell, the higher T1 values occur under the inner part of cell region, demonstrating notable traction force at this region. However, there was no obvious change of T1 at cell edge, indicating absence of strong focal adhesions from this cell. One should notice that the cells did not spread well on this Y-shape force sensor. This may be because the 1.5 nm thick silica layer was not stable enough for supporting the Y-shape construction on NV diamond. Another problem occurred during the relaxation measurement was

that, cells died during the long time measurement, since there was no cell incubator on this wide-field setup.

For another new measurement, a living cell incubator was installed on wide-field setup for cell living condition during measurement. A more stable silica layer of 2 nm was achieved by method *b* on NV diamond. Y-shape force sensor Y-shape S with Gd^{3+} ions was therefore constructed on new silica coatings. After incubation of 4 hours, MC3T3 cells spread on the tested surfaces. Since there were not enough NVs beneath the spread cell, the T1 from only a limited region of a spread cell (edge) was measured. After the measurement, the cell was also treated with trypsin and washed off for a reference T1 test without cell on top. The results of two tests were combined to obtain the difference ΔT1 as shown in ***figure 6.1.47***. The higher T1 values located in the cell region indicated higher cell traction force at this region.

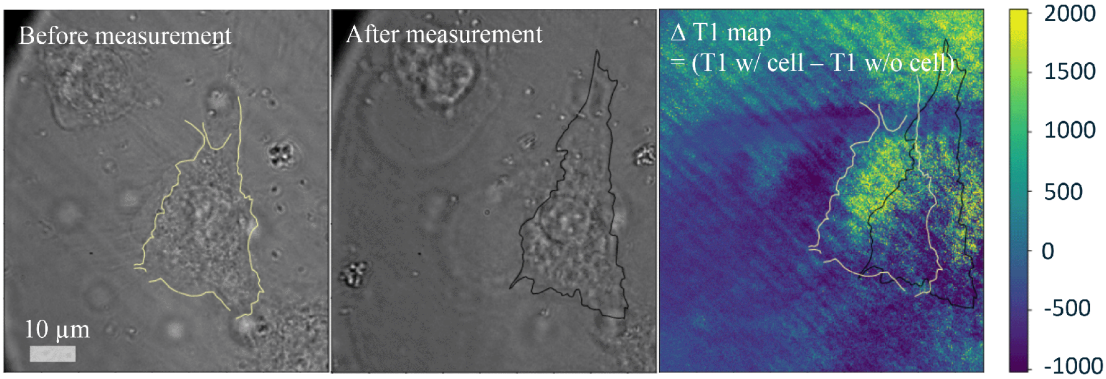

Figure 6.1.46 Δ T1 map above an attached cell on Y-shape S constructed NV diamond. The higher T1 values occur under the inner part of cell region, demonstrating notable traction force at this region. However, there was no obvious change of T1 at cell edge, indicating absence of strong focal adhesions from this cell.

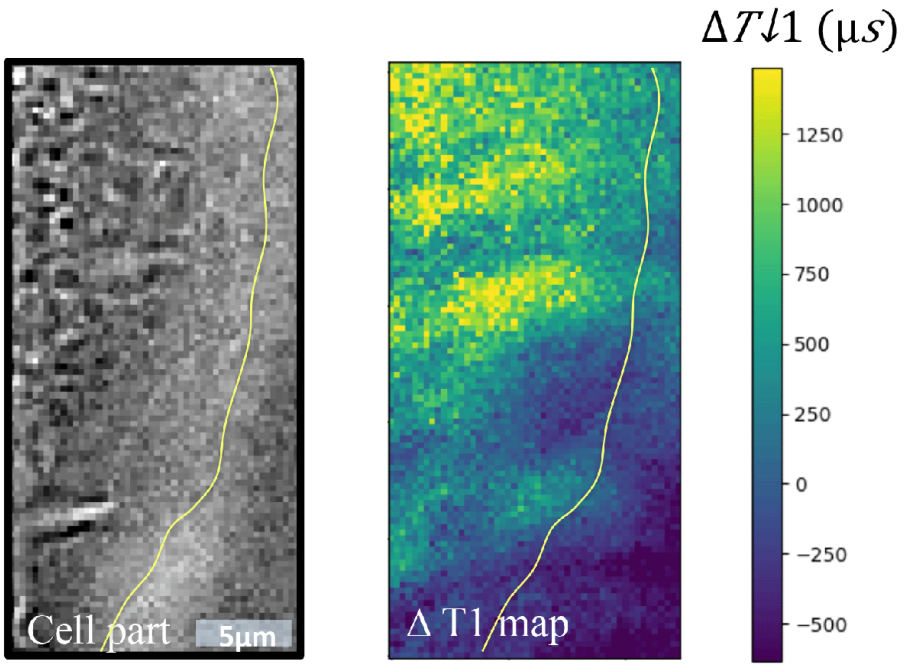

Figure 6.1.47 Δ T1 map above an attached cell on Y-shape S constructed NV diamond with improved silica layer. The higher T1 values located in the cell region indicated cell traction force at this region.

In this chapter, different construction methods for force sensor based on NV diamond were developed. Two optimized strategies for constructing Y-shape force sensors (Y-shape L and Y-shape S) were applied on NV diamond surfaces. MC3T3 cells adhered on the two types of Y-shape force sensors by RGD-integrin interaction. In the first three parts of relaxation measurements, the constructions were not stable due to the instability of silica layer. There were not enough RGD on the surfaces, and the cells did not spread very well. In the final relaxation measurements, silica layer was improved and cells spread better. In all measurements involving cells, the increase of T1 value induced by cell traction force could be detected under cell region. This demonstrated effective extension of immobilized PEG chains under traction force and the Gd^{3+}-NV induced signal was detectable in cell culture condition. All these results

revealed the possibility to employ Y-shape force sensor based on NV diamond as a tool for cell adhesion study, although lots of parameters were still need to be optimized and improved for high quality results.

6.2 Part II Effect of surface immobilized E-cadherin mimetic HAV peptide on MDCK cell adhesion

In an organized multicellular structure, cells adhere either by attachment to extracellular matrix (cell-ECM adhesion) or to other cells (cell-cell adhesion). Cell adhesion plays important role in tissue architecture and morphogenesis. The establishment and dissolution of the attachments regulate cell behavior by a complicate crosslinked signaling network. Cell-cell adhesions are mainly mediated by cadherin superfamily, a type of transmembrane cell adhesion molecules. To guide the design of new cadherin-based biomaterials, it is important to study how immobilized cadherin at the cell-material interface affects the adhesion of cells. It is especially interesting to understand the coordination of cadherin-mediated and integrin-mediated adhesion. The immobilization of cadherin on material surfaces decouples cadherin from other kinds of adhesion proteins and allows the observation of the cadherin-mediated adhesion isolated from other complex cell behaviors.[76, 109, 150]

Past fundamental studies on this topic have mainly focused on cadherin proteins rather than mimetic peptides. However, proteins can be easily denatured and lose their activity during the fabrication process of biomaterials. In addition, their high-precision functionalization with active chemical groups remains difficult. Protein mimetic peptides are wildly utilized as protein substitutes in materials science due to their high stability, simple synthesis, precise chemical structure, relatively low cost, and ease-of-use. Cadherin mimetic peptides mimic only the core amino acid sequence for cadherin-cadherin binding.[151-152] As reported previously, the fragment of E-cadherin containing the first and second outmost extracellular (EC) domains yields single cadherin-cadherin adhesion forces, whereas a construct containing all five EC

domains can promote cell spreading in the absence of integrin-based adhesion.[110] This shows that the efficiency of mimetic peptides is not usually equal to that of cadherin proteins. Thus, it remains necessary to specifically study the effects of surface immobilized cadherin mimetic peptides on cell adhesion.

Here, the E-cadherin mimetic peptide HAV was immobilized on a gold surface via cysteine residues and the adhesion of MDCK (Madin-Darby Canine Kidney) cells was studies. MDCK cells are a model for epithelial cells on the generated model surfaces as ***figure 6.2.1*** describes. The immobilized HAV peptide was proven to specifically interact with MDCK cells via E-cadherin and to assist integrin-based cell adhesion. The mechanical effects of this interaction were detected by traction force microscopy (TFM). Furthermore, the immobilized peptides mediated cell-cell interactions in cell clusters and caused a solid-to-liquid phase transition. The HAV peptide-MDCK interaction affects both the E-cadherin/β-catenin signaling pathway as well as E-cadherin-mediated cell adherens junctions. The expression of E-cadherin and β-catenin in the HAV peptide-activated cells was monitored by Western blot. Overall, our study exhibits an overview of the interactions between E-cadherin mimetic peptide and epithelial cells.

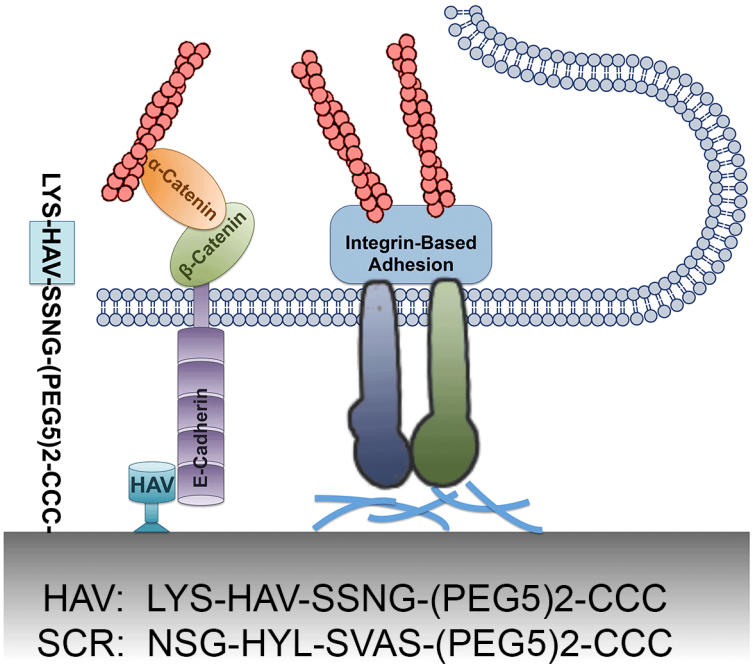

Figure 6.2.1 Immobilized E-cadherin mimetic peptide HAV on the substrate surface affects the adhesion of MDCK epithelial cells.

6.2.1 Specific interaction between HAV peptide and E-cadherin

E-cadherin contains an extracellular (EC) domain that consists of five tandem repeat subdomains (EC-1 to EC-5). The tripeptide His-Ala-Val (HAV) sequence, which is located in the first extracellular (EC-1) subdomain, has its unique importance in mediating homophilic cadherin-cadherin interaction.[152] To recreate this functionality, a LYS-HAV-SSNG-(PEG5)2-CCC (HAV) peptide sequence[151] was designed which mimics the EC-1 domain of E-cadherin. The sequence contains a cysteine anchor domain on the one end, which can be utilized to immobilize the sequence onto a substrate surface by way of an Au-thiol reaction. On the other end of the peptide, the active domain is expected to specifically interact with E-cadherin. For comparison, a scrambled peptide NSG-HYL-SVAS-(PEG5)2-CCC (SCR), which contains the same

cysteine anchor domain, but an active domain that is not in its functional order was also designed.

To prove the specific binding affinity of the synthetic HAV peptide to E-cadherin, QCM-D Au Q-sensors were immobilized with either HAV or SCR peptides for adsorption studies. To this end, E-cadherin in a PBS solution containing calcium ions was loaded onto the Au sensors immobilized with either HAV or SCR peptides for 1.5 hours in a static modulus, followed by washing first with PBS buffer and then with surfactant Hellmanex, which is efficient in washing away non-specifically adsorbed E-cadherin. ***Figure 6.2.2 a*** and ***b*** show the E-cadherin adsorption on the Au sensors immobilized with either HAV or SCR. About 0.50 mg/cm^2 E-cadherin adsorbed on the HAV-immobilized surface after washing with PBS, 84% of which still remained after washing with 2% Hellmanex. In contrast, 0.14 mg/cm^2 E-cadherin adsorbed on the SCR- immobilized surface and only 50% remained after washing with Hellmanex. Non-specifically adsorbed E-cadherin amounted to 0.08 mg/cm^2 and 0.07 mg/cm^2 on HAV and SCR surfaces, respectively. The amount of non-specifically adsorbed E-cadherin was similar on both surfaces, but the specific binding affinity on HAV was 6 times greater than on SCR.

To further confirm the specific binding of the HAV peptide to E-cadherin on the membrane of living cells, incubation experiments were carried out. First, a MDCK cell monolayer was prepared on a fibronectin-coated plate, which was then treated with EGTA to perturb the E-cadherin induced cell-cell contact by way of Ca^{2+} removal. HAV and SCR peptides were added into two separate wells of cell medium. A MDCK monolayer incubated without any peptide was used as the control. As shown in ***figure 6.2.3***, the cell-cell contacts in all three samples were still in a loosened state 30 minutes after the peptides had been added. After 2 hours both the

cell monolayer incubated with the SCR peptide and the one incubated without peptide recovered to a compact polygonal structure. In contrast, the monolayer incubated with the HAV peptide did not recover because of the inhibitory effect of the HAV peptide. It proves that the HAV peptide is able to recognize and bind to E-cadherin, and thus perturbs cadherin homophilic interactions between cells.[152]

Immunostaining of cadherin adhesion-related proteins E-cadherin (magenta) and β-catenin (red) makes this perturbation of cell-cell contact clearly visible (***Figure 6.2.2 c***). MDCK cells spread well on the RGD-immobilized surface. Both E-cadherin and β-catenin clearly accumulated at the cell-cell interface in the samples treated with SCR peptide or left without peptides. This indicates strong cell-cell contacts. In contrast, four hours after adding HAV into the medium the accumulation of both E-cadherin and β-catenin had lessened at the interface, suggesting that the functional integrity of cell-cell contacts was affected. The HAV peptide in the medium permeated into the cell junctions between cells and specifically interacted with E-cadherin on the cell membrane. This suggests that HAV adsorbation to E-cadherin makes E-cadherin unavailable for interactions related to the establishment and maintenance of cell-cell contacts between adjacent cells, thereby negatively affecting the stability of cellular connections.

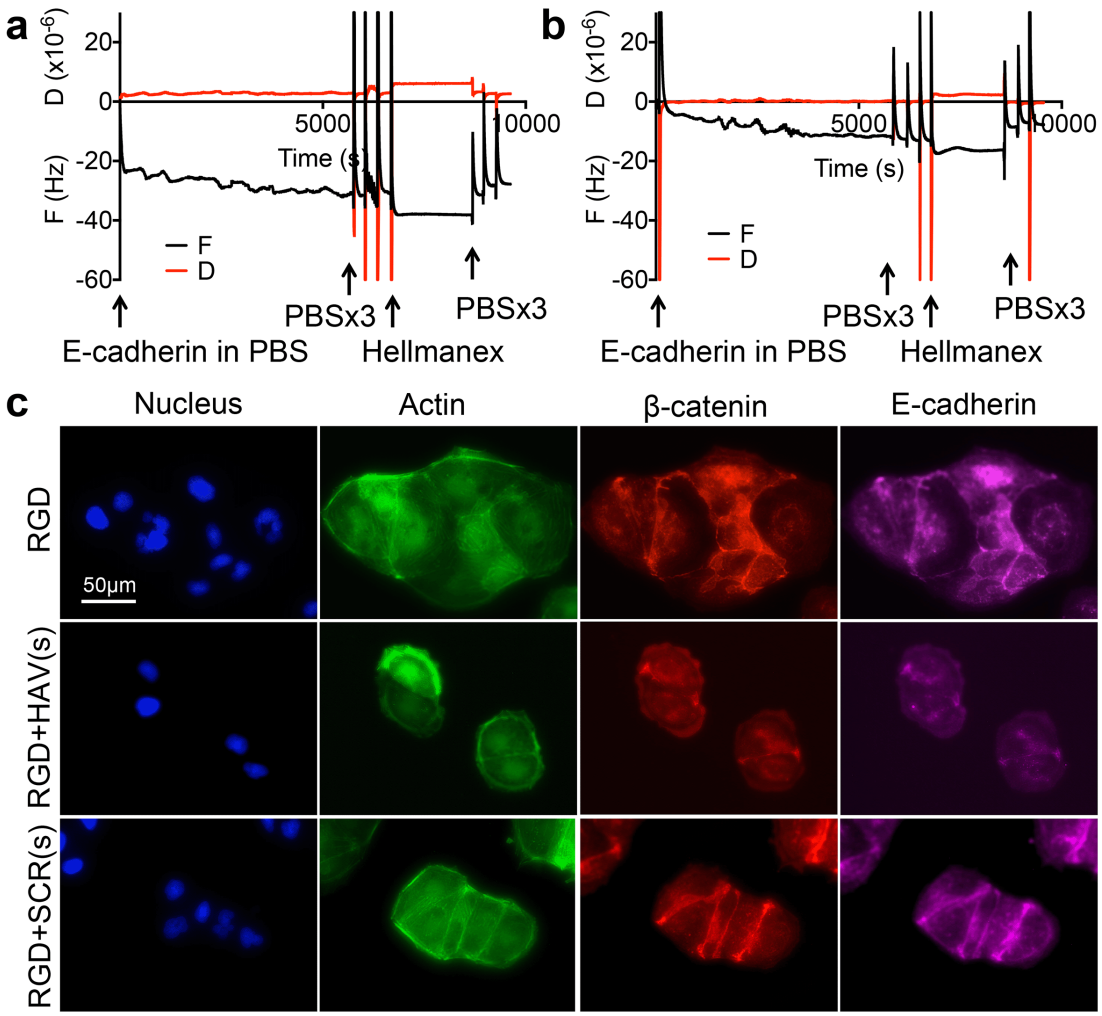

Figure 6.2.2 QCM frequency (F) and dissipation (D) shift as a function of time during the adsorption of E-cadherin on (a) HAV peptide and (b) SCR peptide functional sensor surfaces. (c) Representative immunofluorescence images of MDCK cells labeled for nucleus (DAPI, blue), actin (green), β-catenin (red), and E-cadherin (magenta) after culturing on RGD functional surfaces and incubation with HAV or SCR peptides [(s) stands for 'soluble' peptide in media] in solution for 24 hours.

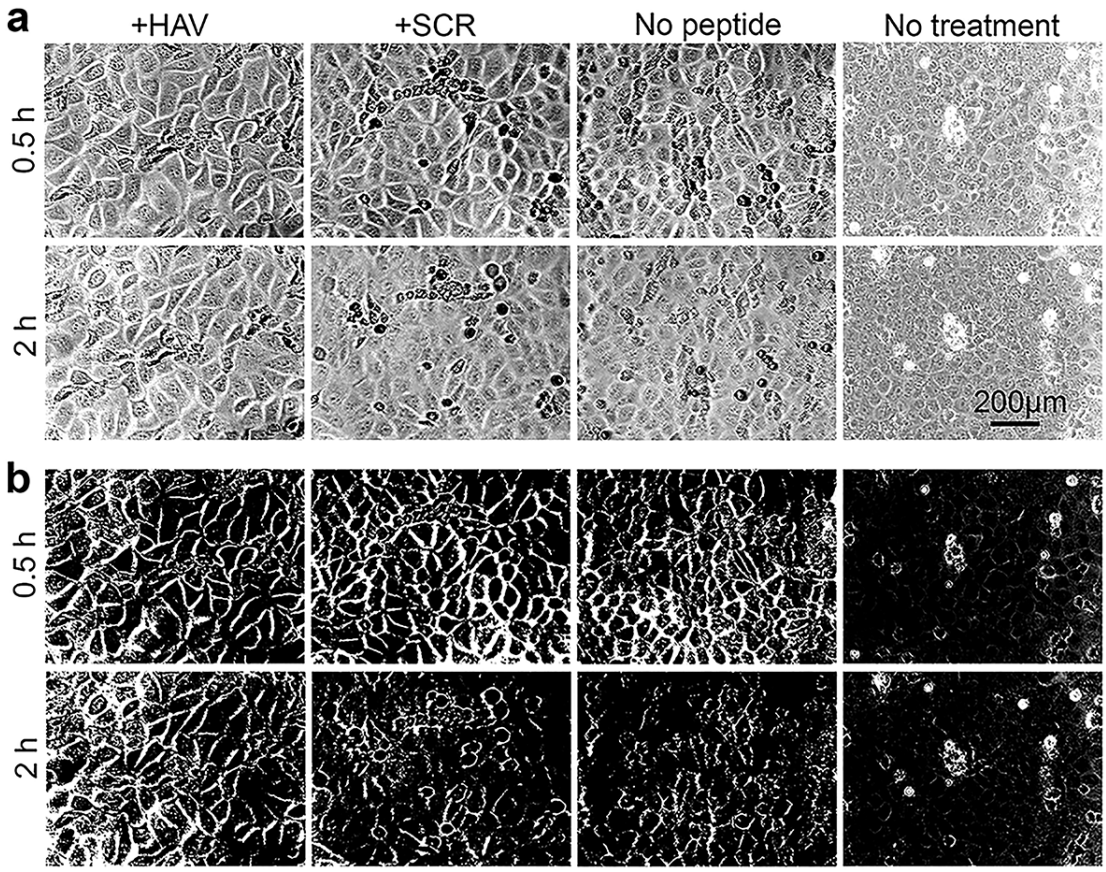

Figure 6.2.3 (a) Representative images of the recovery of cell-cell contacts. MDCK cell monolayers were incubated with HAV or SCR peptides, after cell-cell contact was interrupted by Ca^{2+} removal. In the "no treatment" group Ca^{2+} was not removed and no additional peptide was added. (b) Contrast enhancement of the images in (a).

6.2.2 Cell adhesion on HAV functional surface

Cell adhesion on HAV, SCR as well as RGD peptide functional surfaces was studied employing both homogenous Au surfaces and AuNP-patterned surfaces. Peptides were immobilized onto Au through the cysteine anchor domain to form a self-assembled monolayer (SAM). Peptide nanopatterns were fabricated using BCMN technology to achieve quasi-hexagonal AuNP patterns with an interligand spacing ranging from 12 to 112 nm. The SEM images of AuNPs are shown in ***figure 6.2.4***.

The size of each gold nanoparticle was less than 10 nm in order to restrict interaction to only a single E-cadherin (diameter of about 12 nm[153]). The advantage of utilizing patterned surfaces is to precisely control the density of the immobilized ligands.[154]

MDCK cells were then cultured on these surfaces in DMEM medium containing 10% FBS. Non-specific adsorption of FBS on surfaces exhibiting the HAV or the SCR peptide was evaluated by QCM-D as shown in ***figure 6.2.5***. The amount of adsorbed FBS on the HAV and the SCR SAM-coated Au sensors was 0.2301 and 0.2832 mg/cm^2, respectively. The adsorption on the bare Au sensor, in contrast, was 1.1328 mg/cm^2. This suggests that both the HAV and SCR peptide for the most part are able to counteract FBS adsorption, thereby successfully avoiding 'protein corona' formation and maintaining the activity of the peptides.[155-156] The small amount of adsorbed proteins can assist the adhesion of cells onto the peptide SAM.

The spreading of MDCK cells on different peptide functional surfaces after 4 hours of culture is shown in ***Figures 6.2.6 a*** and ***b***. The spreading area of cells was significantly larger on the HAV-functional Au surface compared to the SCR-functional Au surface. This difference was less significant on nanopatterned surfaces, where peptide density – and in turn the effects of peptide-induced adhesion – are decreased. HAV-induced adhesion differs from RGD-induced adhesion, which is reflected in the cell spreading area and morphology. MDCK cells were more elongated with smaller lamellipodia on HAV functional surfaces compared to more round cells with a larger lamellipodia area on the RGD functional surfaces. This is due to the fact that RGD directly activates integrins, which facilitates cell-ECM adhesion rather than the establishment of cell-cell junctions.

Next, we investigated the effects of HAV peptide density on cell adhesion in greater detail. As indicated in ***figure 6.2.6 c*** and ***d***, the spreading area of cells decreased with

a linear tendency as the spacing of AuNPs increased from 12 nm to 112 nm (and the amount of immobilized HAV peptide decreased). This lies in contrast to how RGD-induced adhesion changes as a reaction to modifications in interligand spacing.[114, 157] RGD-induced adhesion responds to a change in interligand spacing in an on/off behavior, which can be attributed to force loading.[158] In our experiments cells did not spread well on RGD functional AuNP-patterned surfaces with an interligand spacing of 112 nm. However, cell spreading was comparable on the RGD functional homogeneous surface and the nanopatterned surface at an interligand spacing of 12 nm (***figure 6.2.6 a***)**,** which is in accordance with previous studies.[114, 157-158] Cadherin-cadherin interaction in cadherin clusters has been described by an "adhesion zipper" model.[45] Accordingly, the decreased HAV density on the nanopatterned surfaces may simply lead to a decreased number of zipper-like structures and insufficient E-cadherin clustering.

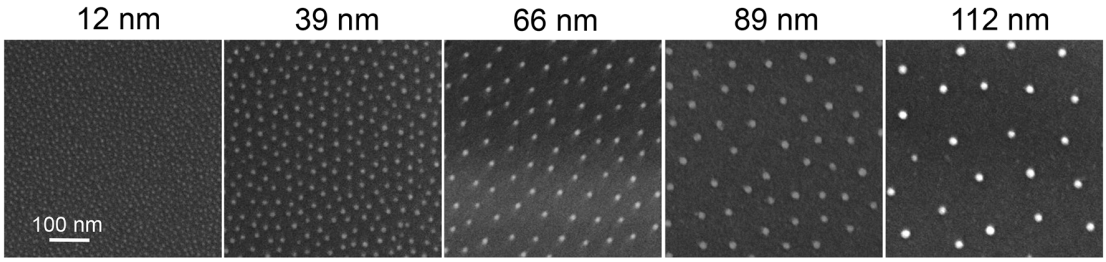

Figure 6.2.4 Representative SEM images of quasi-hexagonal AuNP patterns with interligand spacings ranging from 12 to 112 nm on glass.

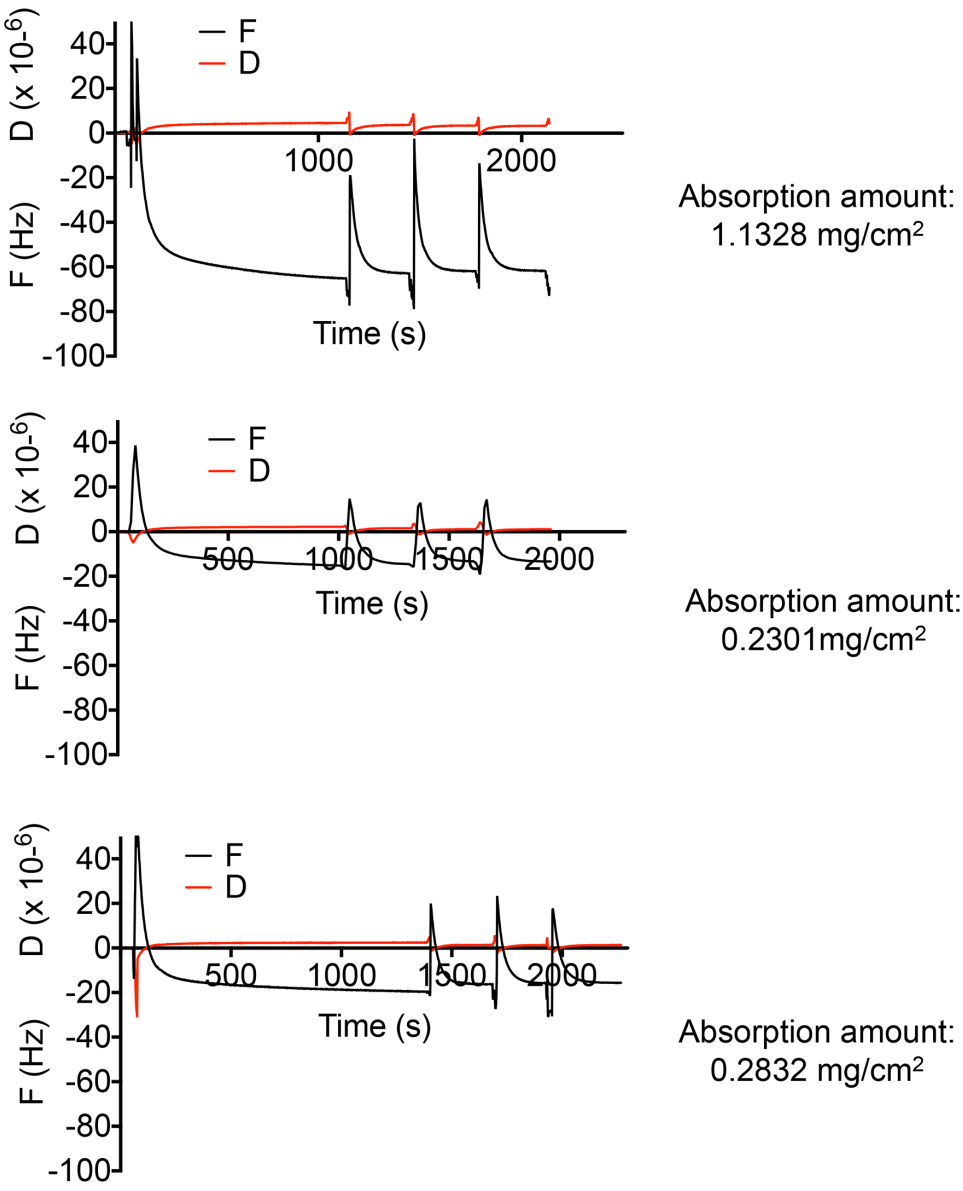

Figure 6.2.5 QCM frequency (F) and dissipation (D) shift as a function of time during the adsorption of FBS on bare (top image), HAV peptide functional (middle), and SCR peptide functional (bottom) Au sensor surfaces.

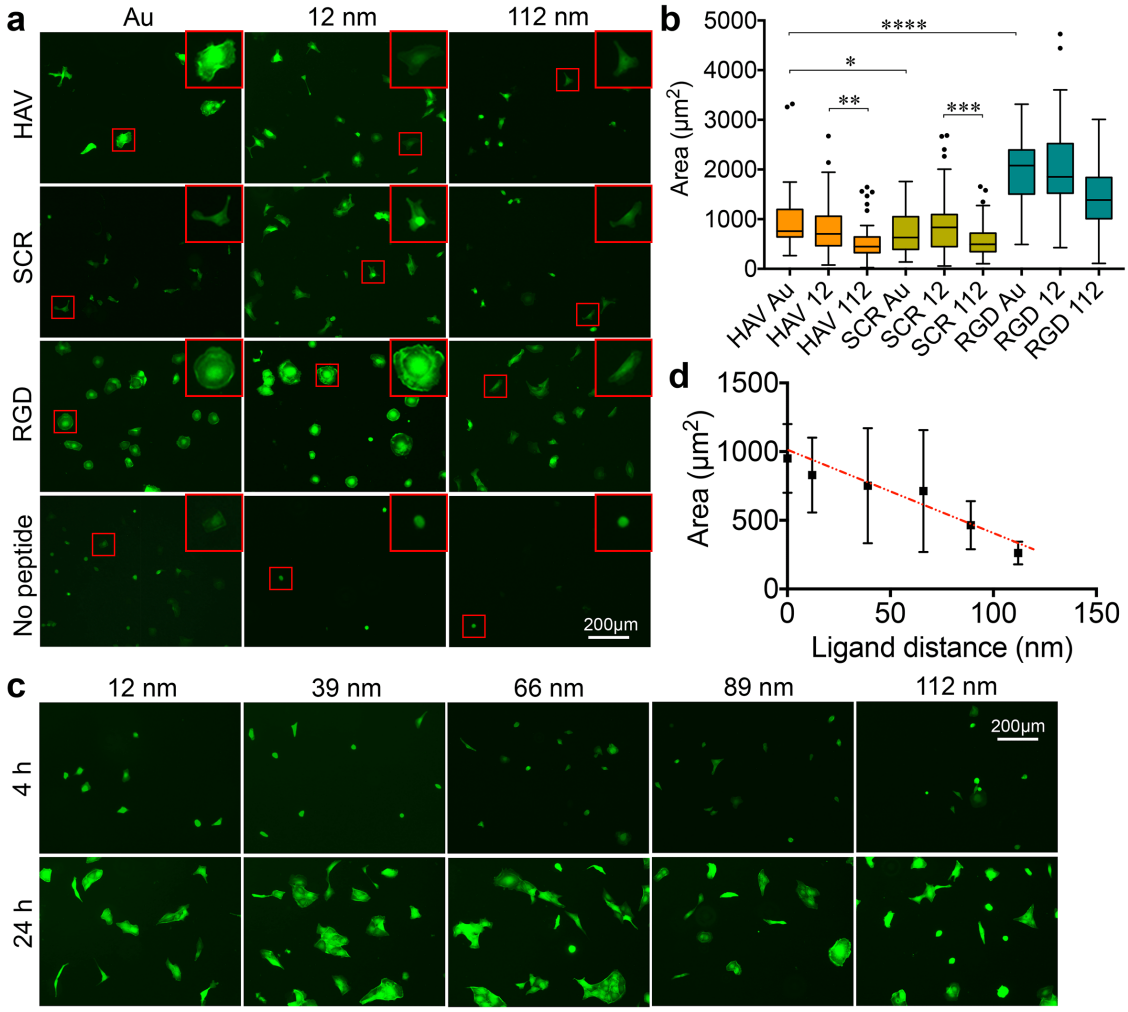

Figure 6.2.6 (a) Representative fluorescence images of MDCK cells cultured on different surfaces for 4 hours. Inserts show a zoom of the region denoted by the smaller red square. (b) Quantification of the spreading area of MDCK cells cultured on homogeneous Au or nanopatterned surfaces (with either 12 nm or 112 nm interligand spacing) and immobilized with either HAV or SCR peptides for 4 hours (n = 50, 3 technical replicates). (c) Representative fluorescence images of MDCK cells cultured for 4 or 24 hours on nanopatterned surfaces differing in interligand spacing. (d) Quantification of the spreading area of MDCK cells cultured for 4 hours on nanopatterned surfaces differing in interligand spacing (n = 50, 3 technical replicates).

6.2.3 Cell clustering on HAV functional surface

During regular growth, epithelial cells form tight clusters by way of adherens junction. When epithelial cells sense scatter factors secreted by mesenchymal cells, however, these clusters can decompose by breaking cell-cell contacts.[159] The separated single cells then become elongated and motile, which plays an important role in tissue remodeling and wound healing. Therefore, we studied the cell-cell contact of each single MDCK cell on a HAV peptide functional surface. The cell detachment ratio of cells, an indicator of cell clustering behavior, was defined as the count of all cell separation times divided by the count of all cell contact times in the same time period in time-lapse images. As shown in ***figure 6.2.7 b***, cells on HAV functional surfaces exhibited a relatively high cell detachment ratio. ***Figure 6.2.7 a*** depicts a typical time-lapse image of two single cells in contact and then separated on a HAV surface. Cells were in contact with each other but failed to form stable clusters, in other words, they remained elongated and then separated from each other only after a short contact time. When the density of immobilized HAV peptide was decreased, as is the case on the nanopatterned surfaces, cells exhibited an increased cell detachment ratio. However, this is mostly because the weak cell-substrate adhesion resulted in a high mobility of the cells (***figure 6.2.7 c***). High mobility, in turn, caused unstable cell-cell contacts. Due to the weakened cell-substrate interactions, the cells on homogenous SCR functional surfaces and on nanopatterned Au surfaces with 12 nm interligand spacing exhibited higher mobility than cells on comparable HAV functional surfaces. However, the cell detachment ratio of cells on both homogenous and nanopatterned SCR surfaces was overall lower than that of cells on related HAV surfaces. This is because HAV – by binding to E-cadherin – interrupted cadherin-cadherin interactions in adherens junctions, thus weakening cell-

cell contacts. As a result, cells on the HAV surface had less resistance against cell separation. However, when the interligand distance on the nanopatterned substrate reached a value of 112 nm, the effects of increased cell mobility overrode the interruptive effects of HAV on cadherin-cadherin interactions. As a result, there was no significant difference in the cell detachment ratio of cells on SCR and HAV surfaces at an interligand spacing of 112 nm (***figure 6.2.7 b***). Cells on RGD functional surfaces exhibited the lowest cell detachment ratio. At a high grafting density of RGD peptides on the homogenous Au surface, the cell detachment ratio is almost 0. And, since these cells spread very well and had little mobility, adherens junctions were not disturbed. These results prove that immobilized HAV interacts with E-cadherin on the cell membrane. This disturbance causes the replacement of E-cadherin-based cell-cell interactions by HAV-cell binding. As a result, cell-cell contact is weakened and cells separate from each other.

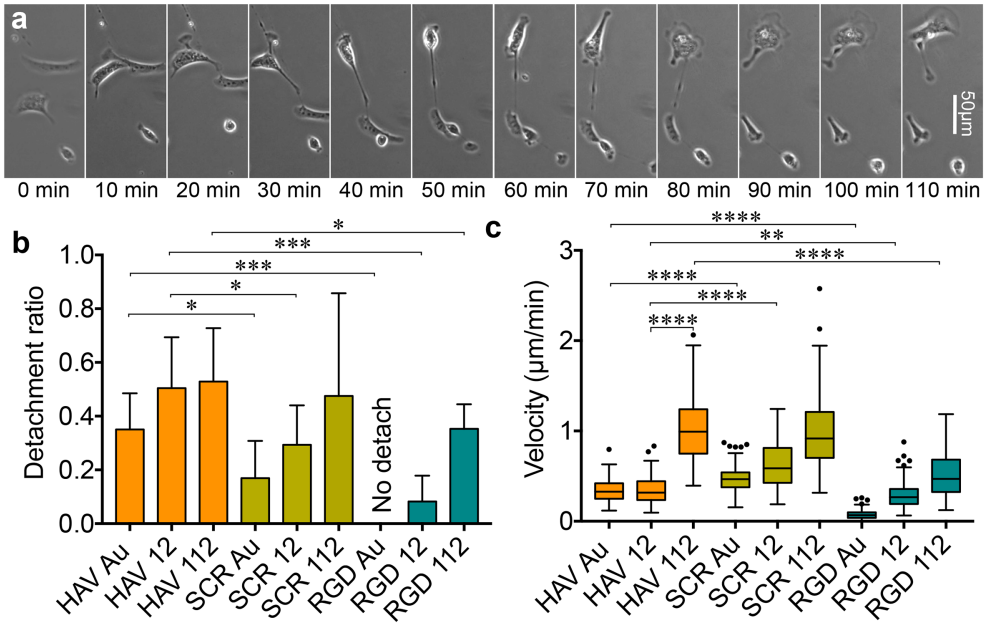

Figure 6.2.7 (a) Representative time-lapse images of cell-cell interactions of MDCK cells on HAV peptide functional surface. (b) The cell detachment ratio and (c) the velocity of the MDCK cells on homogeneous Au or nanopatterned surfaces (with either 12 nm or 112 nm interligand spacing) and immobilized with either HAV or SCR peptides during an observation time window from 4 to 24 hours during the cell culture period (n = 10, 3 technical replicates).

6.2.4 Cell adhesion on RGD and HAV peptide co-functional surfaces

In the experiments described above some of the FBS proteins were non-specifically adsorbed on the HAV functional surfaces. In order to eliminate the effect of non-specific interactions, RGD and HAV peptides were co-immobilized on Au surfaces, and a medium with a reduced serum amount was used for MDCK cell behavior studies. MDCK cell adhesion and mobility were affected by the ratio of surface-immobilized RGD and HAV peptides as shown in ***figure 6.2.8***. Lower amounts of RGDs resulted in insufficient cell adhesion, whereas higher amounts of RGD masked HAV-induced interactions. Because RGD selectively binds to integrin receptors, the RGD-sequence is crucial for cell adhesion. A mixing ratio of 1:400 RGD to HAV peptides was decided for further studies. At this ratio, cells maintained both their adhesion and mobility properties.

Figure 6.2.9 a showed typical phase contrast images of MDCK cell adhesion on a RGD and HAV peptide co-functional surface (RH) as well as images of MDCK cell adhesion on a RGD and SCR peptide co-functional surface (RS) at different time points. Cell spreading differed significantly especially early on during adhesion, as

the 6-hour time point illustrates (***figure 6.2.9 d***). The formation of focal adhesion points was observed only on cells adhering to the RH surface but not to cells on the RS surface (***figure 6.2.9 c***). Later during adhesion the difference in spreading between the cells on RH and RS surfaces became smaller but remained visible, as is indicated at the 24-hours time point (***figure 6.2.9 a***). After adding free HAV peptide into the medium, the spreading area of cells on the RH surface dramatically decreased and became comparable to the spreading of cells on the RS surface. Conversely, adding free SCR peptide into the medium had only little effect on the spreading area of cells on the RH surface, which decreased a little bit but still remained significantly different to spreading on the RS surface (***figure 6.2.9 b*** *and* ***d***). This demonstrates that the added HAV peptide in the medium obviously functioned as a competitor to the SCR peptide. HAV in the medium specifically interacts with E-cadherin on the cell membrane, thereby decreasing the chance of E-cadherin interacting with immobilized HAV on the substrate. As a consequence, immobilized HAV played less of a part in cell adhesion and its impact was reduced. These results further confirm that immobilized HAV assists integrin-based cell adhesion. Interestingly, free HAV peptide did not change the spreading behavior of the cells adhering to the RS surface. Only immobilized HAV peptide was able to improve cell spreading. This indicates that HAV-induced cell adhesion is related to cellular mechanosensing and probably mechanotransduction. Thus only immobilized HAV was able to generate enough force to induce E-cadherin related signaling.

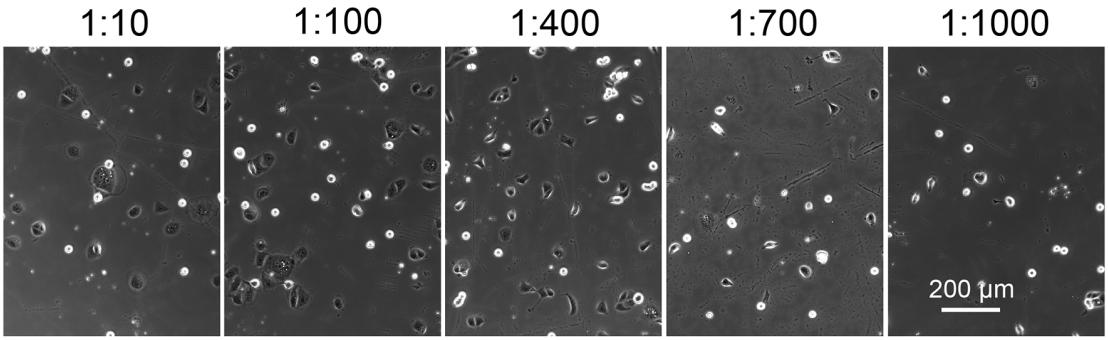

Figure 6.2.8 Representative images of MDCK cells adhering to surfaces functionalized by RGD and HAV peptides at different mixing ratio (RGD:HAV) after 6 hours of culture.

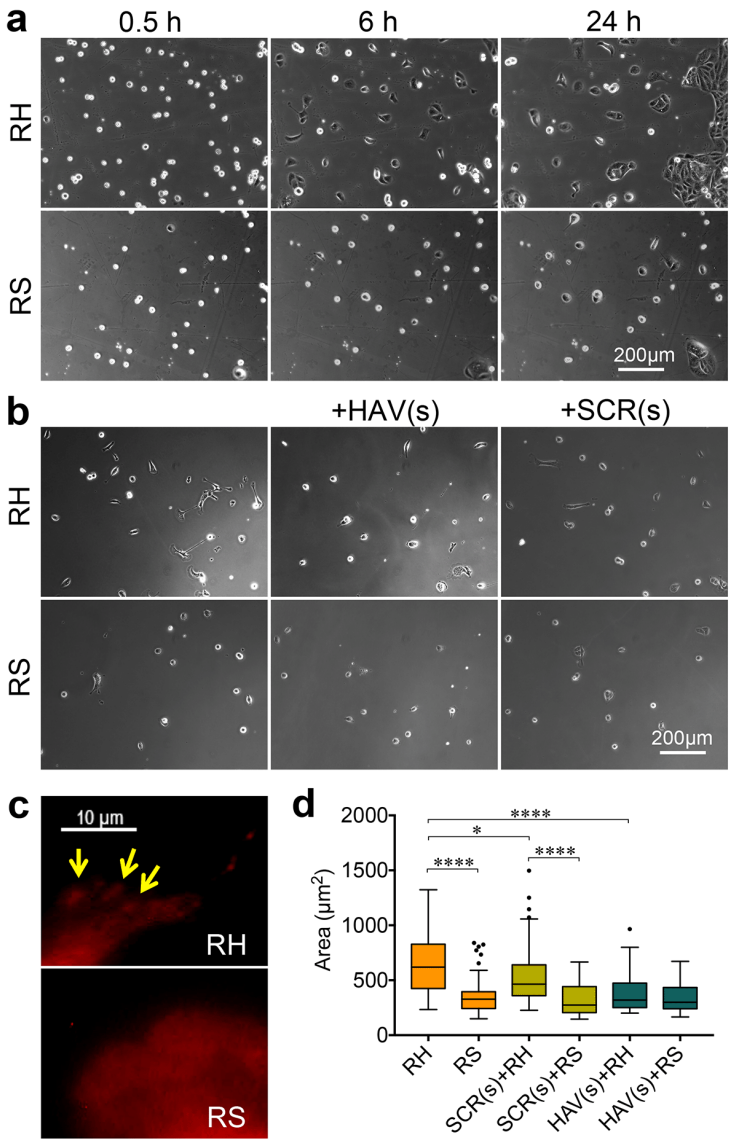

Figure 6.2.9 Representative images of MDCK cell adhesion on RH and RS surfaces. (a) Cellular adhesion at different time points; (b) adhesion at 6 hours after the addition of free HAV or SCR peptides [(s) stands for 'soluble' peptide in media]; (c) representative fluorescent immunofluorescence images of MDCK cells stained with anti-vinculin after 4 hours of growth on RH and RS surfaces. Arrows indicate focal adhesion points. (d) The spreading area of MDCK cells cultured in different conditions for 6 hours (n = 50, 3 technical replicates).

To confirm the HAV-induced cell adhesion is related to cell mechanotransduction, myosin II inhibitor blebbistatin was utilized to treat the MDCK cells. The formation of actomyosin stress fibers is one of the key steps in mechanotransduction. Blebbistatin can interfere stress fiber formation by decreasing myosin II activity to block mechanotransduction.[160] As the results, the spreading area of cells on the RH surface was efficiently inhibited and decreased to the same level as cells on the RS surface (***figure 6.2.10 a*** and ***b***). Thus the HAV-induced cell adhesion requires the intracellular tension, which can initiate mechanotransduction pathways.

The intracellular tension of the single cells is linked with cellular adhesion force. We further measured the force on peptide-immobilized surfaces by traction force microscopy employing beads embedded in PAAm hydrogels. The cell traction force-induced displacement of fluorescent microbeads was recorded by taking microscopy images of microbead relocation during cell spreading. As shown in ***figure 6.2.10 c***, the traction force of a cell on a RH surface was dramatically higher than that on a RS surface. ***Figure 6.2.10 d*** depicts the frequency distribution of the traction forces generated by one cell. Among the force curves detected on the RS surface a high frequency was observed at a low force of ~20 Pascal. On the RH surface, in

comparison, there was a higher frequency at a larger traction force. This corresponds with the results obtained from mean traction force measurement on different single cells shown in ***figure 6.2.10 e***. The mean traction force on the RH surface was 47.74 Pa compared to only 26.46 Pa on the RS surface. The traction force microscopy results reveal that the specific interaction of immobilized HAV peptide enhances both the cell adhesion force and mechanosensing. As mechanosensing is critical for cell adhesion,[161] it explains the means by which HAV functional surfaces increase cell spreading.

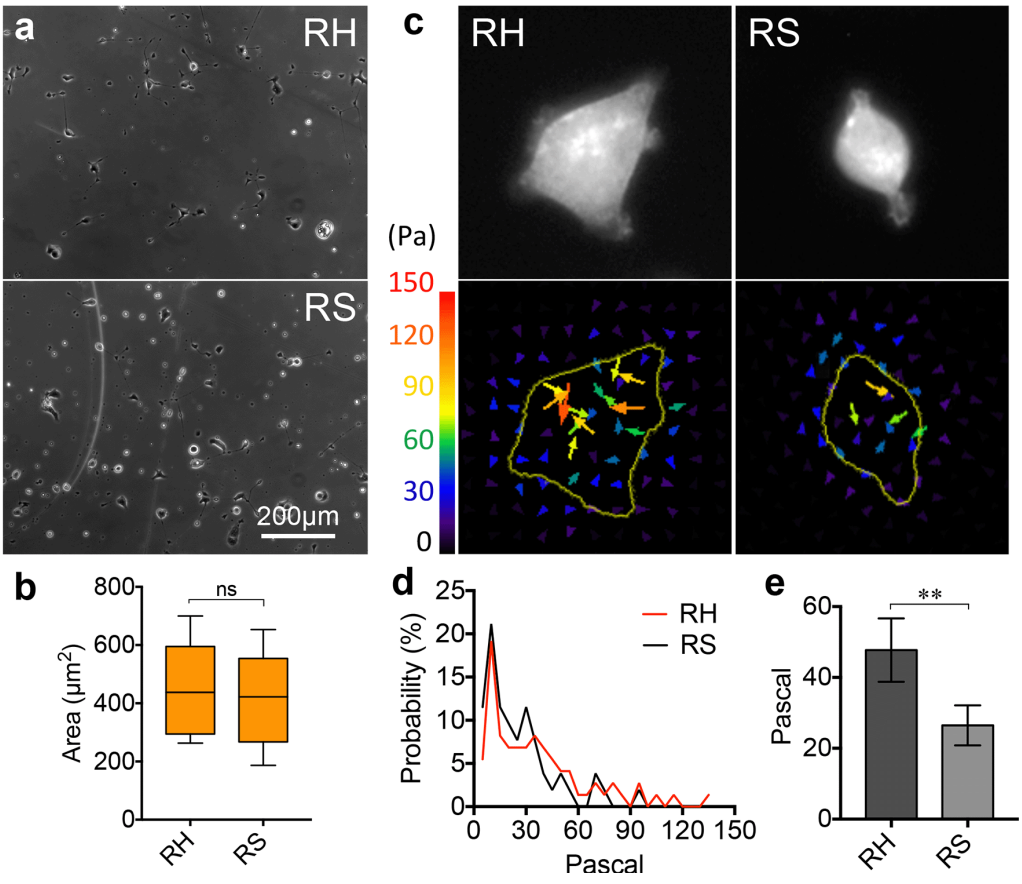

Figure 6.2.10 (a) Representative images and (b) the spreading area of MDCK cells treated with blebbistatin for 6 hours on RH and RS surfaces (n = 50, 3 technical replicates). (c) Representative fluorescence images of single MDCK cells adhering to RH (left) and RS (right) functional PAAm hydrogels with embedded fluorescent microbeads (top two images) and the traction fields of the related cells (bottom two images). (d) Frequency distribution of the traction forces generated by a single cell on RH and RS surfaces. (e) Mean traction force of different single cells on RH and RS surfaces (n = 10, 2 technical replicates).

6.2.5 Cell clustering on RGD and HAV peptide co-functional surfaces

Co-immobilizing HAV and RGD on the peptide functional surfaces affected cell-cell contacts. ***Figure 6.2.11*** shows the accumulation of adherens junction proteins E-cadherin and β-catenin at the cell-cell interface made visible by immunofluorescence. The intensity of both E-cadherin and β-catenin at the cell-cell interface in cell clusters was dramatically weaker on the RH surface than on the RS surface. This is a sign of weaker cell-cell contacts on the RH surface and explains the high cell detachment ratio on HAV functional surfaces. Moreover, we analyzed detachment ratio and velocity of MDCK cells on RH and RS surfaces. Similar to the results shown in section 3.3, the velocity of cells on the RS surface was significantly higher than on the RH surface (***figure 6.2.12 b***), which results in a greater likelihood for cells to separate from each other on the RS surface. However, the cell detachment ratio of cells was dramatically higher on the RH surface than on the RS surface (***figure 6.2.12 a***). This

is in line with the results obtained in the experiments looking at cell adhesion in the presence of FBS (***figure 6.2.7 b***).

We further investigated collective cell behavior in cell clusters. As shown previously, a cellular collective organized in a confluent cluster can either jam together to achieve a solid-like state or instead unjam and flow in a fluid-like state.[162] According to a model representing epithelial layer dynamics each cell is associated with the tension from its neighboring cells and the force between cells is balanced at each vertex, where cell-cell junctions meet.[163] Based on this vertex model, the single cell shape index can be utilized to analyze the solid- and fluid-like states.[164]

In our study, the shape of the MDCK cells in clusters was quantified by circularity analysis (***figure 6.2.12 c***). The cells on the RH surface exhibited smaller circularity, i.e., they were less circular than cells on the RS surface (***figure 6.2.12 d***). Cell clusters on the RH surface were more fluid-like compared to the more solid-like cell clusters on the RS surface. When surface-immobilized HAV peptide interfered in E-cadherin adherens junctions resulting in weakened cell-cell contacts, the cells in the clusters became more independent. They failed to cluster together tightly enough to develop an elastic restoring force sufficient for maintaining the initial shape.[162] This resulted in fluid-like cell clusters on the RH surfaces. Similarly, the removal of Ca^{2+} from a confluent cell monolayer, an act that destroys cell-cell contacts, also leads to a decrease in the circularity of single cells and a more fluid-like monolayer (***figure 6.2.13***). The cell monolayer returned to a more solid state when Ca^{2+} levels were restored.

To investigate the 'jamming' of cells in confluent monolayers, the migration velocity of each cell was calculated using time-lapse imaging. Interestingly, in contrast to the results obtained for single cells (***figure 6.2.12 b***), the velocity of cells

in monolayers on RH surfaces was significantly higher than on RS surfaces (***figure 6.2.14 a***). The migration speed in monolayers (0.8 and 0.7 μm/min on RH and RS, respectively) was higher than in a single cell state (0.3 and 0.5 μm/min on RH and RS, respectively). This migration must be driven by the tension generated by cell sheets in addition to the mobility of the single cell. ***Figure 6.2.14 b*** shows the migration of representative cells on RH and RS surfaces. Besides differences in the length of trajectories, a constant change of neighboring cells could be observed. The number of shifting neighbors was greater on RH surfaces. This confirms that cells were more active to propel and intercalate in fluid-like clusters.[165] These results once again prove that surface-immobilized HAV peptides decrease cell-cell contacts and cause a solid-to-liquid transition of cell clusters.

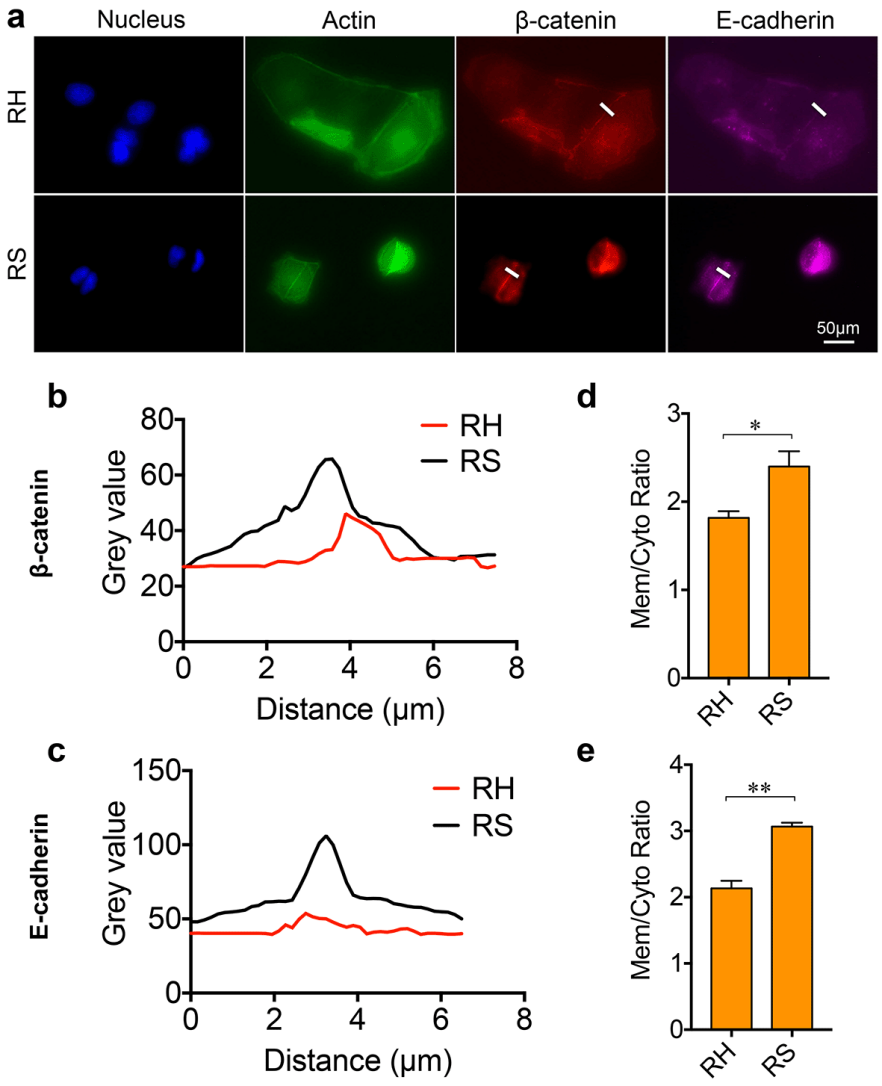

Figure 6.2.11 (a) Representative immunofluorescence images of MDCK cells labeled for nucleus (DAPI, blue), actin (green), β-catenin (red), and E-cadherin (magenta) after 24 hours of culture on RH and RS surfaces. (b,c) The fluorescence intensity profile of anti-β-catenin and anti-E-cadherin at the positions indicated by a short white line in the images in (a). (d,e) The membrane-to-cytoplasm ratios of the fluorescence intensity of anti-β-catenin and anti-E-cadherin (n = 30, 2 technical replicates).

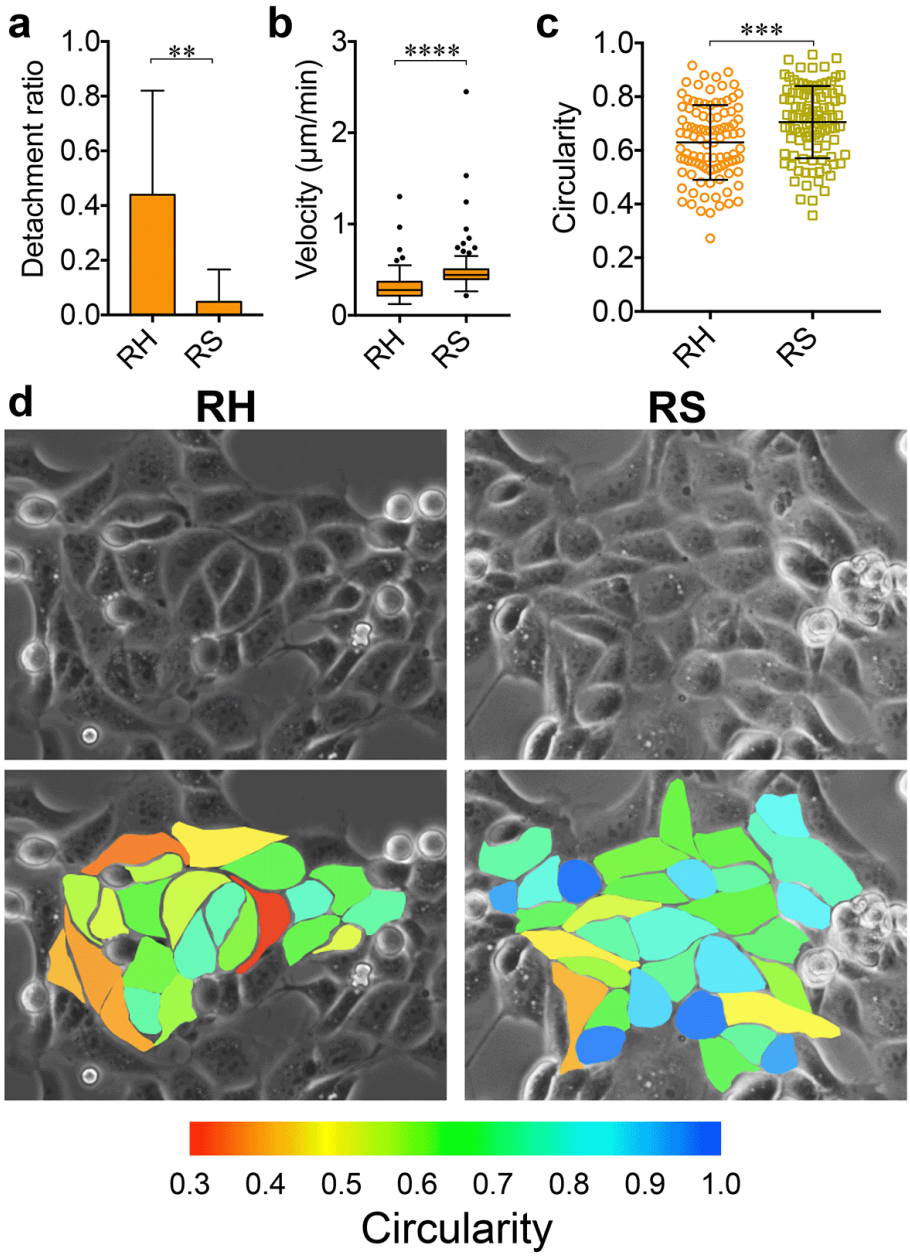

Figure 6.2.12 (a) The cell detachment ratio and (b) the velocity of MDCK cells on RH and RS surfaces during hours 4 to 24 of the cell culture (n = 10, 3 technical replicates). (c) Circularity of MDCK cells in clusters on RH and RS surfaces (n = 100). (d) Representative images (top two images) of MDCK cells in clusters on RH (left) and RS (right) surfaces and a circularity map (bottom two images) of the same cells.

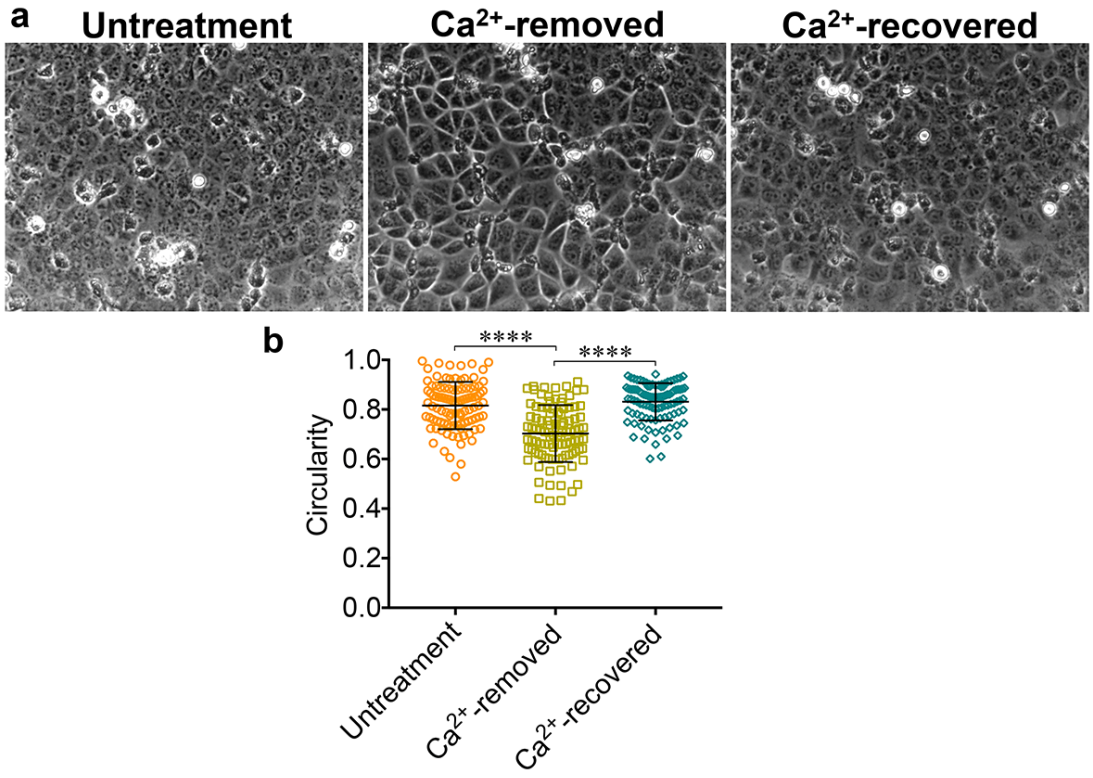

Figure 6.2.13 (a) Representative images of MDCK cell monolayers on fibronectin-coated glass (left), after Ca^{2+} was removed using EGTA (middle), and after recovery 2 hours later (right). (b) The circularity of MDCK cells in monolayers: untreated (orange), after Ca^{2+} removal (green) and after recovery (petrol blue) (n = 100).

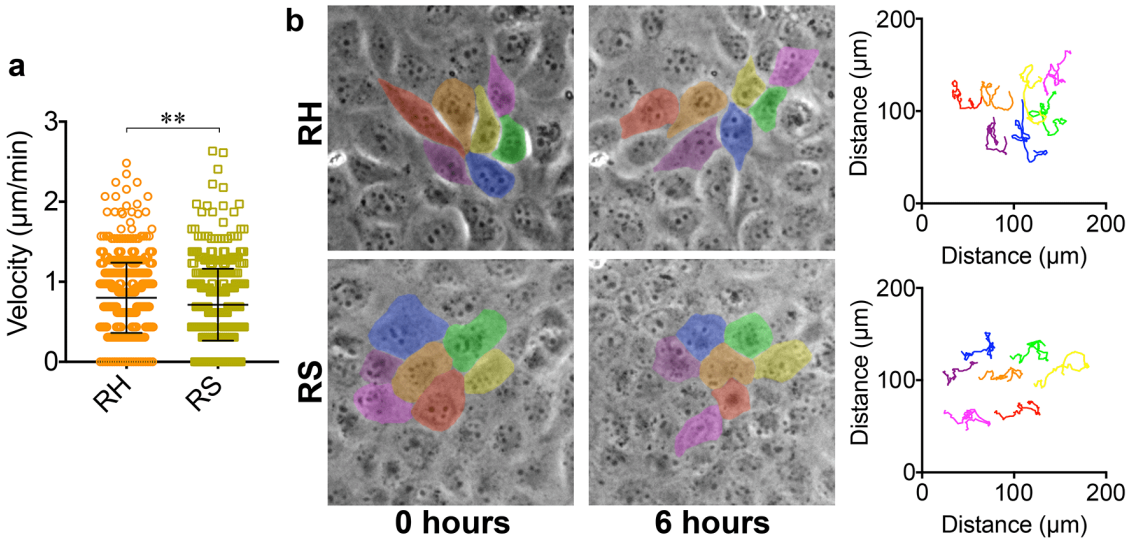

Figure 6.2.14 (a) The velocity of MDCK cells migrating in clusters on the RH and RS surfaces (n = 500). (b) Representative images of MDCK cells migrating in clusters on the RH (top two images) and RS (bottom two images) surfaces and the corresponding cell tracks (far right). Different colors indicate 7 different cells before and after migration.

6.2.6 Investigation of possible signaling pathway involvement

It has previously been shown and also proven in section 3.1 that the HAV peptide specifically binds to E-cadherin. As assumed in the cell adhesion studies above, immobilized HAV assisted cell spreading and mediated cell-surface contact through HAV-E-cadherin interaction. This interrupted E-cadherin-E-cadherin interplay and shifted cellular behavior from cell-cell to cell-materials interaction. By blocking E-cadherin on the cell membrane as well as analyzing the expression levels of related proteins, we wanted to confirm whether the immobilized HAV peptide really did regulate cell behaviors through HAV-E-cadherin interaction.

E-cadherin blocking antibody (DECMA-1) was used to block E-cadherin on the cell membrane (***figure 6.2.15***). As a result, the spreading of MDCK cells was largely inhibited on the RH surface. The spreading area decreased to a level comparable to cells on the RS surface. This indicates that the HAV peptide interacted with cells solely through E-cadherin. When E-cadherin was blocked by an antibody, HAV-mediated adhesion was entirely erased.

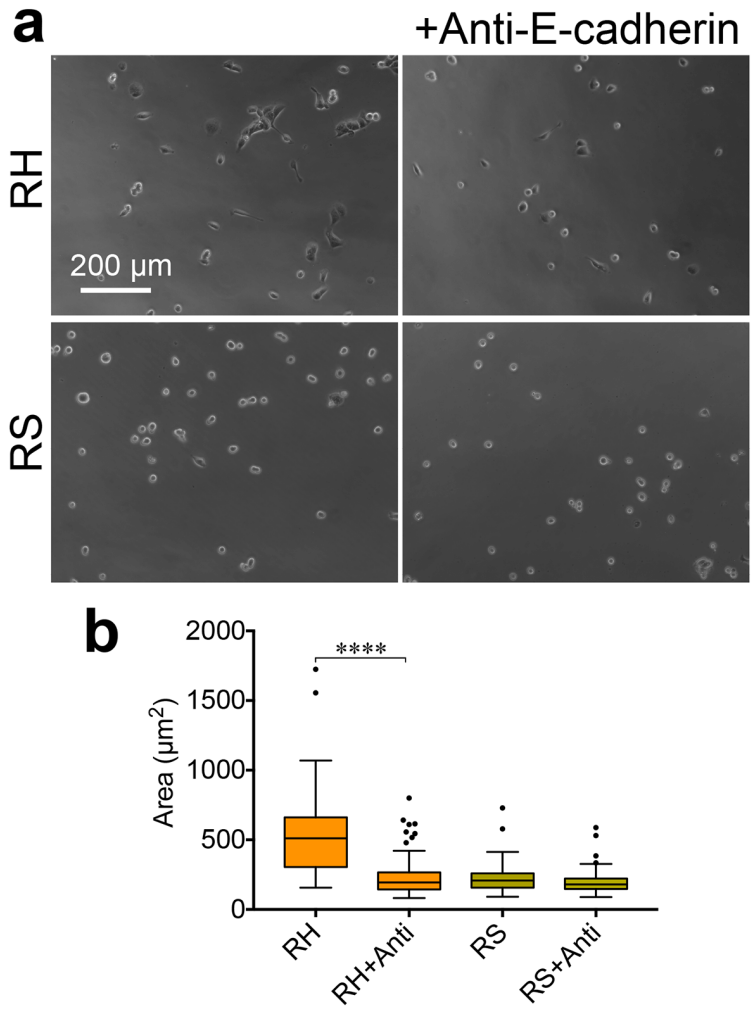

Figure 6.2.15 (a) Representative images of the adhesion of MDCK cells after 6 hours of culture on RH and RS surfaces in a medium containing anti-E-cadherin (b) The spreading area of the MDCK cells after 6 hours of culture on RH and RS surfaces in a medium containing anti-E-cadherin (n = 50, 3 technical replicates).

E-cadherin-induced adherens junctions induce specific intracellular signaling.[44] β-catenin plays an important role in connecting E-cadherin to the cytoskeleton and inducing downstream signaling pathways.[166] We therefore analyzed the expression level of both E-cadherin and β-catenin in the cells that adhered on the surface via HAV-induced adhesion. Only proteins from non-clustered cells were isolated for a Western Blot assay to exclude the effects of cell-cell attachment. As shown in ***figure 6.2.16 a-c***, the expression of both E-cadherin and β-catenin in the cells on the RH surface was significantly higher than on the RS surface. In addition, we investigated expression levels of β3-integrin and β1-integrin, two major integrin types that can be activated by RGD peptide.[106] As shown in ***figure 6.2.16 a, d, e***, expression did not differ significantly between the cells on the RH and RS surfaces. This indicates that the immobilized HAV peptide induces the expression of E-cadherin and β-catenin possibly by way of recruitment of E-cadherin at the interface between cells and materials. These results together confirm that the immobilized HAV peptide affects cell behaviors through the interaction with cell membrane E-cadherin.

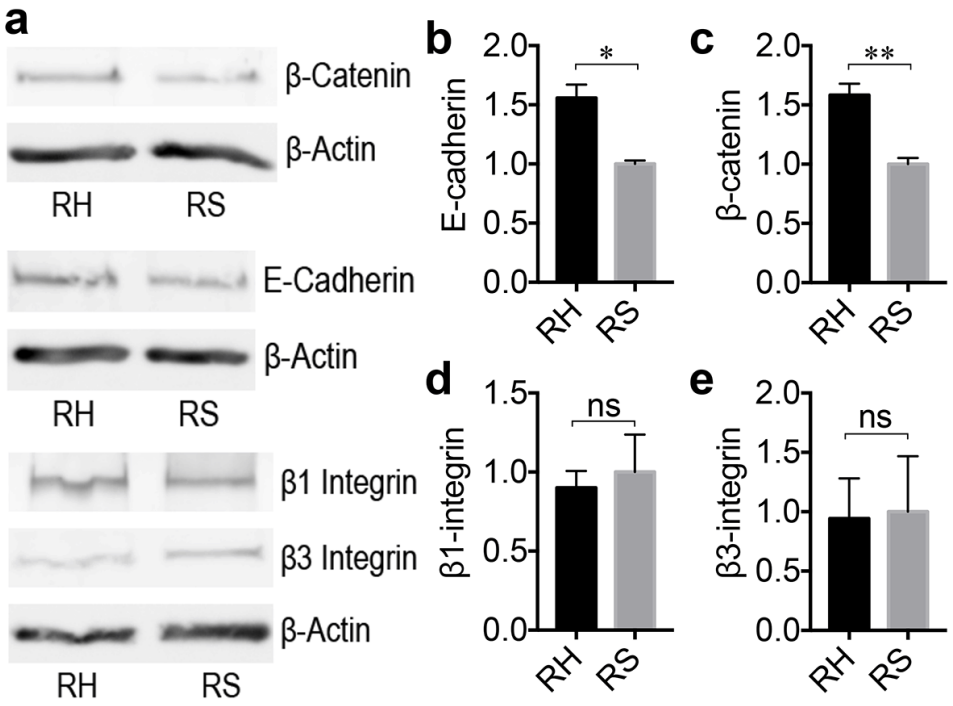

Figure 6.2.16 (a) Representative Western blot analysis of the expression level of β-catenin, E-cadherin, β1-integrin, and β3-integrin in MDCK cells cultured on RH and RS surfaces for 5 hours. (b-e) Quantification of the expression level of each protein based on Western blot images (n = 1-2, 2 technical replicates).

In this fundamental study we studied the effects of surface immobilized E-cadherin mimetic HAV peptide on epithelial cell behaviors, including adhesion and clustering. Surface immobilized HAV peptide specifically interacted with E-cadherin and induced the relocation of E-cadherin-based adhesion from adherens junctions at the cell-cell interface to HAV-E-cadherin binding at the cell-material interface. It enhanced cell adhesion on the material surface and weakened cell-cell contacts, which resulted in a solid-to-liquid phase transition of cell clusters. These effects can play an important role in epithelial wound healing. Moreover, the density of the immobilized peptide was important for achieving efficient adhesion by way of a zipper-like structure. We further demonstrated that HAV-E-cadherin interaction is related to cell

mechanosensing and enhances the expression of E-cadherin and the downstream signaling protein β-catenin. Within the past a few years, the demand for cadherin mimetic peptides for the design of synthetic biomaterials has rapidly increased. Our studies can help to understand the interactions between cells and such materials as well as to guide the design of new biomaterials.

7. Conclusion and Outlook

In this thesis, cell adhesions including cell-extracellular matrix (ECM) adhesion and cell-cell adhesion were studied via cell-ligand interactions. Integrin ligand RGD peptide and/or cadherin ligand HAV peptide were immobilized on 2D surfaces as a toolbox.

In part I, RGD peptide was co-immobilized with paramagnetic ion Gd^{3+} through PEG chains on nitrogen-vacancy (NV) diamond. A Y-shape molecule was designed on NV diamond as a force sensor. The stability and efficiency of the force sensors with different molecular structures were tested. Y-shape S, which contains Y-shape configuration and relatively short PEG chain on a 2 nm silica layer, was recognized as the optimized force sensor molecule. The cell adhesion force induced by integrin-RGD interaction was then detected and measured successfully. The traction force distribution was presented as relaxation time T1 map, which provided the potential to quantify the cell traction force in a high resolution. The results gave a straightforward impact on integrin-RGD interaction induced cell traction force distribution on the substrate within a single cell range. It can be helpful to understand the mechanisms of integrin-mediated cell adhesion and how cells respond to the extracellular mechanical stimulations. The NV centers in diamond render stable fluorescence, high sensitivity and spatial resolution. The RGD in the Y-shape molecule can be replaced by different peptide ligands. Therefore, the NV diamond based Y-shape force sensor may also be applied as a prospective toolbox to study different types of cell adhesion. However, there is still much space to improve the force sensor. For instance, more paramagnetic ions can be immobilized in one polymer, the distance between paramagnetic ions and NVs can be further shortened, in order to improve the sensitivity of the sensor.

In part II, E-cadherin mimetic HAV peptide was immobilized on gold surfaces, and how the immobilized HAV peptide affected adhesion and clustering of epithelia cell was studied. The results revealed that the surface immobilized HAV peptide specifically interacted with cells via HAV-E-cadherin interactions, and affected cell adhesion and clustering in a β-catenin related signaling pathway. This study provided an overview of the interactions between immobilized HAV peptide and epithelia cells. This work also laid the basis for utilizing HAV peptide on NV diamond as force sensor for future studies about the force and mechanobiology of cadherin-mediated cell-cell adhesion.

These studies gave insight into cell-ligand interactions based on the immobilized specific ligands on 2D surfaces. The development of ligand immobilized NV diamond force sensor and the fundamental study about cell-ligand interactions are complementary to each other. These results can guide to the design of new synthetic biomaterials for further cell biology studies and biomedical applications.

8. Appendix

Abbreviations

$(EtO)_3Si$-NCO	3-(triethoxysilyl)propyl isocyanate
2D	two-dimensional
3D	three-dimensional
AC	alternating current
AFM	atomic force microscopy
AOM	acousto-optical-modulator
approx.	approximately
APS	ammonium persulfate
APTES	(3-Aminopropyl)triethoxysilane
ATP	adenosine triphosphate
Au	gold
AuNP	gold nanopattern
BCMN	block copolymer micelle nanolithography
BCN-DOTA-GA	2,2',2"-(10-(4-((2-((((1R,8S,9s)-bicyclo[6.1.0]non-4-yn-9-ylmethoxy)carbonyl)amino)ethyl)amino)-1-carboxy-4-oxobutyl)-1,4,7,10-tetraazacyclododecane-1,4,7-triyl)triacetic acid
BCN-NHS	(1R,8S,9s)-Bicyclo[6.1.0]non-4-yn-9-ylmethyl N-succinimidyl carbonate
BGT	benzylguanine thiol
BRD	BCN-RGD-DOTA 3-in-1 Y-shape molecule
BSA	bovine serum albumin
BSE	backscattered electrons
BTSE	1,2-Bis(triethoxysilyl)ethane

C	carbon
c(RGDfK)C	cyclic(RGDfK)C
Ca	calcium
ca.	circa
CAM	cell adhesion molecule
CCJ	cell-cell junction
CMA	cell-matrix adhesion
D	dissipation
D2O	Deuterium Oxide
Da	dalton
DAPI	4’,6-diamidino-2-phenylindole
DBCO-PEG$_4$-NHS	Dibenzocyclooctyne-PEG4-N-hydroxysuccinimidyl ester
ddH$_2$O	Double-distilled water
DMF	dimethylformamide
DNA	deoxyribonucleic acid
DRD	DBCO-RGD-DOTA
DTT	dithiothreitol
DVC	digital volume correlation
e. g.	exempli gratia
EC	extracelluar
ECM	extracellular matrix
EDC	N-(3-Dimethylaminopropyl)-N′-ethylcarbodiimide hydrochloride
EDTA	ethylenediaminetetraacetic acid
EGTA	ethylene glycol tetraacetic acid
EPR	electron paramagnetic resonance
et al.	et alia
EtOH	ethanol
eV	electronvolt
f	frequency
FA	focal adhesion
FAK	focal adhesion kinase

FBS	fetal bovine serum
FBs	fibrillar adhesions
FITC	fluorescein isothiocyanate
FN	fibronectin
FRET	Förster resonance energy transfer
FTTC	fourier transform traction cytometry
FXs	focal complexes
GAPs	GTPase-activating proteins
Gd	gadolinium
GDP	guanosine diphosphate
GEF-H1	guanine nucleotide exchange factor H1
GEFs	guanine nucleotide exchange factors
GTP	guanosine triphosphate
h	hour
HAV	histidine-alanine-valine
HAV(s)	soluable HAV
HEPES	4-(2-hydroxyethyl)-1-piperazineethanesulfonic acid
IGF1R	insulin-like growth factor 1 receptor
IgG	Immunoglobulin G
LA-MDCK	lifeact-Madin-Darby Canine Kidney
LARG	leukemia-associated Rho GEF
LS (A)-1	Boc-NH-PEG-DOTA
LS (A)-2	H_2N-PEG-DOTA
LS (A)-3	$(EtO)_3Si$-PEG-DOTA
LS (B)	$(MeO)_3Si$-PEG-DOTA
LSCM	laser scanning confocal microscopy
M	mole
m/z	mass-to-charge ratio
maleimide-DOTA-GA	2,2',2"-(10-(1-carboxy-4-((2-(2,5-dioxo-2,5-dihydro-1H-pyrrol-1-yl)ethyl)amino)-4-oxobutyl)-1,4,7,10-tetraazacyclododecane-1,4,7-

	triyl)triacetic acid
MeOD	tetradeuteromethanol
MeOH	methanol
mg	miligram
MHz	megahertz
ml	mililiter
MLC	myosin light chain
mM	milimole
MRI	magnetic resonance imaging
MS	mass spectrometry
ms	milisecond
MT	magnetic tweezers
N	nitrogen
ND	nanodiamond
NHS	N-hydroxysuccinimide
nm	nanometer
NMR	nuclear magnetic resonance
nN	nanonewton
NSET	nonlinear state estimation technique
NV	nitrogen-vacancy
O	oxygen
OT	optical tweezers
Pa	Pascal
PAAm	polyacrylamide
PBS	phosphate-buffered saline
PBST	0.1% v/v Triton-X 100 in PBS
PDMS	poly(dimethylsiloxane)
PE	primary electrons
PEG	polyethylene glycol
PIV	particle image velocimetry
pN	piconewton
ppm	parts per million
PS-b-P2VP	polystyrene-block-poly(2-vinylpyridine)

QCM-D	quartz crystal microbalance with dissipation monitoring
$\boldsymbol{R_F}$	Flory radius
RGD	arginylglycylaspartic acid
RH	RGD and HAV peptide co-functional
RhoA	Ras homolog gene family, member A
ROCK	Rho kinase
ROI	region of interest
RS	RGD and SCR peptide co-functional surface
RSF	relative sensitivity factor
SAM	self-assembled monolayer
SCR	scrambled HAV
SDS-PAGE	sodium dodecyl sulfate polyacrylamide gel electrophoresis
SE	secondary electrons
SEM	scanning electron microscope
Si	silicon
SPAAC	strain-promoted alkyne-azide cycloadditions
TEA	triethylamine
TEMED	tetramethylethylenediamine
TEOS	tetraethyl orthosilicate
TFM	traction force microscopy
Ti	titanium
TMS	tetramethylsilane
TOFMS	time-of-flight mass spectrometry
W	watt
WLC	wormlike chain
wt%	weight percentage
XPS	X-ray photoelectron spectroscopy
YS-1	$(MeO)_3Si$-PEG-NHS
YS-2	$(MeO)_3Si$-PEG-RGD

YS-3	$(MeO)_3Si$-PEG-RGD-DOTA
δ	chemical shift
µg	microgram
µl	microliter
µm	micrometer
µM	micromole
µs	microsecond

List of Figures

List of Tables

9.Bibliography

1. B. Alberts, A. Johnson, J. Lewis, D. Morgan, M. Raff, K. Roberts, P. Walter, *Molecular Biology of the Cell, Sixth Edition*. Garland Science: New York and Abingdon, UK.: 2014.

2. R. Mecham, *The Extracellular Matrix: an Overview*. Springer-Verlag Berlin Heidelberg: 2011.

3. T. D. Pollard, W. C. Earnshaw, J. Lippincott-Schwartz, G. T. Johnson, *Cell Biology, 3rd Edition*. Elsevier Inc.: 2017.

4. B. M. Gumbiner, Cell adhesion: The molecular basis of tissue architecture and morphogenesis. *Cell* **1996,** *84* (3), 345-357.

5. G. Plopper, *The extracellular matrix and cell adhesion, in Cells*. Jones and Bartlett: Burlington: 2007.

6. R. V. Iozzo, Matrix proteoglycans: From molecular design to cellular function. *Annual Review of Biochemistry* **1998,** *67*, 609-652.

7. J. P. Xiong, T. Stehle, B. Diefenbach, R. G. Zhang, R. Dunker, D. L. Scott, A. Joachimiak, S. L. Goodman, M. A. Arnaout, Crystal structure of the extracellular segment of integrin alpha V beta 3. *Science* **2001,** *294* (5541), 339-345.

8. R. O. Hynes, Integrins: Bidirectional, allosteric signaling machines. *Cell* **2002,** *110* (6), 673-687.

9. B. H. Luo, T. A. Springer, Integrin structures and conformational signaling. *Current Opinion in Cell Biology* **2006,** *18* (5), 579-586.

10. S. J. Shattil, C. Kim, M. H. Ginsberg, The final steps of integrin activation: the end game. *Nature Reviews Molecular Cell Biology* **2010,** *11* (4), 288-300.

11. H. Lodish, A. Berk, S. L. Zipursky, P. Matsudaira, D. Baltimore, J. Darnell, *Molecular Cell Biology, 4th edition*. New York: W.H. Freeman and CO.: 2004.

12. C. S. Elangbam, C. W. Qualls, R. R. Dahlgren, Cell adhesion molecules - Update. *Veterinary Pathology* **1997,** *34* (1), 61-73.

13. P. Hermann, M. Armant, E. Brown, M. Rubio, H. Ishihara, D. Ulrich, R. G. Caspary, F. P. Lindberg, R. Armitage, C. Maliszewski, G. Delespesse, M. Sarfati, The vitronectin receptor and its associated CD47 molecule mediates proinflammatory cytokine synthesis in human monocytes by interaction with soluble CD23. *Journal of Cell Biology* **1999,** *144* (4), 767-775.

14. J. J. Bergh, H. Y. Lin, L. Lansing, S. N. Mohamed, F. B. Davis, S. Mousa, P. J. Davis, Integrin alpha(v)beta(3) contains a cell surface receptor site for thyroid hormone that is linked to activation of mitogen-activated protein kinase and induction of angiogenesis. *Endocrinology* **2005,** *146* (7), 2864-2871.

15. S. H. Kim, J. Turnbull, S. Guimond, Extracellular matrix and cell signalling: the dynamic cooperation of integrin, proteoglycan and growth factor receptor. *Journal of Endocrinology* **2011,** *209* (2), 139-151.

16. Z. Q. Sun, A. Lambacher, R. Fassler, Nascent Adhesions: From Fluctuations to a Hierarchical Organization. *Current Biology* **2014,** *24* (17), R801-R803.

17. J. D. Rotty, C. Y. Wu, J. E. Bear, New insights into the regulation and cellular functions of the ARP2/3 complex. *Nature Reviews Molecular Cell Biology* **2013,** *14* (1), 7-12.

18. C. K. Choi, M. Vicente-Manzanares, J. Zareno, L. A. Whitmore, A. Mogilner, A. R. Horwitz, Actin and alpha-actinin orchestrate the assembly and maturation of nascent adhesions in a myosin II motor-independent manner. *Nature Cell Biology* **2008,** *10* (9), 1039-U36.

19. A. Nicolas, B. Geiger, S. A. Safran, Cell mechanosensitivity controls the anisotropy of focal adhesions. *Proceedings of the National Academy of Sciences of the United States of America* **2004,** *101* (34), 12520-12525.

20. R. Zaidel-Bar, C. Ballestrem, Z. Kam, B. Geiger, Early molecular events in the assembly of matrix adhesions at the leading edge of migrating cells. *Journal of Cell Science* **2003,** *116* (22), 4605-4613.

21. R. Pankov, E. Cukierman, B. Z. Katz, K. Matsumoto, D. C. Lin, S. Lin, C. Hahn, K. M. Yamada, Integrin dynamics and matrix assembly: Tensin-dependent translocation of alpha(5)beta(1) integrins promotes early fibronectin fibrillogenesis. *Journal of Cell Biology* **2000,** *148* (5), 1075-1090.

22. B. Geiger, K. M. Yamada, Molecular Architecture and Function of Matrix Adhesions. *Cold Spring Harbor Perspectives in Biology* **2011,** *3* (5).

23. B. Geiger, A. Bershadsky, R. Pankov, K. M. Yamada, Transmembrane extracellular matrix-cytoskeleton crosstalk. *Nature Reviews Molecular Cell Biology* **2001,** *2* (11), 793-805.

24. D. Bouvard, J. Pouwels, N. De Franceschi, J. Ivaska, Integrin inactivators: balancing cellular functions in vitro and in vivo. *Nature Reviews Molecular Cell Biology* **2013,** *14* (7), 430-442.

25. B. Geiger, A. Bershadsky, Assembly and mechanosensory function of focal contacts. *Current Opinion in Cell Biology* **2001,** *13* (5), 584-592.

26. K. A. DeMali, X. W. Sun, G. A. Bui, Force Transmission at Cell-Cell and Cell-Matrix Adhesions. *Biochemistry* **2014,** *53* (49), 7706-7717.

27. P. Roca-Cusachs, N. C. Gauthier, A. del Rio, M. P. Sheetz, Clustering of alpha(5)beta(1) integrins determines adhesion strength whereas alpha(v)beta(3) and talin enable mechanotransduction. *Proceedings of the*

National Academy of Sciences of the United States of America **2009,** *106* (38), 16245-16250.

28. A. del Rio, R. Perez-Jimenez, R. C. Liu, P. Roca-Cusachs, J. M. Fernandez, M. P. Sheetz, Stretching Single Talin Rod Molecules Activates Vinculin Binding. *Science* **2009,** *323* (5914), 638-641.

29. M. X. Yao, B. T. Goult, H. Chen, P. W. Cong, M. P. Sheetz, J. Yan, Mechanical activation of vinculin binding to talin locks talin in an unfolded conformation. *Scientific Reports* **2014,** *4*.

30. C. G. Galbraith, K. M. Yamada, M. P. Sheetz, The relationship between force and focal complex development. *Journal of Cell Biology* **2002,** *159* (4), 695-705.

31. A. M. Pasapera, I. C. Schneider, E. Rericha, D. D. Schlaepfer, C. M. Waterman, Myosin II activity regulates vinculin recruitment to focal adhesions through FAK-mediated paxillin phosphorylation. *Journal of Cell Biology* **2010,** *188* (6), 877-890.

32. C. Grashoff, B. D. Hoffman, M. D. Brenner, R. B. Zhou, M. Parsons, M. T. Yang, M. A. McLean, S. G. Sligar, C. S. Chen, T. Ha, M. A. Schwartz, Measuring mechanical tension across vinculin reveals regulation of focal adhesion dynamics. *Nature* **2010,** *466* (7303), 263-U143.

33. A. Carisey, R. Tsang, A. M. Greiner, N. Nijenhuis, N. Heath, A. Nazgiewicz, R. Kemkemer, B. Derby, J. Spatz, C. Ballestrem, Vinculin Regulates the Recruitment and Release of Core Focal Adhesion Proteins in a Force-Dependent Manner. *Current Biology* **2013,** *23* (4), 271-281.

34. D. A. Calderwood, A. Huttenlocher, W. B. Kiosses, D. M. Rose, D. G. Woodside, M. A. Schwartz, M. H. Ginsberg, Increased filamin binding to beta-

integrin cytoplasmic domains inhibits cell migration. *Nature Cell Biology* **2001,** *3* (12), 1060-1068.

35. J. H. Hartwig, J. Tyler, T. P. Stossel, Actin-Binding Protein Promotes the Bipolar and Perpendicular Branching of Actin-Filaments. *Journal of Cell Biology* **1980,** *87* (3), 841-848.

36. R. Niederman, P. C. Amrein, J. Hartwig, 3-Dimensional Structure of Actin-Filaments and of an Actin Gel Made with Actin-Binding Protein. *Journal of Cell Biology* **1983,** *96* (5), 1400-1413.

37. D. Choquet, D. P. Felsenfeld, M. P. Sheetz, Extracellular matrix rigidity causes strengthening of integrin-cytoskeleton linkages. *Cell* **1997,** *88* (1), 39-48.

38. E. C. Lessey, C. Guilluy, K. Burridge, From Mechanical Force to RhoA Activation. *Biochemistry* **2012,** *51* (38), 7420-7432.

39. R. J. Marjoram, E. C. Lessey, K. Burridge, Regulation of RhoA Activity by Adhesion Molecules and Mechanotransduction. *Current Molecular Medicine* **2014,** *14* (2), 199-208.

40. C. Guilluy, V. Swaminathan, R. Garcia-Mata, E. T. O'Brien, R. Superfine, K. Burridge, The Rho GEFs LARG and GEF-H1 regulate the mechanical response to force on integrins. *Nature Cell Biology* **2011,** *13* (6), 722-U211.

41. L. Julian, M. F. Olson, Rho-associated coiled-coil containing kinases (ROCK): structure, regulation, and functions. *Small GTPases* **2014,** *5*, e29846.

42. K. Clark, M. Langeslag, C. G. Figdor, F. N. van Leeuwen, Myosin II and mechanotransduction: a balancing act. *Trends in Cell Biology* **2007,** *17* (4), 178-186.

43. C. H. Streuli, Integrins and cell-fate determination. *Journal of Cell Science* **2009,** *122* (2), 171-177.

44. T. Lecuit, A. S. Yap, E-cadherin junctions as active mechanical integrators in tissue dynamics. *Nature Cell Biology* **2015,** *17* (5), 533-539.

45. T. J. C. Harris, U. Tepass, Adherens junctions: from molecules to morphogenesis. *Nature Reviews Molecular Cell Biology* **2010,** *11* (7), 502-514.

46. S. Pokutta, W. I. Weis, Structure and mechanism of Cadherins and catenins in cell-cell contacts. *Annual Review of Cell and Developmental Biology* **2007,** *23*, 237-261.

47. J. L. Maitre, C. P. Heisenberg, Three Functions of Cadherins in Cell Adhesion Review. *Current Biology* **2013,** *23* (14), R626-R633.

48. T. D. Perez, W. J. Nelson, Cadherin adhesion: mechanisms and molecular interactions. *Handbook of Experimental Pharmacology* **2004,** (165), 3-21.

49. D. B. Ivanov, M. P. Philippova, V. A. Tkachuk, Structure and functions of classical cadherins. *Biochemistry-Moscow* **2001,** *66* (10), 1174-1186.

50. O. W. Blaschuk, N-cadherin antagonists as oncology therapeutics. *Philosophical Transactions of the Royal Society B-Biological Sciences* **2015,** *370* (1661).

51. P. D. Mccrea, C. W. Turck, B. Gumbiner, A Homolog of the Armadillo Protein in Drosophila (Plakoglobin) Associated with E-Cadherin. *Science* **1991,** *254* (5036), 1359-1361.

52. H. Aberle, S. Butz, J. Stappert, H. Weissig, R. Kemler, H. Hoschuetzky, Assembly of the Cadherin Catenin Complex in-Vitro with Recombinant Proteins. *Journal of Cell Science* **1994,** *107*, 3655-3663.

53. R. B. Hazan, L. Kang, S. Roe, P. I. Borgen, D. L. Rimm, Vinculin is associated with the E-cadherin adhesion complex. *Journal of Biological Chemistry* **1997,** *272* (51), 32448-32453.

54. M. Watabe-Uchida, N. Uchida, Y. Imamura, A. Nagafuchi, K. Fujimoto, T. Uemura, S. Vermeulen, F. van Roy, E. D. Adamson, M. Takeichi, alpha-catenin-vinculin interaction functions to organize the apical junctional complex in epithelial cells. *Journal of Cell Biology* **1998,** *142* (3), 847-857.

55. B. M. Jockusch, G. Isenberg, Interaction of Alpha-Actinin and Vinculin with Actin - Opposite Effects on Filament Network Formation. *Proceedings of the National Academy of Sciences of the United States of America-Biological Sciences* **1981,** *78* (5), 3005-3009.

56. D. L. Rimm, E. R. Koslov, P. Kebriaei, C. D. Cianci, J. S. Morrow, Alpha(1)(E)-Catenin Is an Actin-Binding and Actin-Bundling Protein Mediating the Attachment of F-Actin to the Membrane Adhesion Complex. *Proceedings of the National Academy of Sciences of the United States of America* **1995,** *92* (19), 8813-8817.

57. S. Yonemura, Y. Wada, T. Watanabe, A. Nagafuchi, M. Shibata, alpha-Catenin as a tension transducer that induces adherens junction development. *Nature Cell Biology* **2010,** *12* (6), 533-U35.

58. M. G. Lampugnani, A. Zanetti, F. Breviario, G. Balconi, F. Orsenigo, M. Corada, R. Spagnuolo, M. Betson, V. Braga, E. Dejana, VE-cadherin regulates endothelial actin activating Rac and increasing membrane association of Tiam. *Molecular Biology of the Cell* **2002,** *13* (4), 1175-1189.

59. N. K. Noren, C. M. Niessen, B. M. Gumbiner, K. Burridge, Cadherin engagement regulates Rho family GTPases. *Journal of Biological Chemistry* **2001,** *276* (36), 33305-33308.

60. E. Theveneau, R. Mayor, Cadherins in collective cell migration of mesenchymal cells. *Current Opinion in Cell Biology* **2012,** *24* (5), 677-684.

61. B. Baum, M. Georgiou, Dynamics of adherens junctions in epithelial establishment, maintenance, and remodeling. *Journal of Cell Biology* **2011,** *192* (6), 907-917.

62. G. F. Weber, M. A. Bjerke, D. W. DeSimone, Integrins and cadherins join forces to form adhesive networks. *Journal of Cell Science* **2011,** *124* (8), 1183-1193.

63. T. Onodera, T. Sakai, J. C. Hsu, K. Matsumoto, J. A. Chiorini, K. M. Yamada, Btbd7 Regulates Epithelial Cell Dynamics and Branching Morphogenesis. *Science* **2010,** *329* (5991), 562-565.

64. E. Avizienyte, A. W. Wyke, R. J. Jones, G. W. McLean, M. A. Westhoff, V. G. Brunton, M. C. Frame, Src-induced de-regulation of E-cadherin in colon cancer cells requires integrin signalling. *Nature Cell Biology* **2002,** *4* (8), 632-638.

65. N. Chattopadhyay, Z. M. Wang, L. K. Ashman, S. M. Brady-Kalnay, J. A. Kreidberg, alpha 3 beta 1 integrin-CD151, a component of the cadherin-catenin complex, regulates PTP mu, expression and cell-cell adhesion. *Journal of Cell Biology* **2003,** *163* (6), 1351-1362.

66. A. Canonici, W. Steelant, V. Rigot, A. Khomitch-Baud, H. Boutaghou-Cherid, E. Bruyneel, F. Van Roy, F. Garrouste, G. Pommier, F. Andre, Insulin-like growth factor-I receptor, E-cadherin and alpha v integrin form a dynamic complex under the control of alpha-catenin. *International Journal of Cancer* **2008,** *122* (3), 572-582.

67. C. Yeaman, K. K. Grindstaff, W. J. Nelson, New perspectives on mechanisms involved in generating epithelial cell polarity. *Physiological Reviews* **1999,** *79* (1), 73-98.

68. M. Burute, M. Thery, Spatial segregation between cell-cell and cell-matrix adhesions. *Current Opinion in Cell Biology* **2012,** *24* (5), 628-636.

69. G. K. Ojakian, D. R. Ratcliffe, R. Schwimmer, Integrin regulation of cell-cell adhesion during epithelial tubule formation. *Journal of Cell Science* **2001,** *114* (5), 941-952.

70. A. Al-Kilani, O. de Freitas, S. Dufour, F. Gallet, Negative Feedback from Integrins to Cadherins: A Micromechanical Study. *Biophysical Journal* **2011,** *101* (2), 336-344.

71. A. Koenig, C. Mueller, C. Hasel, G. Adler, A. Menke, Collagen type I induces disruption of E-cadherin-mediated cell-cell contacts and promotes proliferation of pancreatic carcinoma cells. *Cancer Research* **2006,** *66* (9), 4662-4671.

72. K. Giehl, A. Menke, Microenvironmental regulation of E-cadherin-mediated adherens junctions. *Frontiers in Bioscience* **2008,** *13*, 3975-3985.

73. R. B. Sperry, N. H. Bishop, J. J. Bramwell, M. N. Brodeur, M. J. Carter, B. T. Fowler, Z. B. Lewis, S. D. Maxfield, D. M. Staley, R. M. Vellinga, M. D. H. Hansen, Zyxin Controls Migration in Epithelial-Mesenchymal Transition by Mediating Actin-Membrane Linkages at Cell-Cell Junctions. *Journal of Cellular Physiology* **2010,** *222* (3), 612-624.

74. Q. le Duc, Q. M. Shi, I. Blonk, A. Sonnenberg, N. Wang, D. Leckband, J. de Rooij, Vinculin potentiates E-cadherin mechanosensing and is recruited to actin-anchored sites within adherens junctions in a myosin II-dependent manner. *Journal of Cell Biology* **2010,** *189* (7), 1107-1115.

75. F. L. Zhang, S. Saha, A. Kashina, Arginylation-dependent regulation of a proteolytic product of talin is essential for cell-cell adhesion. *Journal of Cell Biology* **2012,** *197* (6), 819-836.

76. N. Borghi, M. Lowndes, V. Maruthamuthu, M. L. Gardel, W. J. Nelson, Regulation of cell motile behavior by crosstalk between cadherin- and integrin-mediated adhesions. *Proceedings of the National Academy of Sciences of the United States of America* **2010,** *107* (30), 13324-13329.

77. M. L. McCain, H. Lee, Y. Aratyn-Schaus, A. G. Kleber, K. K. Parker, Cooperative coupling of cell-matrix and cell-cell adhesions in cardiac muscle. *Proceedings of the National Academy of Sciences of the United States of America* **2012,** *109* (25), 9881-9886.

78. A. Katsumi, A. W. Orr, E. Tzima, M. A. Schwartz, Integrins in mechanotransduction. *Journal of Biological Chemistry* **2004,** *279* (13), 12001-12004.

79. P. G. Gillespie, R. G. Walker, Molecular basis of mechanosensory transduction. *Nature* **2001,** *413* (6852), 194-202.

80. W. J. Polacheck, C. S. Chen, Measuring cell-generated forces: a guide to the available tools. *Nature Methods* **2016,** *13* (5), 415-423.

81. E. Bell, B. Ivarsson, C. Merrill, Production of a Tissue-Like Structure by Contraction of Collagen Lattices by Human-Fibroblasts of Different Proliferative Potential Invitro. *Proceedings of the National Academy of Sciences of the United States of America* **1979,** *76* (3), 1274-1278.

82. H. Vandenburgh, J. Shansky, F. Benesch-Lee, K. Skelly, J. M. Spinazzola, Y. Saponjian, B. S. Tseng, Automated drug screening with contractile muscle tissue engineered from dystrophic myoblasts. *FASEB Journal* **2009,** *23* (10), 3325-3334.

83. W. R. Legant, A. Pathak, M. T. Yang, V. S. Deshpande, R. M. McMeeking, C. S. Chen, Microfabricated tissue gauges to measure and manipulate forces from 3D

microtissues. *Proceedings of the National Academy of Sciences of the United States of America* **2009,** *106* (25), 10097-10102.

84. J. Lee, M. Leonard, T. Oliver, A. Ishihara, K. Jacobson, Traction Forces Generated by Locomoting Keratocytes. *Journal of Cell Biology* **1994,** *127* (6), 1957-1964.

85. M. Dembo, T. Oliver, A. Ishihara, K. Jacobson, Imaging the traction stresses exerted by locomoting cells with the elastic substratum method. *Biophysical Journal* **1996,** *70* (4), 2008-2022.

86. W. R. Legant, C. K. Choi, J. S. Miller, L. Shao, L. Gao, E. Betzig, C. S. Chen, Multidimensional traction force microscopy reveals out-of-plane rotational moments about focal adhesions. *Proceedings of the National Academy of Sciences of the United States of America* **2013,** *110* (3), 881-886.

87. S. S. Hur, Y. H. Zhao, Y. S. Li, E. Botvinick, S. Chien, Live Cells Exert 3-Dimensional Traction Forces on Their Substrata. *Cellular and Molecular Bioengineering* **2009,** *2* (3), 425-436.

88. S. A. Maskarinec, C. Franck, D. A. Tirrell, G. Ravichandran, Quantifying cellular traction forces in three dimensions. *Proceedings of the National Academy of Sciences of the United States of America* **2009,** *106* (52), 22108-22113.

89. Q. Z. Tseng, E. Duchemin-Pelletier, A. Deshiere, M. Balland, H. Guillou, O. Filhol, M. Thery, Spatial organization of the extracellular matrix regulates cell-cell junction positioning. *Proceedings of the National Academy of Sciences of the United States of America* **2012,** *109* (5), 1506-1511.

90. W. R. Legant, J. S. Miller, B. L. Blakely, D. M. Cohen, G. M. Genin, C. S. Chen, Measurement of mechanical tractions exerted by cells in three-dimensional matrices. *Nature Methods* **2010,** *7* (12), 969-U113.

91. J. P. Fu, Y. K. Wang, M. T. Yang, R. A. Desai, X. A. Yu, Z. J. Liu, C. S. Chen, Mechanical regulation of cell function with geometrically modulated elastomeric substrates. *Nature Methods* **2010,** *7* (9), 733-U95.

92. L. Trichet, J. Le Digabel, R. J. Hawkins, R. K. Vedula, M. Gupta, C. Ribrault, P. Hersen, R. Voituriez, B. Ladoux, Evidence of a large-scale mechanosensing mechanism for cellular adaptation to substrate stiffness. *Proceedings of the National Academy of Sciences of the United States of America* **2012,** *109* (18), 6933-6938.

93. S. Ghassemi, G. Meacci, S. M. Liu, A. A. Gondarenko, A. Mathur, P. Roca-Cusachs, M. P. Sheetz, J. Hone, Cells test substrate rigidity by local contractions on submicrometer pillars. *Proceedings of the National Academy of Sciences of the United States of America* **2012,** *109* (14), 5328-5333.

94. Y. Liu, K. Galior, V. P. Y. Ma, K. Salaita, Molecular Tension Probes for Imaging Forces at the Cell Surface. *Accounts of Chemical Research* **2017,** *50* (12), 2915-2924.

95. C. Jurchenko, K. S. Salaita, Lighting Up the Force: Investigating Mechanisms of Mechanotransduction Using Fluorescent Tension Probes. *Molecular and Cellular Biology* **2015,** *35* (15), 2570-2582.

96. P. P. Lehenkari, M. A. Horton, Single integrin molecule adhesion forces in intact cells measured by atomic force microscopy. *Biochemical and Biophysical Research Communications* **1999,** *259* (3), 645-650.

97. N. Walter, C. Selhuber, H. Kessler, J. P. Spatz, Cellular unbinding forces of initial adhesion processes on nanopatterned surfaces probed with magnetic tweezers. *Nano Letters* **2006,** *6* (3), 398-402.

98. K. Hayakawa, H. Tatsumi, M. Sokabe, Actin stress fibers transmit and focus force to activate mechanosensitive channels. *Journal of Cell Science* **2008,** *121* (4), 496-503.

99. Y. Liu, R. Medda, Z. Liu, K. Galior, K. Yehl, J. P. Spatz, E. A. Cavalcanti-Adam, K. Salaita, Nanoparticle Tension Probes Patterned at the Nanoscale: Impact of Integrin Clustering on Force Transmission. *Nano Letters* **2014,** *14* (10), 5539-5546.

100. B. L. Blakely, C. E. Dumelin, B. Trappmann, L. M. McGregor, C. K. Choi, P. C. Anthony, V. Duesterberg, B. M. Baker, S. M. Block, D. R. Liu, C. S. Chen, A DNA-based molecular probe for optically reporting cellular traction forces. *Nature Methods* **2014,** *11* (12), 1229-+.

101. Y. Liu, K. Yehl, Y. Narui, K. Salaita, Tension Sensing Nanoparticles for Mechano-Imaging at the Living/Nonliving Interface. *Journal of the American Chemical Society* **2013,** *135* (14), 5320-5323.

102. D. R. Stabley, C. Jurchenko, S. S. Marshall, K. S. Salaita, Visualizing mechanical tension across membrane receptors with a fluorescent sensor. *Nature Methods* **2012,** *9* (1), 64-U172.

103. M. Morimatsu, A. H. Mekhdjian, A. S. Adhikari, A. R. Dunn, Molecular Tension Sensors Report Forces Generated by Single Integrin Molecules in Living Cells. *Nano Letters* **2013,** *13* (9), 3985-3989.

104. D. H. Davis, C. S. Giannoulis, R. W. Johnson, T. A. Desai, Immobilization of RGD to < 111 > silicon surfaces for enhanced cell adhesion and proliferation. *Biomaterials* **2002,** *23* (19), 4019-4027.

105. M. H. Ho, D. M. Wang, H. J. Hsieh, H. C. Liu, T. Y. Hsien, J. Y. Lai, L. T. Hou, Preparation and characterization of RGD-immobilized chitosan scaffolds. *Biomaterials* **2005,** *26* (16), 3197-3206.

106. U. Hersel, C. Dahmen, H. Kessler, RGD modified polymers: biomaterials for stimulated cell adhesion and beyond. *Biomaterials* **2003,** *24* (24), 4385-4415.

107. D. Guarnieri, A. De Capua, M. Ventre, A. Borzacchiello, C. Pedone, D. Marasco, M. Ruvo, P. A. Netti, Covalent immobilized RGD gradient on PEG hydrogel scaffold influences cell migration parameters. *Acta Biomaterialia* **2010,** *6* (7), 2532-2539.

108. F. Z. Cui, W. M. Tian, S. P. Hou, Q. Y. Xu, I. S. Lee, Hyaluronic acid hydrogel immobilized with RGD peptides for brain tissue engineering. *Journal of Materials Science-Materials in Medicine* **2006,** *17* (12), 1393-1401.

109. J. Tsai, L. Kam, Rigidity-Dependent Cross Talk between Integrin and Cadherin Signaling. *Biophysical Journal* **2009,** *96* (6), L39-L41.

110. D. Fichtner, B. Lorenz, S. Engin, C. Deichmann, M. Oelkers, A. Janshoff, A. Menke, D. Wedlich, C. M. Franz, Covalent and Density-Controlled Surface Immobilization of E-Cadherin for Adhesion Force Spectroscopy. *PloS One* **2014,** *9* (3).

111. A. Ganz, M. Lambert, A. Saez, P. Silberzan, A. Buguin, R. M. Mege, B. Ladoux, Traction forces exerted through N-cadherin contacts. *Biology of the Cell* **2006,** *98* (12), 721-730.

112. B. D. Cosgrove, K. L. Mui, T. P. Driscoll, S. R. Caliari, K. D. Mehta, R. K. Assoian, J. A. Burdick, R. L. Mauck, N-cadherin adhesive interactions modulate matrix mechanosensing and fate commitment of mesenchymal stem cells. *Nature Materials* **2016,** *15* (12), 1297-1306.

113. R. Glass, M. Moller, J. P. Spatz, Block copolymer micelle nanolithography. *Nanotechnology* **2003,** *14* (10), 1153-1160.

114. J. Deng, C. S. Zhao, J. P. Spatz, Q. Wei, Nanopatterned Adhesive, Stretchable Hydrogel to Control Ligand Spacing and Regulate Cell Spreading and Migration. *ACS Nano* **2017,** *11* (8), 8282-8291.

115. J. Kankare, Sauerbrey equation of quartz crystal microbalance in liquid medium. *Langmuir* **2002,** *18* (18), 7092-7094.

116. S. T. Wang, L. Feng, H. Liu, T. L. Sun, X. Zhang, L. Jiang, D. B. Zhu, Manipulation of surface wettability between superhydrophobicity and superhydrophilicity on copper films. *Chemphyschem* **2005,** *6* (8), 1475-1478.

117. D. Briggs, J. T. Grant, *Surface analysis by Auger and x‐ray photoelectron spectroscopy*. IMPublications, Chichester, UK and SurfaceSpectra, Manchester, UK: 2003.

118. K. Downard, *Mass Spectrometry: A Foundation Course*. Royal Society of Chemistry: 2004.

119. R. K. Harris, E. D. Becker, S. M. C. De Menezes, P. Granger, R. E. Hoffman, K. W. Zilm, Further conventions for NMR shielding and chemical shifts (IUPAC recommendations 2008). *Pure and Applied Chemistry* **2008,** *80* (1), 59-84.

120. R. E. Hoffman, Standardization of chemical shifts of TMS and solvent signals in NMR solvents. *Magnetic Resonance in Chemistry* **2006,** *44* (6), 606-616.

121. R. Schirhagl, K. Chang, M. Loretz, C. L. Degen, Nitrogen-Vacancy Centers in Diamond: Nanoscale Sensors for Physics and Biology. *Annual Review of Physical Chemistry, Vol 65* **2014,** *65*, 83-105.

122. Y. Z. Wu, F. Jelezko, M. B. Plenio, T. Weil, Diamond Quantum Devices in Biology. *Angewandte Chemie-International Edition* **2016,** *55* (23), 6586-6598.

123. G. Balasubramanian, P. Neumann, D. Twitchen, M. Markham, R. Kolesov, N. Mizuochi, J. Isoya, J. Achard, J. Beck, J. Tissler, V. Jacques, P. R. Hemmer, F. Jelezko, J. Wrachtrup, Ultralong spin coherence time in isotopically engineered diamond. *Nature Materials* **2009,** *8* (5), 383-387.

124. X. Q. Zhang, R. Lam, X. Y. Xu, E. K. Chow, H. J. Kim, D. Ho, Multimodal Nanodiamond Drug Delivery Carriers for Selective Targeting, Imaging, and Enhanced Chemotherapeutic Efficacy. *Advanced Materials* **2011,** *23* (41), 4770-+.

125. Y. L. Liu, K. W. Sun, Protein Functionalized Nanodiamond Arrays. *Nanoscale Research Letters* **2010,** *5* (6), 1045-1050.

126. B. M. Chang, H. H. Lin, L. J. Su, W. D. Lin, R. J. Lin, Y. K. Tzeng, R. T. Lee, Y. C. Lee, A. L. Yu, H. C. Chang, Highly Fluorescent Nanodiamonds Protein-Functionalized for Cell Labeling and Targeting. *Advanced Functional Materials* **2013,** *23* (46), 5737-5745.

127. H. Huang, E. Pierstorff, E. Osawa, D. Ho, Active nanodiamond hydrogels for chemotherapeutic delivery. *Nano Letters* **2007,** *7* (11), 3305-3314.

128. J. S. Xiao, X. P. Duan, Q. Yin, Z. W. Zhang, H. J. Yu, Y. P. Li, Nanodiamonds-mediated doxorubicin nuclear delivery to inhibit lung metastasis of breast cancer. *Biomaterials* **2013,** *34* (37), 9648-9656.

129. J. Li, Y. Zhu, W. X. Li, X. Y. Zhang, Y. Peng, Q. Huang, Nanodiamonds as intracellular transporters of chemotherapeutic drug. *Biomaterials* **2010,** *31* (32), 8410-8418.

130. Y. Q. Li, X. P. Zhou, D. X. Wang, B. S. Yang, P. Yang, Nanodiamond mediated delivery of chemotherapeutic drugs. *Journal of Materials Chemistry* **2011,** *21* (41), 16406-16412.

131. M. Vinante, G. Digregorio, L. Lunelli, S. Forti, S. Musso, L. Vanzetti, A. Lui, L. Pasquardini, M. Giorcelli, A. Tagliaferro, M. Anderle, C. Pederzolli, Human Plasma Protein Adsorption on Carbon-Based Materials. *Journal of Nanoscience and Nanotechnology* **2009,** *9* (6), 3785-3791.

132. A. Krueger, D. Lang, Functionality is Key: Recent Progress in the Surface Modification of Nanodiamond. *Advanced Functional Materials* **2012,** *22* (5), 890-906.

133. X. X. Li, J. Q. Shao, Y. Qin, C. Shao, T. T. Zheng, L. Ye, TAT-conjugated nanodiamond for the enhanced delivery of doxorubicin. *Journal of Materials Chemistry* **2011,** *21* (22), 7966-7973.

134. L. Zhao, Y. H. Xu, T. Akasaka, S. Abe, N. Komatsu, F. Watari, X. Chen, Polyglycerol-coated nanodiamond as a macrophage-evading platform for selective drug delivery in cancer cells. *Biomaterials* **2014,** *35* (20), 5393-5406.

135. L. Zhao, Y. H. Xu, H. M. Qin, S. Abe, T. Akasaka, T. Chano, F. Watari, T. Kimura, N. Komatsu, X. Chen, Platinum on Nanodiamond: A Promising Prodrug Conjugated with Stealth Polyglycerol, Targeting Peptide and Acid-Responsive Antitumor Drug. *Advanced Functional Materials* **2014,** *24* (34), 5348-5357.

136. S. E. Dsouza, M. H. Ginsberg, E. F. Plow, Arginyl-Glycyl-Aspartic Acid (Rgd) - a Cell-Adhesion Motif. *Trends in Biochemical Sciences* **1991,** *16* (7), 246-250.

137. A. D. Sherry, R. D. Brown, C. F. G. Geraldes, S. H. Koenig, K. T. Kuan, M. Spiller, Synthesis and Characterization of the Gadolinium (3+) Complex of Dota-Propylamide - a Model Dota-Protein Conjugate. *Inorganic Chemistry* **1989,** *28* (3), 620-622.

138. J. M. Zhu, Bioactive modification of poly(ethylene glycol) hydrogels for tissue engineering. *Biomaterials* **2010,** *31* (17), 4639-4656.

139. N. E. Mbua, J. Guo, M. A. Wolfert, R. Steet, G. J. Boons, Strain-Promoted Alkyne-Azide Cycloadditions (SPAAC) Reveal New Features of Glycoconjugate Biosynthesis. *ChemBioChem* **2011,** *12* (12), 1911-1920.

140. H. Okudera, A. Hozumi, The formation and growth mechanisms of silica thin film and spherical particles through the Stober process. *Thin Solid Films* **2003,** *434* (1-2), 62-68.

141. Q. Wei, T. Becherer, R. C. Mutihac, P. L. M. Noeske, F. Paulus, R. Haag, I. Grunwald, Multivalent Anchoring and Cross-Linking of Mussel-Inspired Antifouling Surface Coatings. *Biomacromolecules* **2014,** *15* (8), 3061-3071.

142. N. Patel, M. C. Davies, M. Hartshorne, R. J. Heaton, C. J. Roberts, S. J. B. Tendler, P. M. Williams, Immobilization of protein molecules onto homogeneous and mixed carboxylate-terminated self-assembled monolayers. *Langmuir* **1997,** *13* (24), 6485-6490.

143. C. Bouchiat, M. D. Wang, J. F. Allemand, T. Strick, S. M. Block, V. Croquette, Estimating the persistence length of a worm-like chain molecule from force-extension measurements. *Biophysical Journal* **1999,** *76* (1), 409-413.

144. A. R. Nicholas, M. J. Scott, N. I. Kennedy, M. N. Jones, Effect of grafted polyethylene glycol (PEG) on the size, encapsulation efficiency and permeability of vesicles. *Biochimica Et Biophysica Acta-Biomembranes* **2000,** *1463* (1), 167-178.

145. Z. Drira, V. K. Yadavalli, Nanomechanical measurements of polyethylene glycol hydrogels using atomic force microscopy. *Journal of the Mechanical Behavior of Biomedical Materials* **2013,** *18*, 20-28.

146. N. Q. Balaban, U. S. Schwarz, D. Riveline, P. Goichberg, G. Tzur, I. Sabanay, D. Mahalu, S. Safran, A. Bershadsky, L. Addadi, B. Geiger, Force and focal adhesion

assembly: a close relationship studied using elastic micropatterned substrates. *Nature Cell Biology* **2001,** *3* (5), 466-472.

147. S. Steinert, F. Ziem, L. T. Hall, A. Zappe, M. Schweikert, N. Gotz, A. Aird, G. Balasubramanian, L. Hollenberg, J. Wrachtrup, Magnetic spin imaging under ambient conditions with sub-cellular resolution. *Nature Communications* **2013,** *4*.

148. A. I. Chervanyov, G. Heinrich, Flory radius of polymers in a periodic field: An exact analytic theory. *European Physical Journal E* **2007,** *24* (3), 271-276.

149. P. Mi, N. Dewi, H. Yanagie, D. Kokuryo, M. Suzuki, Y. Sakurai, Y. M. Li, I. Aoki, K. Ono, H. Takahashi, H. Cabral, N. Nishiyama, K. Kataoka, Hybrid Calcium Phosphate-Polymeric Micelles Incorporating Gadolinium Chelates for Imaging-Guided Gadolinium Neutron Capture Tumor Therapy. *ACS Nano* **2015,** *9* (6), 5913-5921.

150. C. T. Lefort, K. Wojciechowski, D. C. Hocking, N-cadherin Cell-Cell Adhesion Complexes Are Regulated by Fibronectin Matrix Assembly. *Journal of Biological Chemistry* **2011,** *286* (4), 3149-3160.

151. V. Noe, J. Willems, J. Vandekerckhove, F. Van Roy, E. Bruyneel, M. Mareel, Inhibition of adhesion and induction of epithelial cell invasion by HAV-containing E-cadherin-specific peptides. *Journal of Cell Science* **1999,** *112* (1), 127-135.

152. I. T. Makagiansar, M. Avery, Y. Hu, K. L. Audus, T. J. Siahaan, Improving the selectivity of HAV-peptides in modulating E-cadherin-E-cadherin interactions in the intercellular junction of MDCK cell monolayers. *Pharmaceutical Research* **2001,** *18* (4), 446-453.

153. Z. Erami, P. Timpson, W. Yao, R. Zaidel-Bar, K. I. Anderson, There are four dynamically and functionally distinct populations of E-cadherin in cell junctions. *Biology Open* **2015,** *4* (11), 1481-1489.

154. E. H. Schwab, T. L. M. Pohl, T. Haraszti, G. K. Schwaerzer, C. Hiepen, J. P. Spatz, P. Knaus, E. A. Cavalcanti-Adam, Nanoscale Control of Surface Immobilized BMP-2: Toward a Quantitative Assessment of BMP-Mediated Signaling Events. *Nano Letters* **2015,** *15* (3), 1526-1534.

155. Q. Wei, T. Becherer, S. Angioletti-Uberti, J. Dzubiella, C. Wischke, A. T. Neffe, A. Lendlein, M. Ballauff, R. Haag, Protein Interactions with Polymer Coatings and Biomaterials. *Angewandte Chemie-International Edition* **2014,** *53* (31), 8004-8031.

156. Q. Wei, R. Haag, Universal polymer coatings and their representative biomedical applications. *Materials Horizons* **2015,** *2* (6), 567-577.

157. M. Arnold, E. A. Cavalcanti-Adam, R. Glass, J. Blummel, W. Eck, M. Kantlehner, H. Kessler, J. P. Spatz, Activation of integrin function by nanopatterned adhesive interfaces. *Chemphyschem* **2004,** *5* (3), 383-388.

158. R. Oria, T. Wiegand, J. Escribano, A. Elosegui-Artola, J. J. Uriarte, C. Moreno-Pulido, I. Platzman, P. Delcanale, L. Albertazzi, D. Navajas, X. Trepat, J. M. Garcia-Aznar, E. A. Cavalcanti-Adam, P. Roca-Cusachs, Force loading explains spatial sensing of ligands by cells. *Nature* **2017,** *552* (7684), 219-224.

159. M. Stoker, M. Perryman, An Epithelial Scatter Factor Released by Embryo Fibroblasts. *Journal of Cell Science* **1985,** *77* (Aug), 209-223.

160. M. Kovacs, J. Toth, C. Hetenyi, A. Malnasi-Csizmadia, J. R. Sellers, Mechanism of blebbistatin inhibition of myosin II. *Journal of Biological Chemistry* **2004,** *279* (34), 35557-35563.

161. B. Geiger, J. P. Spatz, A. D. Bershadsky, Environmental sensing through focal adhesions. *Nature Reviews Molecular Cell Biology* **2009,** *10* (1), 21-33.

162. J. A. Park, L. Atia, J. A. Mitchel, J. J. Fredberg, J. P. Butler, Collective migration and cell jamming in asthma, cancer and development. *Journal of Cell Science* **2016,** *129* (18), 3375-3383.

163. D. Sulsky, S. Childress, J. K. Percus, A Model of Cell Sorting. *Journal of Theoretical Biology* **1984,** *106* (3), 275-301.

164. D. P. Bi, J. H. Lopez, J. M. Schwarz, M. L. Manning, A density-independent rigidity transition in biological tissues. *Nature Physics* **2015,** *11* (12), 1074-1079.

165. D. P. Bi, X. B. Yang, M. C. Marchetti, M. L. Manning, Motility-Driven Glass and Jamming Transitions in Biological Tissues. *Physical Review X* **2016,** *6* (2).

166. W. J. Nelson, R. Nusse, Convergence of Wnt, beta-catenin, and cadherin pathways. *Science* **2004,** *303* (5663), 1483-1487.

Acknowledgement

First of all, I would like to thank Prof. Dr. Joachim Spatz who provided me the opportunity to finish my PhD thesis in this group. I am very grateful for his unreserved support in my academic and personal life during the last years. I am also thankful to Prof. Dr. Jörg Wrachtrup for providing me the cooperation project about the Nitrogen-Vacancy diamond based force sensor, and for his constructive suggestions during the research.

I wish to express my gratitude to Prof. (apl.) Dr. Reiner Dahint for for being my second reviewer and to PD Dr. Günter Majer for being my external examiner. I also appreciate Dr. Fania Geiger in helping with the German summary of my dissertation.

I especially want to thank Dr. Qiang Wei. I appreciate his knowledge on surface chemistry and the experience on cell adhesion behavior on biomaterial surface. He helped me very patiently, both on laboratory skills and on the designing of the project.

Thanks to my cooperators for their kind help. Dr. Zhiqin Chu proposed the cooperation project about the Nitrogen-Vacancy diamond based force sensor. He gave me many suggestions both on the designing of the force sensor construction, and on the later relaxation time tests. Dr. Florestan Ziem, Dr. Andrea Zappe and Marwa Garsi performed the relaxation time tests together. They are friendly and gave me basic knowledge about Nitrogen-Vacancy induced photoluminescence.

I am very thankful to my colleges Dr. Jacopo Di Russo and Dr. Medhavi Vishwakarma for solving the biology problems very kindly in my research. Also thanks to Ximeng Hua, who prepared microbeads embedded hydrogels used in traction force microscopy for me.

I also would like to express my thanks to PD Dr. Günter Majer and Dr. Igor Moudrakovski for their help in nuclear magnetic resonance spectroscopy tests, Dr. Michael Noeske and Kathrin Müller for X-ray photoelectron spectroscopy tests, Dr. Stephan Rauschenbach for Mass spectroscopy tests, and Frank Thiele for preparing gold thin film on glass slides for me.

I appreciate very much the nice time I had in the last years in Spatz group. Thanks to all of my colleges for the relaxed and comfortable environment when I was working. Thank you for your assiduities whenever I had problems.

My family and friends must be thanked for their care throughout all this years. I am very grateful to my parents for their understanding and supporting.

Especially, I want to thank my dear husband, Qiang Wei. Thank you for being always on my side and love me so much!

Eidesstattliche Versicherung gemäß § 8 der Promotionsordnung der Naturwissenschaftlich-Mathematischen Gesamtfakultät der Universität Heidelberg

1. Bei der eingereichten Dissertation zu dem Thema "**Cell-ligand interaction study by immobilizing ligand on surface**" handelt es sich um meine eigenständig erbrachte Leistung.

2. Ich habe nur die angegebenen Quellen und Hilfsmittel benutzt und mich keiner unzulässigen Hilfe Dritter bedient. Insbesondere habe ich wörtlich oder sinngemäß aus anderen Werken übernommene Inhalte als solche kenntlich gemacht.

3. Die Arbeit oder Teile davon habe ich bislang nicht an einer Hochschule des In- oder Auslandes als Bestandteil einer Prüfungs- oder Qualifikationsleistung vorgelegt.

4. Die Richtigkeit der vorstehenden Erklärung bestätige ich.

5. Die Bedeutung der eidesstattlichen Versicherung und die strafrechtlichen Folgen einer unrichtigen oder unvollständigen eidesstattlichen Versicherung sind mir bekannt.

Ich versichere an Eides statt, dass ich nach bestem Wissen die reine Wahrheit erklärt und nichts verschwiegen habe.

Ort und Datum

Unterschrift